

**STUDIES ON PHOTODYNAMIC AND PHOTON-
ACTIVATION TREATMENT OF CANCER CELLS USING
CHLOROPHYLL DERIVATIVE CONJUGATED TO
COPPER IODIDE**

By

PAROMITA SARBADHIKARY

Enrolment No: LIFE 03201104001

Raja Ramanna Centre for Advanced Technology, Indore

A thesis submitted to the

Board of Studies in Life Sciences

In partial fulfillment of requirements

for the Degree of

DOCTOR OF PHILOSOPHY

of

HOMI BHABHA NATIONAL INSTITUTE

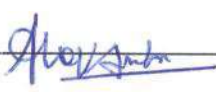
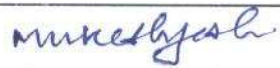
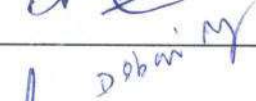


August, 2017

Homi Bhabha National Institute

Recommendations of the Viva Voce Committee

As members of the Viva Voce Committee, we certify that we have read the dissertation prepared by Paromita Sarbadhikary entitled "**Studies on photodynamic and photon-activation treatment of cancer cells using chlorophyll derivative conjugated to copper iodide**" and recommend that it may be accepted as fulfilling the thesis requirement for the award of Degree of Doctor of Philosophy.

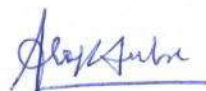
Chairman – Prof. S. K. Dixit		Date: 11/6/18
Guide / Convener – Prof. A. Dube		Date: 11/04/18
Examiner - Prof. D. Ramaiah		Date: 11.04.2018
Member 1- Prof. K. I. Priyadarsini		Date: 11.4.2018
Member 2- Prof. M. P. Joshi		Date: 11/04/18
Member 3- Prof. S. N. Jha		Date:
Member 4- Prof. R. Makde		Date: 11/4/18
Member 5- Prof. D. Nayak		Date: 11.4.18
Member 6- Prof. A. Das		Date: 11.4.2018

Final approval and acceptance of this thesis is contingent upon the candidate's submission of the final copies of the thesis to HBNI.

I/We hereby certify that I/we have read this thesis prepared under my/our direction and recommend that it may be accepted as fulfilling the thesis requirement.

Date: 12/04/18

Place: RRCAT, Indore



Dr. Alok Dube
(Guide)

STATEMENT BY AUTHOR

This dissertation has been submitted in partial fulfillment of requirements for an advanced degree at Homi Bhabha National Institute (HBNI) and is deposited in the Library to be made available to borrowers under rules of the HBNI.

Brief quotations from this dissertation are allowable without special permission, provided that accurate acknowledgement of source is made. Requests for permission for extended quotation from or reproduction of this manuscript in whole or in part may be granted by the Competent Authority of HBNI when in his or her judgment the proposed use of the material is in the interests of scholarship. In all other instances, however, permission must be obtained from the author.



(Paromita Sarbadhikary)

DECLARATION

I, hereby declare that the investigation presented in the thesis has been carried out by me. The work is original and has not been submitted earlier as a whole or in part for a degree / diploma at this or any other Institution / University.

Paromita Sarbadhikary

(Paromita Sarbadhikary)

List of Publications arising from the thesis

In Journals

1. "Synthesis and Characterization of Photodynamic activity of Iodinated Chlorin p_6 Copper complex", **P. Sarbadhikary**, A. Dube, P. K. Gupta. *RSC Adv.*, **2016**, *6*, 75782- 75792.
2. "Iodinated Chlorin p_6 Copper complex induces anti-proliferative effect in oral cancer cells through elevation of intracellular reactive oxygen species", **P. Sarbadhikary**, A. Dube. *Chem. Biol. Interact.*, **2017**, *277*, 137-144.
3. "Enhancement of radiosensitivity of oral carcinoma cells by Iodinated chlorin p_6 copper complex in combination with synchrotron X-ray radiation", **P. Sarbadhikary**, A. Dube. *J. Synchrotron Rad.*, **2017**, *24*, 1265-1275.
4. "Spectroscopic investigations on binding of Iodinated Chlorin p_6 Copper complex to Human serum albumin", **P. Sarbadhikary**, A. Dube. *Photochem. Photobiol. Sci.*, **2017**, *16*, 1762-1770.

In Conferences

1. "Radio/ photosensitization of human oral cancer cells through activation of iodo- Chlorin p_6 copper complex with X -ray radiation", **P. Sarbadhikary**, A. Dube, V. P. Dhamgaye, P. K. Gupta. International Conference on Radiation Research: Impact on human health and environment. *J Radiat Cancer Res.*, **2016**, *7*, Suppl S1:2-56.
2. "Efficacy of Iodinated Chlorin p_6 -Copper complex for Photodynamic treatment of cancer cells", **P. Sarbadhikary**, A. Dube, P. K. Gupta. In proceedings of DAE-BRNS National Laser Symposium (NLS-25) 2016.

Patent:

A. Dube, **P. Sarbadhikary**, P. K. Gupta. A Metal complex of chlorophyll derivative for magnetic resonance imaging and photodynamic therapy. Indian patent application No. 4912/MUM/2015, filed on 29 Dec. 2015.

(Paromita Sarbadhikary)

DEDICATED TO ALL MY LOVED ONES

For their unconditional love, support and encouragement

ACKNOWLEDGEMENTS

It's a great opportunity for me to thank all those people who have contributed in their own ways for the successful completion of this my Ph.D work. I would like to express my sincere gratitude to my guide Dr. Alok Dube, for his invaluable guidance, planning, encouragement and continuous support which motivated me to work with full devotion throughout my Ph.D tenure.

I am grateful to Professor P. K. Gupta (former doctoral committee chairman), Dr. S. K. Dixit (present doctoral committee chairman), Dr. K. I. Priyadarsini (External expert) and all other doctoral committee members, for their suggestions and discussions during the course my thesis work. I express my sincere thanks to Dr. S. K. Majumder (Head, Laser Biomedical applications section) for his constant support and help. I would also like to thank Dr. Mrinalini Sharma for her valuable suggestions, scientific discussions and proof reading of this thesis.

I am thankful to, Dr. G. S. Lodha and Dr. M. K. Tiwari for helping with XRF measurement at BL -16, Dr. V. P. Dhamgaye and Shri. B. S. Thakur for their assistance in carrying out X-ray irradiation experiments at beamline-7 of Indus –II synchrotron source at our center. I would like to thank Dr. B. Jain for helping with FTIR measurements and Dr. K. Das for time resolved fluorescence measurements. I also thank Dr. B. S. Dwarakanath, INMAS, Delhi and Dr. U. M. Warawdekar, ACTREC, Mumbai for providing oral cancer cell lines. I acknowledge Dr. S. K. Sandur and Dr. D. Sharma (BARC, Mumbai) for providing technical support and expert guidance in flow cytometry experiments and Dr M. Shanmugam (IIT Bombay, Mumbai) for EPR measurement.

I feel great pleasure to express my heartfelt thanks to Dr. K. Sahu, Dr. A. Uppal, and Dr. R. Shrivastava, for their help and suggestions. I would also like to thank Mrs. Harsha Bansal, Mr. Y. Deshpande, Mr. Anupam Chowdhary, Mr. Gyan Singh and all other members of Laser Biomedical Applications Section for their kind co-operation and assistance. My heartfelt thanks to my seniors Dr. Arpana Parihar, Dr. Surya Prakash Singh and friends Gopal, Pooja, Srinivas, Dipankar, Smritijit, Yashveer, Debashis, Dipanjana, Rijul, Saurabh, Azam and all other friends of RRCAT for their support. I thank all my batch mates (55th batch BARC) Moushumi, Babita, Shraddha, Pooja, Kiran, Dhiman, Rajesh, Jagannath and Vinod for their love and support during the training period. I also thank Nisha madam, Bipasa madam, Swapna madam, Lipilekha madam and Swati Madam for being my inspiration.

My heartfelt gratitude goes to my true and best friend Sanjay who was always by my side during the ups and downs during my Ph.D tenure. Even though he do not understand my field of work, but still he use to listen my every word very patiently. Due to his constant support, encouragement and positive views, I was able to overcome the tough times of my research and complete my Ph.D work.

And, importantly I owe my deepest gratitude to my father, mother, brother and late grandma for their unconditional love, care, support and faith. They are always being my source of inspiration. I can proudly say that wherever I stand today is because of them.

I am grateful to Homi Bhabha National Institute, Department of Atomic Energy, RRCAT for providing financial assistance during my Ph.D research work.

Paromita Sarbadhikary

CONTENTS

Synopsis	i -x
List of schemes	xi
List of figures	xii - xv
List of tables	xvi
List of abbreviations	xvii - xviii
Chapter 1. <i>Introduction and Review of Literature</i>	(1-35)
1.1. Cancer treatment modalities	4
1.1.1. Radiotherapy	5
1.1.2. Chemotherapy	7
1.1.3. Chemoradiotherapy	9
1.2. Pitfalls and challenges of cancer therapies	12
1.3. Novel chemoradiotherapy based treatment modalities	14
1.3.1. Photon-activation therapy (PAT)	14
1.3.2. Photodynamic therapy (PDT)	16
1.3.2.1. Photophysical and Photochemical mechanism of PDT	17
1.3.2.2. Photosensitizers in PDT	18
1.3.2.3. Limitations of PDT	22
1.4. Insertion of high Z elements: a promising approach to overcome the limitations of PDT	24

1.4.1. Effect of metal and heavy elements on photophysical properties of PS	24
1.4.2. Metal conjugated tetrapyrroles as chemotoxic and phototoxic agent	30
1.4.3. PSs for combined radiotherapy and PDT using X-ray irradiation	32
1.5. Aim of the study	34
Chapter 2. <i>Materials and Methods</i>	(36-60)
2.1. Materials	37
2.1.1. Fluorescence probes	37
2.1.2. Biochemicals & Culture media	37
2.1.3. Cell lines	38
2.1.4. Preparation of Cp_6 -CuI conjugate	38
2.2. Methods	39
2.2.1 Cell culture	39
2.2.2 Treatment of cells with ICp_6 -Cu	39
2.2.3. Light Irradiation	40
2.2.4. MTT assay	40
2.2.5. Determination of intracellular ROS levels	41
2.3. Methods used for characterization of ICp_6-Cu	42
2.3.1. Spectroscopic characterization of ICp_6 -Cu	42
2.3.2. Fluorescence assay for determination of generation of 1O_2 and other ROS in solution	43
2.3.3. Photobleaching	44

2.3.4. Octanol/ water partition coefficient	44
2.3.5. Binding studies of ICp ₆ -Cu with HSA	45
2.3.5.1. Spectroscopic measurements	45
2.3.5.2. Fluorescence lifetime measurements.....	46
2.3.6. Binding studies of ICp ₆ -Cu with DNA	47
2.3.6.1. Spectroscopic measurements	47
2.3.6.2. DNA mobility shift assay.....	47
2.4. Methods used in studies on PDT efficacy of ICp₆-Cu	48
2.4.1. Intracellular uptake of ICp ₆ -Cu and Cp ₆	48
2.4.1.1. BCA method of protein estimation	48
2.4.2. Intracellular localization of ICp ₆ -Cu	49
2.4.3. Photodynamic treatment of cancer cells	49
2.4.4. Microscopy for PDT-induced cell death	50
2.5. Methods used in studies on efficacy of ICp₆-Cu for PAT	51
2.5.1. X-ray irradiation	51
2.5. 2. XO-Fricke assay	53
2.5.3. Determination of cytotoxicity	55
2.5.4 Clonogenic survival assay	55
2.5.5. Determination of intracellular ROS levels	56
2.5.6. ICp ₆ -Cu induced DNA damage upon X-ray irradiation	56
2.5.7. Cell cycle analysis	57
2.6. Methods used in studies on chemotoxic potential of ICp₆-Cu	58
2.6.1. Treatment of cells with ICp ₆ -Cu	58
2.6.2. Determination of cytotoxicity	58

2.6.3. Cell proliferation assay	58
2.6.4. Confocal microscopy for study of cellular morphology and cell death	59
2.6.5. Determination of intracellular ROS levels	60
2.7. Statistical analysis	60
Chapter 3. Characterization of ICp₆-Cu	(61-93)
3.1. Introduction	62
3.2. Results	63
3.2.1. Characterization of structure	63
3.2.1.1 Formation of complex of Cp ₆ with CuI	63
3.2.1.2. Position of copper and iodine in the complex	64
3.2.1.3. Octanol/ water partition coefficient	69
3.2.2. Photodynamic activity in aqueous solution	70
3.2.2.1. ¹ O ₂ and ROS generation efficiency of ICp ₆ -Cu	70
3.2.2.2 Photobleaching of ICp ₆ -Cu and Cp ₆	71
3.2.3. Interaction of ICp ₆ -Cu with HSA and DNA	73
3.2.3.1. Interaction and binding of ICp ₆ -Cu with HSA	73
3.2.3.2. Fluorescence quenching of HSA by ICp ₆ -Cu	75
3.2.3.3. Binding constant and number of binding sites	76
3.2.3.4. Proximity of ICp ₆ -Cu to tryptophan in HSA	77
3.2.3.5. Effect of ICp ₆ -Cu on Protein conformation	80
3.2.3.6. Effect of HSA binding on stability of ICp ₆ -Cu	80
3.2.3.7. Binding affinity of ICp ₆ -Cu with DNA	82
3.2.3.9. Gel –mobility shift assay	83

3.3. Discussion	84
3.3.1. Structural characterization	84
3.3.2. Mode of photodynamic action of ICp ₆ -Cu	87
3.3.3. Ability of ICp ₆ -Cu to bind with serum albumin	88
3.3.4. Ability of ICp ₆ -Cu to bind with DNA	92
3.4. Conclusion	93
 Chapter 4. <i>Photodynamic efficacy of ICp₆-Cu in cancer cells</i>(94-106)	
4.1. Introduction	95
4.2. Results	96
4.2.1. Intracellular uptake of ICp ₆ -Cu and Cp ₆	96
4.2.2. Intracellular distribution of ICp ₆ -Cu	96
4.2.3. Phototoxicity of ICp ₆ -Cu in cancer cells	97
4.2.4. ICp ₆ -Cu induced morphological changes	98
4.2.5. Effect of ROS quenchers on ICp ₆ -Cu induced phototoxicity...	101
4.2.6. Phototoxicity under hypoxic conditions	102
4.3. Discussion	102
4.4. Conclusion	106
 Chapter 5. <i>Radiosensitization efficacy of ICp₆-Cu in combination with</i>	
<i>synchrotron X-ray radiation</i> (107- 120)	
5.1. Introduction	108
5.2. Results	109
5.2.1. Intracellular uptake of ICp ₆ -Cu	109
5.2.2. ICp ₆ -Cu pretreatment enhances X-ray induced cytotoxicity ...	109

5.2.3. X-ray dose enhancement effect by ICp ₆ -Cu	111
5.2.4. Enhancement in X-ray induced ROS formation by ICp ₆ -Cu ...	112
5.2.5. DNA damage induction and repair	112
5.2.6. Radiation induced cell organelle damage	114
5.2.7. Cell cycle distribution and induction of cell death	115
5.3. Discussion	118
5.4. Conclusion	120
Chapter 6. Chemotoxic potential of ICp₆-Cu in cancer cells....(121-133)	
6.1. Introduction	122
6.2. Results	123
6.2.1. ICp ₆ -Cu induced cytotoxicity	123
6.2.2. Effect of ICp ₆ -Cu on cell morphology	124
6.2.3. ICp ₆ -Cu induced organelle damage	125
6.2.4. Effect of ICp ₆ -Cu on intracellular ROS levels	128
6.3. Discussion	130
6.4. Conclusions	133
Chapter 7. Summary and Future Prospective	(134- 138)
Bibliography	(139-175)
Appendix (Supplementary Information and Research Output).....	176

SYNOPSIS

Cancer is one of the major health problems and life-threatening disease which is responsible for ~8.8 million deaths globally [1]. In India, more than 1 million new cases of cancer are diagnosed every year [2] and the prevalent cases belong to cancer of oral cavity, breast, cervix, lung, colorectal, stomach, esophagus, pharynx, gallbladder and leukemia [3]. Radio and chemotherapy, either alone or in combination are the major treatment modalities for the clinical management of cancer. However, despite significant success in prolonging the life expectancy of patients, the effectiveness of these modalities is limited by severe side effects such as peripheral nerve damage, severe allergic reactions, Immune-suppression, damage to various vital organs and development of resistance in tumors [4, 5]. In past few decades, photodynamic therapy (PDT) has gained considerable attention as promising alternative treatment modality for cancer [6]. PDT utilizes a photosensitive drug referred as 'photosensitizer' (PS) and irradiation with light (630- 800 nm) to induce tumor damage through the generation of reactive oxygen species (ROS) [7]. Photofrin, a semi-purified preparation containing hematoporphyrin derivatives (HpD) was the first FDA approved drug for PDT of cancer. The application of HpD, however, was associated with drawbacks such as low absorption coefficient, poor tumor selectivity and prolonged retention in the body [8].

To find better PDT agents, various types of PSs such as derivatives of porphyrins, phthalocyanines, texaphyrins and chlorins have been widely investigated [7, 8]. Among these PSs, chlorin derivatives obtained from chlorophyll, a plant pigment have received particular attention. Chlorophyll derivatives possess ideal

photophysical properties such as high absorption coefficient at longer wavelengths that penetrate deeper in tissue and higher efficiency to generate excited triplet state and ROS [8]. Another important advantage of chlorophyll based PS is relatively low-cost due to feasible synthesis from abundantly available natural pigment. Further, the amphiphilic chlorophyll derivatives e.g. Radachlorin, mono aspartyl derivative of chlorin e6 (MACe6) can accumulate preferentially in tumor due to their ability to interact with drug transport proteins such as serum albumin and low-density lipoprotein (LDL) [9]. One such derivative, Chlorin *p6* (*Cp6*) was investigated by A Dube and coworkers as potential PS for PDT of cancer. *Cp6* showed potent photodynamic activity against cancer cells, localized preferentially in oral cavity tumors of hamster, cleared rapidly from the skin and induced complete tumor regression after PDT [10, 11].

The aim of this Ph.D. work was to investigate the use of copper iodide (CuI) conjugated *Cp6* as a multimodal anticancer agent by exploring its photodynamic, X-ray photon-activation and chemotoxic activity against cancer cells. CuI was selected for conjugation with *Cp6* based on following rationale. It is known that insertion of high Z element in PS molecule can enhance the yield of its triplet state through heavy atom effect and thereby improve its efficiency to generate ROS. Further, the X-ray absorption property of copper & iodide can be exploited for photon-activation therapy (PAT). The combination of PS containing high Z element and X-ray photon-activation is a novel approach which holds considerable potential for the treatment of deep-seated tumors [12]. In addition, copper due to redox active property is capable of inducing cytotoxicity in cancer cells by disturbing the cellular redox homeostasis. In this respect, it is pertinent to mention that copper complexes have received significant

attention as potential anticancer agents [13]. Finally, both copper & iodine, being essential trace elements are relatively less toxic than other non-essential metals such as Pt, Ru, Gd that have been used for cancer therapeutics [14].

The thesis is organized into seven chapters:

Chapter 1. Introduction and review of literature: This chapter first provides a general understanding on the cellular basis of cancer and tumor development. This is followed by an overview of conventional cancer treatment modalities such as chemotherapy, radiotherapy, combined chemoradiotherapy, PAT and their limitations. The chapter then deals with PDT covering its basic principles, history and present status, types of PSs used in PDT including chlorophyll derivatives. Finally, a review of literature pertaining to the application of metal conjugated PSs for PDT, chemotherapy and PAT is provided.

Chapter 2. Materials and methods: This chapter first provides details of various materials such as chemicals and reagents, cell lines, culture media, fluorescence probes etc., used in the experiments. This is followed by detailed description of the methods used in studies on four different aspects mentioned above. For characterization of Cp_6-CuI complex (ICp_6-Cu) to determine its probable chemical structure, photodynamic activity and interaction with serum albumin and DNA various spectroscopy methods (UV-Visible, fluorescence, XRF, FTIR, EPR, Mass spectroscopy) were used. The second section provides procedures used for culture of cancer cells, various treatments and irradiation procedure, methods used to determine cellular uptake and intracellular localization of ICp_6-Cu , assessment of cell viability, proliferation, cell death and cellular ROS levels. The third section provides specific methods used to assess the efficacy of ICp_6-Cu for X-ray photo-activation (8-10 keV)

such as clonogenic survival assay, γ -H2AX immune fluorescence assay for DNA damage and repair analysis and flow cytometry for cell cycle analysis.

Chapter 3. Characterization of ICp₆-Cu: In this chapter, spectroscopic studies carried out to deduce chemical structure of Cp₆-CuI conjugate, assess its photodynamic properties and characterize its interaction with human serum albumin (HSA) and DNA have been described. The metal complex was obtained by reacting Cp₆ with CuI at equimolar concentration. The formation of the complex between Cp₆ and CuI was completed at 1:1 stoichiometry as indicated by a shift in Q band of Cp₆ from 663 nm to 634 nm. The presence of copper and iodide in the purified conjugate was confirmed by X-ray fluorescence. The results of FTIR and EPR spectroscopy suggest that the copper is attached to Cp₆ at the two adjacent carboxylic groups. Analysis of mass spectrum of the complex suggested attachment of iodide at meso position. Studies on the photochemical generation of singlet oxygen (¹O₂) and other ROS using fluorescence probes revealed that the photodynamic action of ICp₆-Cu is mediated predominantly via type I process. These results demonstrated that ICp₆-Cu possess potent photodynamic activity which is exceptional because other known copper complexes of tetrapyrrole compounds are poor PSs [15].

Serum albumin is a major drug transport protein which acts as a carrier for amphiphilic photosensitizers including Cp₆ [16]. Therefore, the interaction of ICp₆-Cu with HSA was investigated using UV-Vis absorption and fluorescence spectroscopy. Results showed that the addition of HSA to ICp₆-Cu at physiology pH led to ~7 nm red shift in its Soret and Q band absorption. The binding constant (K_b) and the number of binding sites (n) of ICp₆-Cu obtained from quenching of the intrinsic fluorescence of HSA was 2.5 X 10⁶ M⁻¹ and 1.2 respectively. The distance between Trp-214 residue

and ICp_6 -Cu computed from Forster non-radiative energy transfer theory was 3.1 nm. Synchronous spectroscopy revealed that quenching of protein Trp fluorescence was higher than that for Tyr with no significant shift in peak position. Results suggested that HSA acts as a carrier protein for ICp_6 -Cu with a high probability of its binding at subdomain IIA and the binding of ICp_6 -Cu had no effect on the conformation of the HSA.

Metal complexes due to their cationic charge often display an affinity with DNA and cause genotoxicity [17]. Results of UV-Vis spectroscopic studies on the interaction of ICp_6 -Cu with calf-thymus DNA showed a significant decrease in the absorption of ICp_6 -Cu at Soret band (hypochromism). The value of binding constant (K_b) determined from the analysis of hypochromism was almost same for ICp_6 -Cu and Cp_6 . The binding of ICp_6 -Cu with supercoiled plasmid DNA (pUC 19) assessed by gel mobility shift assay revealed that ICp_6 -Cu did not form a strong complex with DNA. These results suggested that interaction of ICp_6 -Cu with DNA is electrostatic in nature and there is no possibility of ICp_6 -Cu to target cellular DNA.

Chapter 4. PDT efficacy of ICp_6 -Cu in cancer cells: This chapter deals with the studies on cellular uptake, intracellular localization and phototoxicity of ICp_6 -Cu in human oral cancer cell lines (NT8e and 4451). Confocal microscopy combined with cell organelle specific fluorescence probes revealed that ICp_6 -Cu localized in ER and lysosomes but not in mitochondria, Golgi and cell nucleus. The uptake of ICp_6 -Cu in cancer cells was significantly higher than that for Cp_6 which correlated with their relative hydrophobicity. Treatment of cells with ICp_6 -Cu (10 μ M, 3 h) and subsequent exposure to a red LED light (630 nm \pm 20 nm) led to high cytotoxicity (~90 % at 12 J/cm²) and the phototoxic effect was dependent on ICp_6 -Cu concentration and light

dose. Observations on cell and nuclear morphology suggested that the mode of PDT induced cell death in 4451 and NT8e was necrosis and apoptosis respectively, which was expected due to the difference of their p53 gene status. Studies on phototoxicity of ICp₆-Cu using mechanistic probes of ¹O₂ (D₂O, sodium azide) and free radicals (DMSO, mannitol) provided evidence that the mode of action of ICp₆-Cu in the cellular environment is mediated via both type I and type II photochemical pathway. Studies also revealed one significant advantage of ICp₆-Cu over Cp₆ that its phototoxicity is not significantly affected under hypoxic conditions.

Chapter 5. Radiosensitization efficacy of ICp₆-Cu in combination with synchrotron X-ray radiation: Combination of synchrotron X-ray radiation and metal-based radiosensitizer is a novel form of PAT which offers an advantage to treat malignant tumors with greater efficacy and higher precision than the conventional radiation therapy [18]. In this chapter, the efficacy of ICp₆-Cu to radiosensitize oral cancer cells through photon-activation with synchrotron X-ray radiation (8-10 keV) was investigated. Results showed that pre-treatment of cells with ICp₆-Cu (3 h) led to significant enhancement in the X-ray induced cytotoxicity. The radiosensitization effect of ICp₆-Cu was more pronounced in 4451 cells than that for NT8e cells and correlated with the level of ICp₆-Cu uptake in the two cell lines. Sensitization enhancement factor obtained through clonogenic cell survival assay was ~1 and ~2.5 at 10 μM and 30 μM, respectively. As compared to X-ray alone the combined treatment led to substantial increase in intracellular ROS levels and confocal microscopy revealed that lysosomes are the main site of intracellular damage. Measurements on the number of γ-H2AX foci showed that pre-treatment with ICp₆-Cu have no effect on the initial level of X-ray induced DNA damage. Further, in

contrast to X-ray alone, the cells in combined treatment displayed persistence of a significant number of γ -H2AX foci at 24 h post-irradiation. The result of flow cytometry measurements suggested that both X-ray alone and combined treatment did not alter cell cycle progression. These results demonstrated that IC_{p6}-Cu is a promising radiosensitizer for PAT of cancer cells and its radiosensitization action is mediated through photoactivation induced ROS generation, damage to vital cell organelle and inhibition of DNA repair.

Chapter 6. Chemotoxic potential of IC_{p6}-Cu in cancer cells: Copper complexes due to their ability to undergo redox reaction in the cellular environment and thus inducing oxidative stress have been actively explored as a novel class of anticancer agents [13]. In this chapter, results of the investigation on the possibility of IC_{p6}-Cu to exert chemotoxic action against oral cancer cells and non-cancerous keratinocytes are provided. The cells were treated with various concentration of IC_{p6}-Cu for 3 h to 48 h in dark. Results show that in oral cancer cells, IC_{p6}-Cu led to increase in cytotoxicity in a concentration-dependent manner and IC₅₀ value was $\sim 40 \mu\text{M}$. In contrast, IC_{p6}-Cu from 10-100 μM did not induce any significant cytotoxic effect in non-cancerous human keratinocytes cells. Results of multiple point chemosensitivity assay revealed that IC_{p6}-Cu at $\sim 40 \mu\text{M}$ led to cytostatic effect and at higher concentration, it caused cell death in both the cell lines. Cell morphology studied by confocal microscopy showed an absence of cell death via necrosis or apoptosis. Instead, the treated cells displayed distinct features of non-apoptotic death such as highly vacuolated cytoplasm, rounded off morphology, lysosomal membrane permeabilization and damage to cytoskeleton F-actin filaments. In addition, IC_{p6}-Cu treatment led to a time-dependent increase in the level of ROS in cancer cells and the cytotoxicity of IC_{p6}-Cu was

significantly inhibited by pre-treatment of cells with antioxidants (glutathione and trolox). These findings suggest that ICp_6 -Cu can also act as chemotoxic agent and because of ability to elevate oxidative stress it may provide tumor selective chemotoxicity by exploiting difference of redox environment in normal and cancer cells.

Chapter 7. Summary and Future Prospective: Here the summary of various studies carried out as part of this thesis work has been provided. The important findings on the efficacy of ICp_6 -Cu as a potential candidate for PDT, PAT and chemotherapy, advantages of combined treatments and possibility of further application of ICp_6 -Cu in radiotherapy and imaging have been discussed.

Bibliography:

1. Ferlay J, Soerjomataram I, Dikshit R, Eser S, Mathers C, Rebelo M, Parkin DM, Forman D, Bray F. Cancer incidence and mortality worldwide: sources, methods and major patterns in GLOBOCAN 2012. *Int J Cancer*. 2015; 136: E359-386.
2. Mallath MK, Taylor DG, Badwe RA, Rath GK, Shanta V, Pramesh CS, Digumarti R, Sebastian P, Borthakur BB, Kalwar A, et al. The growing burden of cancer in India: epidemiology and social context. *Lancet Oncol*. 2014; 15: e205–e212.
3. Bakhya Shree and Radhasaraswathy. Incidence and risk factors of most prevalent cancers in India. *Int J Pharm Bio Sci*. 2015; 6: (B) 436 - 443.
4. Sharma RA, Plummer R, Stock JK, Greenhalgh TA, Ataman O, Kelly S, Clay R, Adams RA, Baird RD, Billingham L, et al. Clinical development of new drug-radiotherapy combinations. *Nat Rev Clin Oncol*. 2016; 13:627-642.

5. Higgins GS, O'Cathail SM, Muschel RJ, McKenna WG. Drug radiotherapy combinations: review of previous failures and reasons for future optimism. *Cancer Treat Rev.* 2015; 41:105-113.
6. Agostinis P, Berg K, Cengel KA, Foster TH, Girotti AW, Gollnick SO, Hahn SM, Hamblin MR, Juzeniene A, Kessel D et al. Photodynamic therapy of cancer : an update. *CA Cancer J Clin.* 2011; 61:250-281.
7. Abrahamse H, Hamblin MR. New photosensitizers for photodynamic therapy. *Biochem J.* 2016; 473: 347-364.
8. Nyman ES, Hynninen PH. Research advances in the use of tetrapyrrolic photosensitizers for photodynamic therapy. *J Photochem Photobiol B.* 2004; 73:1-28.
9. Ortel B, Calzavara-Pinton P. Advances in photodynamic therapy. A review. *G Ital Dermatol Venereol.* 2010; 145: 461-475.
10. Dube A, Sharma S, Gupta PK. Evaluation of chlorin p6 for photodynamic treatment of squamous cell carcinoma in the hamster cheek pouch model. *Oral Oncol.* 2006; 42:77–82.
11. Dube A, Sharma S, Gupta PK. Tumor regression induced by photodynamic treatment with chlorin p6 in hamster cheek pouch model of oral carcinogenesis: Dependence of mode of tumor cell death on the applied drug dose. *Oral Oncol.* 2011; 47: 467–471.
12. Ishibashi N, Fujiwara K, Pandey RK, Kataba M, Oguni A, Igarashi J, Soma M, Shizukuishi T, Maebayashi T, Abe K. An Iodine labeled porphyrin as a new radiation sensitizer in human bladder cancer cells in vitro and in vivo, combining photodynamic therapy (PDT) with photon activation therapy (PAT). *Nihon Univ J Med.* 2013; 72: 212-219.

13. Santini C, Pellei M, Gandin V, Porchia M, Tisato F, Marzano C. Advances in copper complexes as anticancer agents. *Chem Rev.* 2014; 114: 815-862.
14. Zhou C-H, Zhang H-Z, Cui S-F, Lv J-S, Yan C-Y, Wan K, Zhang Y-Y, Zhang S-L, Cai G-X, Geng R-X et al. Recent Developments in Organometallic Supramolecular Complexes as Anticancer Drugs, in: Prudhomme M (Eds.) *Advances in Anticancer Agents in Medicinal Chemistry Vol 2*: Bentham Science Inc., 2013; pp. 46-129.
15. Josefsen LB, Boyle RW. Photodynamic therapy and the development of metal-based photosensitisers. *Met Based Drugs.* 2008; 2008:276109.
16. Mishra PP, Patel S, Datta A. Effect of increased hydrophobicity on the binding of two model amphiphilic chlorin drugs for photodynamic therapy with blood plasma and its components. *J Phys Chem B.* 2006; 110: 21238-21244.
17. Komor AC, Barton JK. The path for metal complexes to a DNA target. *Chem Commun (Camb).* 2013; 49: 3617-3630.
18. Kobayashi K, Usami N, Porcel E, Lacombe S, Le Sech C. Enhancement of radiation effect by heavy elements. *Mutat Res.* 2010; 704: 123-131

LIST OF SCHEMES

Scheme No.	Page No.
1.1. Schematic representation of Cell cycle phases and checkpoints.....	3
1.2. The three-phase process of carcinogenesis.....	5
1.3. Interaction of X-rays with high-Z element	15
1.4. Schematic illustration of Jablonski diagram including photochemical reactions.....	19
2.1. Experimental set-up at X-ray lithography beamline (BL-7) used for X-ray irradiation of cells in 96 well plate.....	52

LIST OF FIGURES

Figure 2.1. The emission spectrum of synchrotron X-ray in the energy range of (8-10 keV).	52
Figure 2.2. The absorbance spectra for irradiated samples of Xylenol orange Fricke solution and the dose-response plot of change in absorbance at 560 nm (ΔA) of Xylenol orange Fricke solution vs No. of scans.....	54
Figure 3.1. Structure of Cp_6	63
Figure 3.2. Absorption and fluorescence spectra of Cp_6 and Cp_6-CuI	64
Figure 3.3. XRF spectrum of ICp_6-CuI	65
Figure 3.4. ESR spectrum of Cp_6-CuI at 100 K in methanol.	65
Figure 3.5. FTIR spectra of Cp_6 and Cp_6-CuI	67
Figure 3.6. Mass spectrum of Cp_6-CuI	68
Figure 3.7. Proposed structure of ICp_6-Cu	69
Figure 3.8. Plot of Cp_6 and ICp_6-Cu induced photodynamic generation of 1O_2 and total ROS, plotted as an increase in fluorescence of SOSG and DCF.	71
Figure 3.9. Plot of Cp_6 and ICp_6-Cu induced photodynamic generation of ROS plotted as an increase in fluorescence of APF in presence of NaN_3 and D_2O	72
Figure 3.10. Photobleaching of Cp_6 and ICp_6-Cu	72
Figure 3.11. Absorption and fluorescence spectra of ICp_6-Cu in presence of different concentration of HSA.	73

Figure 3.12. Changes in the fluorescence emission spectra of HSA on addition of different concentration of ICp_6-Cu	76
Figure 3.13. Stern–Volmer plot and double reciprocal plot of HSA fluorescence quenching upon addition of different concentration of ICp_6-Cu	77
Figure 3.14. Spectral overlap of fluorescence of HSA and absorption of ICp_6-Cu and fluorescence spectra ($\lambda_{ex} = 280$ nm) of ICp_6-Cu alone and in the presence of HSA.	79
Figure 3.15. Synchronous fluorescence spectra of HSA in the presence of different concentration of ICp_6-Cu recorded at $\Delta\lambda = 60$ nm and $\Delta\lambda = 15$ nm.	81
Figure 3.16. Fluorescence quenching of tryptophan and tyrosine residue vs concentration of ICp_6-Cu	81
Figure 3.17. Absorption spectra of ICp_6-Cu in presence of HSA after 0 h, 12 h, 24 h and 48 h of incubation in dark.	82
Figure 3.18. Absorption spectra of ICp_6-Cu in presence of increasing amounts of CT-DNA and Plot of $[DNA]/[\epsilon_a - \epsilon_f]$ vs $[DNA]$	83
Figure 3.18. Absorption spectra of Cp_6 in presence of increasing amounts of CT-DNA and Plot of $[DNA]/[\epsilon_a - \epsilon_f]$ vs $[DNA]$	84
Figure 3.20. Image of agarose gel after electrophoresis of pUC19 plasmid DNA that was pre-incubated with different concentration of ICp_6-Cu	84
Figure 4.1. Colocalization of ICp_6-Cu with Lyso and ER-tracker NT8e cells.	97
Figure 4.2. Colocalization of ICp_6-Cu with Mito and Golgi tracker in NT8e cells.	98
Figure. 4.3. Concentration and light dose-dependent phototoxicity of ICp_6-Cu in cancer cells.	99

Figure 4.4. Phase contrast microphotographs of cancer cells after PDT showing cell morphology.	99
Figure 4.5. Fluorescence microphotographs of HO-PI stained cancer cells after ICp_6-Cu induced PDT and determination of percentage of apoptotic and necrotic cells.	100
Figure 4.6. Percent phototoxicity induced by ICp_6-Cu in NT8e cells in absence and presence of quenchers of ROS.	101
Figure 4.7. Percent phototoxicity of ICp_6-Cu and Cp_6 in NT8e cells after PDT under normoxia and hypoxia.	102
Figure 5.1. Intracellular uptake of ICp_6-Cu as a function of concentration in NT8e and 4451 cells.	109
Figure 5.2. Cytotoxic effects of X-ray without and with ICp_6-Cu pretreatment in oral cancer cells determined by MTT assay.	110
Figure 5.3. Radiosensitization effect of ICp_6-Cu in oral cancer cells determined by clonogenic assay.	111
Figure 5.4. Effects of ICp_6-Cu and X-ray irradiation on ROS generation.	113
Figure 5.5. Effect of ICp_6-Cu and X-ray irradiation on DNA damage determined by γ -H2AX immunostaining.	114
Figure 5.6. Changes in percentage of γ -H2AX foci in oral cancer cells treated with or without ICp_6-Cu at different time periods postirradiation.	115
Figure 5.7. Confocal fluorescence micrographs of NT8e cells showing the effect of ICp_6-Cu induced radiosensitization on the integrity of lysosomes and ER.	116
Figure 5.8. Effect of ICp_6-Cu and X-rays irradiation on cell cycle distribution 24 h post- irradiation.	117

Figure 6.1. Effect of ICp_6 -Cu and Cp_6 treatment on the viability of NT8e, 4451 and HaCaT cells.	124
Figure 6.2. Time-dependent effect of ICp_6 -Cu treatment (10, 20 and 50 μ M) on the proliferation of NT8e and 4451 cells.	125
Figure 6.3. Photomicrographs of control and ICp_6 -Cu treated HaCaT, NT8e and 4451 cells.	126
Figure 6.4. Confocal fluorescence photomicrographs of control and ICp_6 -Cu treated NT8e and 4451 cells showing F- actin filaments of cytoskeleton.	127
Figure 6.5. Confocal fluorescence photomicrographs of control and ICp_6 -Cu treated NT8e and 4451 cells showing AO stained lysosomal acidic vesicles.	128
Figure 6.6. Changes in the levels of intracellular ROS relative to control in HaCaT and NT8e cells at different time periods after treatment with ICp_6 -Cu.	129
Figure 6.7. Percent cell viability and cell proliferation of ICp_6 -Cu treated NT8e and 4451 cells without and with GSH and Trolox pretreatment.	130

LIST OF TABLES

Table 1.1. Photophysical properties of some second generation photosensitizers.....	20
Table 2.1. No. of scans and corresponding calculated absorbed dose.	55
Table 3.1. Octanol/ water partition coefficient of Cp_6 and ICp_6-Cu	69
Table 3.2. Absorption characteristics of ICp_6-Cu with various concentration of HSA.	74
Table 3.3. Average fluorescence lifetime (τ_{avg}) of ICp_6-Cu and Cp_6 in presence and absence of HSA.	74
Table 4.1. Intracellular uptake of Cp_6 and ICp_6-Cu in cancer cells.	96

LIST OF ABBREVIATIONS

μl	Microliter
μM	Micromolar
Φ_{Δ}	Singlet oxygen quantum yield
Φ_{T}	Quantum yield of triplet excited state
τ_{T}	Lifetime of triplet excited state
APF	3'-(p-Aminophenyl) fluorescein
BCA	Bicinchoninic acid
Chl-a	Chlorophyll- a
Cp_6	Chlorin p_6
$Cp_6\text{-CuI}$	Chorin p_6 – Copper iodide conjugate
DMEM	Dulbecco's modified essential Media
DMF	Dimethylformamide
DMSO	Dimethyl sulfoxide
D_2O	Deuterium Oxide
EDTA	Ethylenediaminetetraacetate
ER	Endoplasmic reticulum
FBS	Fetal bovine serum
GSH	Reduced glutathione
HEPES	N-2-hydroxyethylpiperazine-N'- 2- ethanesulphonic acid
HO	Hoechst 33342
Hp	Hematoporphyrin
HSA	Human serum albumin
H_2O_2	Hydrogen peroxide
H_2DCFDA	2, 7'-dichlorodihydrofluorescein diacetate

ICp ₆ -Cu	Iodinated Chlorin p6 copper complex
ISC	Intersystem crossing
MTT	3(4,5-dimethylthiazol-2-yl)2,5 diphenyltetrazolium bromide
NaOH	Sodium Hydroxide
NaN ₃	Sodium Azide
O ₂ ⁻	Superoxide anion
[•] OH	Hydroxyl Radical
¹ O ₂	Singlet Oxygen
OSCC	Oral squamous cell carcinoma
PAT	Photon-activation therapy
PBS	Phosphate buffer saline
PDT	Photodynamic therapy
PI	Propidium Iodide
PMT	Photomultiplier tube
PS	Photosensitizer
PS ^{1*}	Singlet excited state of photosensitizer
PS ^{3*}	Triplet excited state of photosensitizer
ROS	Reactive oxygen species
SDS	Sodium dodecyl sulfate
SD	Standard deviation
SER	Sensitivity Enhancement Ratio
SOSG	Singlet Oxygen Sensor Green
TBS	Tris-buffered saline

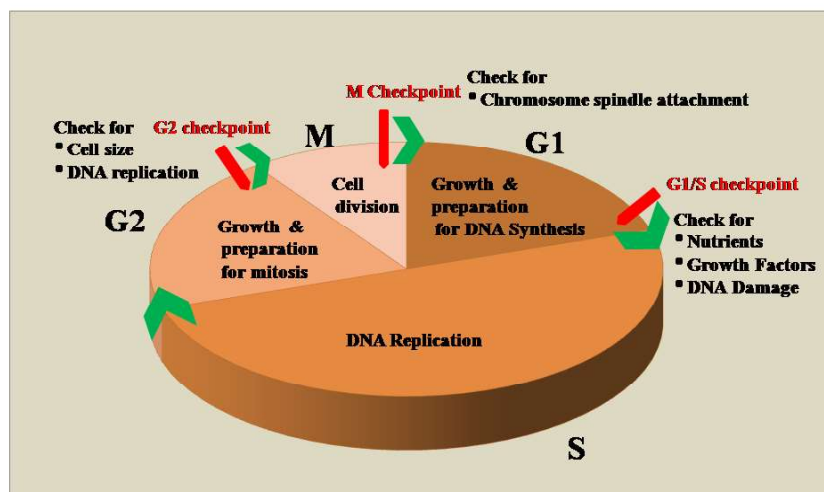
Chapter 1

Introduction and Review of Literature

Cancer remains one of the major health problems and leading cause of death worldwide. Despite the significant technological advancements in both diagnosis and treatment of cancer, new cases of almost all types of cancer are rising globally. According to GLOBOCAN statistics- 2012, about 14.1 million new cancer cases and 8.2 million cancer deaths have been reported worldwide and the incidence of the disease is expected to rise by ~ 70% in next 2 decades [1,2]. In India cancer has become third fatal disease accounting for ~ 0.7 million deaths in the year 2012 and about 1 million new cases of cancer are diagnosed annually. It is estimated that cancer burden will double in the next 20 years [2, 3, 5]. According to WHO, major types of cancer among men are lung and oral cancers while among women cancer of cervix and breast are the most common in India [6].

Cancer arises as a result of deregulation of cell division process leading to excessive cell proliferation. A normal cell grows, replicates its DNA and divides via tightly regulated cell cycle involving activity of hundreds of genes that intricately control a series of signaling and checkpoints during the progression of cell cycle. As illustrated in the scheme 1.1, the cell cycle comprises of four phases, G1, S, G2, & M involving three checkpoints at G1/S, G2/M and M phases that ensure proper division of cells by avoiding DNA damage and mutations. At G1/S checkpoint, the cell determines whether or not to replicate its DNA and checks DNA damage. G2 checkpoint ensures that all of the chromosomes have been accurately replicated without error before entry into M phase. At both the G1/S and G2 checkpoints, cells with damaged DNA are arrested in an attempt to repair the damages and if the DNA remain unrepaired, then these checkpoints signals for induction of programmed cell death, known as apoptosis. M checkpoint occurs near the end of the metaphase stage

of mitosis which ensures that all the sister chromatids are correctly attached to the spindle microtubules. Uncontrolled cell proliferation or induction of carcinogenesis is associated with mutation in one or more genes that regulate these checkpoints. This mainly involves mutation in two classes of genes: proto-oncogenes (involving gain of function) and tumor suppressor genes (involving loss of function). Proto-oncogenes are positive regulators of carcinogenesis which promote cell growth and differentiation, while tumor suppressor genes are involved in inhibition of cell division, thus act as negative regulator of carcinogenesis [7, 8]. In this respect, deregulation of G1/S checkpoint is considered to be the most crucial event that leads to oncogenic defects. This is because the G1/S regulators are mainly proto-oncogenes (cyclins D1, D2 and E, CDK4/6, CDC25A) or tumor suppressors (the p15, p16, p21, p27, and p57 CDK inhibitors and pRB) [7].

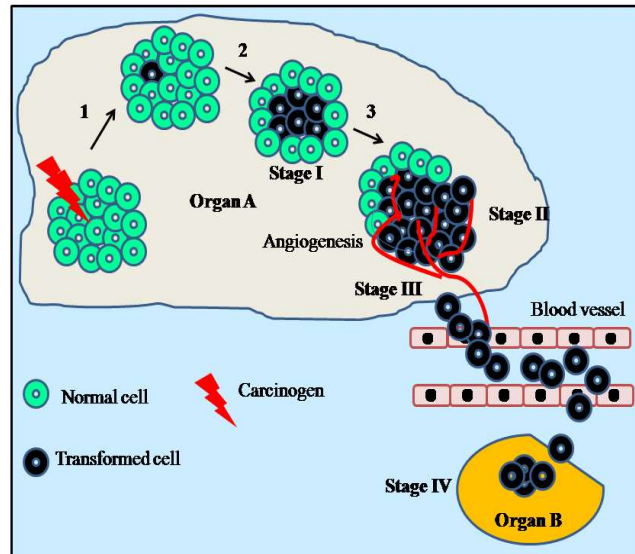


Scheme 1.1. Schematic representation of Cell cycle phases and checkpoints. G1 phase (1st Gap phase), is the postmitotic phase where the newly formed cells accumulate nutrients, grows and prepares itself for DNA synthesis. In S phase (Synthesis phase), DNA replication takes place resulting into doubling of DNA content. G2 phase (2nd Gap phase), is the premitotic phase when the cell grows in size and prepares to divide. M phase (mitosis) involves karyokinesis (nuclear division) and cytokinesis (cytoplasmic division). The cell cycle is regulated by 3 major checkpoints at G1/S, G2 and M phases.

The development of tumor after the loss of control on cell proliferation is a multistage process in which the transformed cells initially grow into a compact mass referred to as 'benign' tumor (Scheme 1.2). The benign tumor then acquires ability to promote angiogenesis, evade growth suppressors and immune system, and turns into relatively rapidly growing 'malignant' tumor. As the malignant tumor grows in size, it invades the surrounding tissue and then spread to distant organs via the process known as metastasis. Uncontrolled metastasis is the leading cause of death in cancer patients, as this interferes with the normal functioning of the body by destroying other healthy tissues [9].

1.1. Cancer treatment modalities

Cancer is conventionally treated by surgery, radiotherapy and chemotherapy. The common goal of these treatments is removal and/ direct or eventual killing of cancer cells. Surgery involves operative removal of primary tumors (stage I) and/ associated tissue /organ and usually practiced in combination with radio and chemotherapy. Over the past 25 years, research in cancer therapeutics have led to significant developments not only in conventional therapies but also provided some novel approaches of cancer treatments which holds considerable potential to treat cancer with better efficacy and improved outcome. Among these photodynamic therapy (PDT) and photon-activation therapy (PAT) that involve tumor selective agents in combination with light and/or radiation have received significant attention. In this chapter, first, a brief overview is presented on the recent scenario of radiotherapy and chemotherapy and existing limitations. This is followed by review on PDT, and application of metal-based photosensitizers (PSs) for combined treatment modalities.



Scheme 1.2. The three-phase process of carcinogenesis. 1. Initiation is the first step in cancer development, where a carcinogen (chemical agent and/or ionizing radiation) causes permanent genetic change resulting into abnormal and transformed cell. 2. Promotion step involves uncontrolled proliferation of transformed cells into a large number of daughter cells (clonal expansion) containing the mutation created by the initiator. Clonal expansion results into a mass of transformed cells known as benign tumor. 3. The third step, progression refers to the serial transformations from a benign tumor to a neoplasm finally leading to a rapidly growing malignant tumor having properties of invasiveness and metastasis. Metastasis process involves: detachment of tumor cells from the primary mass, invasion into local host tissue stroma, lymphatic and blood vessels and migration to other organs to form a new tumor. Cancer staging is a way of describing the size of a cancer and how far it has grown, at the time of first diagnosis. Stage I: Cancer is usually small and localized within the organ it started. Stage II: Cancer is larger but has not spread to surrounding tissue. Stage III: Cancer is larger and it may have started to spread into surrounding tissues and lymph nodes in the area but not to other parts of the body. Stage IV: Cancer has spread to other organs or parts of the body. This is also known as secondary or metastatic cancer.

1.1.1. Radiotherapy

The conventional radiation therapy of cancer refers to the use of ionizing radiation (IR) to kill actively dividing cells. Low LET (linear energy transfer) X-rays and γ -rays are the most common form of radiation used to treat various cancers due to their deeper penetration in the body. While high LET alpha, beta particles, electron, proton and neutron beams are commonly used to treat tumors close to body surface since they do

not penetrate deeply into tissues. Radiation generally target and induce DNA damage, either by direct interaction and ionization of DNA (direct effect) or by an indirect mechanism involving radiolysis of water and generation of free radicals in the near vicinity of the nucleus (indirect effect). Since the anticancer action of IR is mediated through induction of DNA damage, its effectiveness depends on the distribution of cells in different cell cycle phases. Cells in G2 and M stage are most sensitive, G1 and early S phase shows intermediate sensitivity while those in S stage are least sensitive. DNA damage through activation of cell cycle checkpoints leads to cell cycle arrests at G1, S, and G2 phases. The cell cycle arrest is either temporary that permits time for genetic repair or irreversible growth arrest that results in cell death (necrosis or apoptosis) [10, 11].

The era of radiotherapy for cancer treatment started in 1920s using γ -radiation emitted from radium tubes, needles and Coolidge tubes. The main milestone in this field was achieved in 1928 when it was shown that head and neck cancers could be cured by fractionated radiation therapy [12]. However, since the external beam radiotherapy (EBRT) with energies between 200 kV and 500 kV was unable to deliver sufficient doses into deep-seated tumors, its application was limited to either small superficial tumors (skin and vocal cord) or to intrinsically radiosensitive cancers (Hodgkin lymphoma and seminoma); and also the application of brachytherapy was limited to 'accessible' tumours (tongue, anal or uterus cancers). Further, the routine use of radiotherapy was associated with unavoidable skin toxicity [13, 14].

A major breakthrough in cancer radiotherapy happened in 1960s with the introduction of cobalt source and linear accelerators. These radiation sources due to capability of producing high energy radiation in the low MV range made it possible to

treat tumors deep inside the body for the very first time. In 1980s computer-assisted radiotherapy combined with CT imaging was introduced which shifted the treatment planning from 2D to 3D (3D conformal radiotherapy). Later, technological advances in imaging modalities such as magnetic resonance imaging (MRI) and positron emission tomography (PET) together with development of novel radiotherapeutic approach such as intensity-modulated radiation therapy (IMRT) and image-guided radiation therapy (IGRT) have made it possible to better see and target tumors, with better treatment outcomes, more organ preservation and fewer side effects. Thus, radiotherapy has become a major treatment modality for cancer worldwide [15-17].

1.1.2. Chemotherapy

Chemotherapy involves administration of chemical agents that can either inhibit cell proliferation or induce cell death in cancer cells through various mechanisms. One main advantage of chemotherapy is its systemic effect and thus applicable for all stages of cancer. In fact, the focus for cancer cure was shifted to the search of chemotoxic drugs because radiation therapy could not eradicate metastatic cancer [18]. Nitrogen mustard was the first chemotherapeutic drug approved by the Food and Drug Administration (FDA) in 1949 for the treatment of Hodgkin lymphoma. However, a seminal progress in chemotherapy of cancer took place in 1958, when Hertz and Li demonstrated the potential of methotrexate to cure solid tumors in humans [19]. In 1965, Barnett Rosenberg demonstrated the effectiveness of cisplatin, a platinum-containing compound against sarcoma and leukemia in mice, which stimulated researchers to investigate other platinum and non-platinum metal-containing compounds for the treatment of cancer [20]. Cisplatin was clinically

approved in 1978 for the treatment of bladder, testicular and advanced ovarian cancer. The use of cisplatin was limited due to side effects and development of resistance in tumors and to overcome these limitations other platinum-based drugs were investigated which led to clinical approval of two more platinum drugs, carboplatin and oxaliplatin in 1990s. In the same period, many other cytotoxic drugs such as paclitaxel, gemcitabine, valrubicin etc. which target microtubules, DNA synthesis and topoisomerases respectively, were also approved by FDA for treatment of various cancers [21]. Later, extensive research led to better understanding of the molecular aberrations that occur in cancer cells and as a result, the scenario of chemotherapy changed from non-specific agents to compounds that act on specific critical molecular targets [12, 22]. Till date, FDA has approved several small molecule inhibitors such as imatinib, gefitinib, bortezomib, brigatinib etc., and other cytotoxic agents such as eribulin, uridine triacetate, topotecan etc., for the treatment of various cancers worldwide [23]. A brief overview of various chemotherapeutic drugs and their mechanism of action are given below.

(a) Cytotoxic agents: Most of the FDA approved chemotherapeutic drugs are based under this category. These drugs target either vital biomolecules such DNA, microtubules and topoisomerases or metabolic pathways. e.g. DNA binding alkylating agents (cisplatin, oxaliplatin, temozolomide), microtubule-active drugs (navelbine, docetaxel, paclitaxel), inhibitors of topoisomerase I (irinotecan, topotecan), topoisomerase II (valrubicin), antimetabolites (capecitabine, gemcitabine, cladribine, pemetrexed) and proteasome inhibitor (bortezomib) [21].

(b) Cancer-selective agents: This class of drugs includes small molecule inhibitors having molecular weight of approximately 500 Dalton, which enter cells and thereby blocks receptor signaling and interferes with downstream intracellular molecules. The name of these drugs generally ends with the stem "-ib" (indicating that the agent has protein inhibitory properties) [24-26]. These drugs often target proteins such as epidermal growth factor receptor (EGFR, also known as HER1 and HER2/neu), vascular endothelial growth factor (VEGF) and intracellular tyrosine kinases which are responsible for cell proliferation, cell-cycle regulation, and angiogenesis respectively [21]. For example, Imatinib used in the treatment of chronic myeloid leukemia inhibits a constitutively active Bcr-ABL tyrosine kinase, gefitinib and erlotinib used in the treatment of non-small cell lung cancer (NSCLC) inhibits the epidermal growth factor receptor (EGFR) kinase, lapatinib used in the treatment of ERBB2-positive breast cancer act specifically on the EGFR/ERBB2 and sorafenib used in the treatment of renal cancer inhibit vascular epidermal growth factor receptor (VEGFR) kinase [23].

1.1.3. Chemoradiotherapy

Although both radiation therapy and chemotherapy alone were significantly useful for clinical management of cancer, the occurrence of severe side effects and development of resistance in tumor limited the application of both these therapies. To circumvent these issues, Steel and Peckham in 1979 proposed the use of chemotherapy agents in combination with radiation which was based on the hypothesis of "spatial cooperation" between mode of action of chemo and radiotherapy. This hypothesis states that the combined action of the two modalities can lead to increased killing of cells (cytotoxic

activity) either by additive effect that combines the individual damage mechanism or by supra-additive effect that involves augmentation of damage induced by each treatment [27]. With the advancement in the understanding of cancer at the molecular level, the scenario for cancer treatment has shifted from the sole dependence on chemo and radiotherapy to combined chemoradiotherapy [28]. The application of chemoradiotherapy offers improved treatment outcomes in case of radioresistant tumors and distant micrometastases with lower systemic toxicity [27]. Enhancement of therapeutic efficacy by combined chemoradiotherapy involves following mechanisms of interaction between chemotherapy and radiotherapy [27].

1) Increased radiation damage: Where DNA damage is induced by both chemotherapy and radiotherapy and interaction of both therapies results into synergy. For e.g. interaction of cisplatin with DNA results into increase in susceptibility to radiotherapeutic damage. Radiation-induced free radicals results into enhanced formation of toxic platinum intermediates (radicals) which further increases DNA damage [29].

2) Inhibition of DNA repair: Certain chemotherapeutic agents interfere with the DNA repair process after radiation. For e.g. halogenated pyrimidines (e.g. 5-FU, bromodeoxyuridine, iododeoxyuridine), nucleoside analogs (e.g. gemcitabine, fludarabine), cisplatin, methotrexate, camptothecins, doxorubicin, etoposide, hydroxyurea, carmustine, lomustine etc. Among which, fluoropyrimidines, thymidine analogs, gemcitabine, and hydroxyurea, which acts by affecting nucleoside and nucleotide metabolism are among the most potent radiation sensitizers in patients.

3) Cell-cycle interference: Most cytotoxic chemotherapeutic agents as well as ionizing radiations are specific to a particular cell-cycle phase and thus co-operate to produce an additive effect. Cells in the S phase are the most radio-resistant, and cells in the G2/M phase of the cell cycle are the most radiosensitive. Cytokinetic cooperation of S-phase specific agents such as camptothecins, 5-FU, hydroxyurea, results into elimination of radioresistant cells in the S phase. Other drugs such as taxanes arrest cell cycle resulting in synchronization of cells which increases the efficacy of subsequent radiotherapy.

4) Enhanced activity against hypoxic cells: Hypoxic cells are 2.5–3.0 times less radiation-sensitive than normoxic cells, and is one of the leading causes of failure of radiotherapy. Chemotherapeutic drugs such as tirapazamine, and mitomycin C, preferentially kill hypoxic cells. Also, paclitaxel and EGFR inhibitors, causes shrinkage of tumors, thus leading to reoxygenation and reducing radioresistant hypoxic areas.

5) Enhancement of radio-therapeutic efficacy by preventing repopulation: Repopulation of rapidly proliferating tumors is one of other cause of radio-resistance, thus agents that target the S phase of the cell cycle, such as 5-FU, irinotecan, and hydroxyurea, as well as those that inhibit proliferation and/or growth factor pathways, such as EGFR inhibitors, may be effective in preventing tumor cell repopulation. This maximizes the radiotherapeutic outcome efficacy.

1.2. Pitfalls and challenges of cancer therapies

Whilst radio and chemotherapy either alone or in combination are effective therapy against cancer, their success has been limited mainly due to two important issues. First is the harmful side effects that arise because of cytotoxicity to normal cells. Since these treatment modalities target rapidly dividing cells, they also inhibit the proliferation of normal cells such as hair follicles, gastrointestinal epithelium and bone marrow which are required for maintaining normal body function and appearance. Chemotherapeutic drugs are known to produce side effects such as peripheral nerve damage, severe allergic reactions, immune-suppression and anemia due to adverse effects on bone marrow cells, ulceration of mouth (mucositis), diarrhea, nausea, vomiting, fever and distended abdomen etc. In addition, Cardio-toxicity, hepatotoxicity, nephrotoxicity and ototoxicity, are some of the leading problems associated with application of chemotherapeutic drugs [30].

The second main drawback of conventional radio and chemotherapy is the development of resistant cancer cell population after the treatment. For example, cancer cells often exhibit mutation in genes related to programmed cell death and thus display resistance to radio and chemotherapy. Resistance to chemotherapeutic agents is acquired through expression of surface-pumps like p-glycoprotein and intracellular antioxidant efflux that prevent entry of these drugs into the cells. In addition, certain biological features of tumors can limit the effectiveness of radiotherapy; for example, the extent and degree of hypoxia, the ability of the surviving cells to repopulate within the treatment time (typically 6–7 weeks for conventionally fractionated radiotherapy) [31].

Similarly, targeted anticancer therapy (TATs) which was designed to act on specific molecular targets is also associated with several toxic effects and has generally failed to produce expected therapeutic outcome because of several pitfalls [31]. The common side effects of TATs includes hypertension, fatigue, bone marrow toxicity, skin toxicity, gastrointestinal side-effects as well as immune-suppression, metabolic alterations, interstitial pneumonitis, and hypothyroidism [32]. For example, EGFR targeted drugs affects normal epithelial tissue (i.e., skin and mucosa) and lead to significant dermatologic and gastrointestinal toxicities, causing skin rashes and diarrhea. Similarly, targeting VEGF is associated with adverse effects on normal blood vessels, leading to toxicities such as bleeding, thrombosis, hypertension, and proteinuria [28].

The two main causes of failure of TATs are emergence of resistance and tumor heterogeneity. For example, drugs such as crizotinib and vemurafenib which demonstrated therapeutic efficacy under clinical trials have suffered the drawback of emergence of resistance [26]. Resistance to molecularly targeted agents can be due to mutation of the target itself, as in the case of kinase gatekeeper mutations and/or the activation of adaptive feedback loops or alternative oncogenic pathways [26]. In addition, tumor heterogeneity plays an important role in limiting the efficacy of targeted drugs and their outcome. Cancer cells within a tumor, as well as tumors of the same type in different patients, display heterogeneity with respect to morphological and phenotypic characteristics such as cellular morphology, gene expression, metabolism, motility, proliferation, and metastatic potential [33]. In addition, the heterogeneous cancer cell population in tumor includes a sub-fraction of drug-resistant

stem cells which are capable of reconstituting the tumor after the treatment and the resulting tumor is dominated by resistant cells [34].

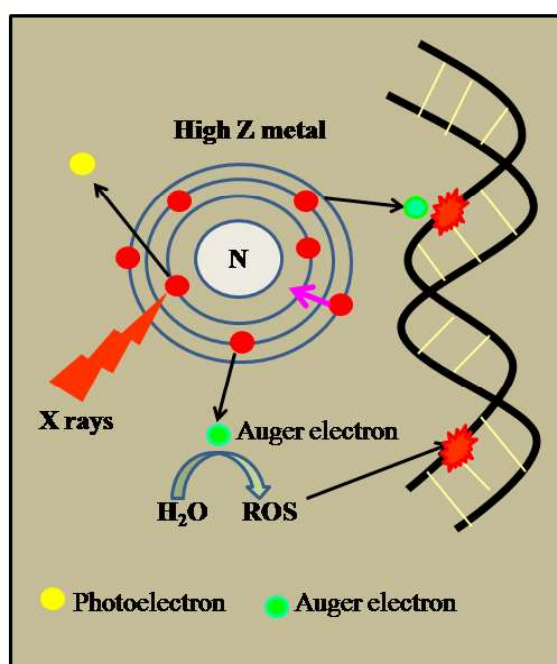
1.3. Novel chemoradiotherapy based treatment modalities

1.3.1. Photon-activation therapy (PAT)

In chemoradiotherapy, the drug and radiation act independently to result in improvement of the therapeutic outcome. Fairchild et al., in 1982 introduced another form of chemoradiotherapy known as photon-activation therapy (PAT), where a metal-based compound having X-ray absorption property was primarily used to enhance X-ray dose deposition in tumor cells [35]. The drug candidates for PAT contain high Z atom (Pt, Au, I or Br,) and generally designed with the purpose to target the nucleus in tumor cells. The tumor is then irradiated with X-ray of energy slightly above the K-edge absorption of the metal. The photon-activation of metal leads to the emission of Auger electrons and photoelectrons, which in turn reacts with nearby biomolecules or induces the formation of free radicals through radiolysis of water to cause direct or indirect cellular damage. This phenomenon is known as photoelectric effect and is illustrated in scheme 1.3. Thus, the photon absorption by metal contributes to the enhancement of energy deposition such that efficient tumor damage can be achieved even with low irradiation dose [35-38].

The biological effectiveness of PAT has been demonstrated in several studies. Shinohara, Ohara and co-workers demonstrated that irradiation of 5-bromodeoxyuridine treated HeLa and Chinese hamster ovary (CHO) cells with monochromatic synchrotron radiation induced higher killing rate with the irradiation of energy at the K-absorption edge (~ 12.40 keV) of bromine than above K-edge

(13.78 keV) [39, 40]. Similarly, Larson et al showed ~ 3-12 % increase in radiosensitization in Chinese hamster V79 cells after treatment with BUdr and X-ray irradiation above the K-edge absorption of Br as compared to radiation energy below K-edge [41]. X-ray irradiation (at National Synchrotron Light Source of Brookhaven National Laboratory) of Chinese hamster V79 cells treated with IdUrd showed more killing efficiency with monochromatic photons above (33.4 keV) than below (32.9 keV) iodine K-edge [35].



Scheme 1.3. Interaction of X-rays with high-Z element, results into DNA damage. X-rays strike an inner shell electron causing ejection of the electron (photoelectron), to fill the vacancy, an electron of an outer shell (higher energy state) drops into the lower energy shell. The energy difference between the two shells is then transferred to another electron which is ejected from an outer shell (Auger electron). Thus one vacancy in the inner shell is converted into two vacancies in an outer shell. If another outer shells exist in the atom, these two vacancies can be filled with other electrons and a succession of further Auger electron ejections takes place, resulting into an Auger cascade. Auger electrons have lower energy (~20–500 eV) and shorter range (<1 μm). Emission of multiple auger electrons either directly deposit their energy on DNA, and/or result in water hydrolysis and production of ROS which indirectly leads to DNA damage.

Currently, platinated drugs (cisplatin, carboplatin) and iodinated compounds in combination with X-ray are actively investigated for the treatment of radio-resistant brain cancer [42-46]. Recently, Ceresa et al. reported that cisplatin plus irradiation with synchrotron X-ray produce substantially higher cell killing compared to conventional X-ray irradiation in highly resistant Glioblastoma multiforme cells [47].

1.3.2. Photodynamic therapy (PDT)

In last two decades, photodynamic therapy (PDT) has emerged as a promising therapeutic modality for cancer [48-51]. PDT utilizes photoactivable drug referred as PS followed by irradiation with red or near-infrared light to induce tumor damage via generation of reactive oxygen species (ROS). PDT offers several advantages such as selective killing of cancer cells, lower risk of developing resistance and less systemic toxicity as compared to chemo and radiotherapy [52]. In PDT, the tumor selectivity is achieved in a dual manner, first using a photosensitizer (PS) which preferentially localizes in malignant tissue and then confining the irradiation to the affected site using an intense beam of light either from non-coherent light sources (e.g., arc lamps) or laser/fiber optic systems. Tumor regression induced by PDT is a consequence of complex mechanisms involving direct tumor destruction, tumor vasculature shutdown and anti-tumor immune response [49-51]. Currently, PDT is clinically approved for the treatment of several types of cancer such as breast cancer, gynecological tumors, intraocular tumors, brain tumors, head and neck tumors, colorectal cancer, cutaneous malignancies, intraperitoneal tumors, mesothelioma, cholangiocarcinoma and pancreatic cancer [54-56].

1.3.2.1. Photophysical and Photochemical mechanism of PDT

The phenomenon of photosensitization was documented more than 100 years ago by Oscar Raab who observed that acridine in combination with light irradiation was able to induce a strong cytotoxic effect in paramecia. Later, in 1903, von Tappeiner and Jesionek published results on the use of eosin and light for the treatment of skin cancer and coined the term 'Photodynamic therapy' (PDT) for the first time [48, 57, 58]. In the process of photosensitization, a photosensitive compound absorbs light energy and transfers it to nearby substrate molecules via photophysical and photochemical processes. In the photophysical process, the PS molecule after absorption of light is excited from its ground state (PS^0) to its short-lived (nanoseconds) excited singlet state ($^1PS^*$). The $^1PS^*$ state either directly decay back to its ground state releasing energy in the form of a photon emission (fluorescence) or heat (non-radiative decay) or converted into longer lived and chemically more reactive excited triplet state $^3PS^*$ via intersystem crossing (ISC). This $^3PS^*$ can either decay to ground state radiationlessly or undergo photochemical reactions via type I and/or type II mechanisms. Type I process involves hydrogen-atom abstraction or electron transfer process from $^3PS^*$ to nearby biological substrate or O_2 molecules to result in the formation of free radicals and radical ions. Further, the highly reactive free radicals of a substrate molecule can readily interact with O_2 to either generate ROS such as superoxide anions ($O_2^{\cdot-}$) or hydroxyl radicals ($\cdot OH$) or can cause irreparable biological damage. In type II pathway $^3PS^*$ transfer its energy to molecular oxygen (O_2) to form singlet oxygen (1O_2). The resulting ROS oxidize biomolecules such as nucleic acids, amino acids or unsaturated lipids eventually leading to cell death. Both

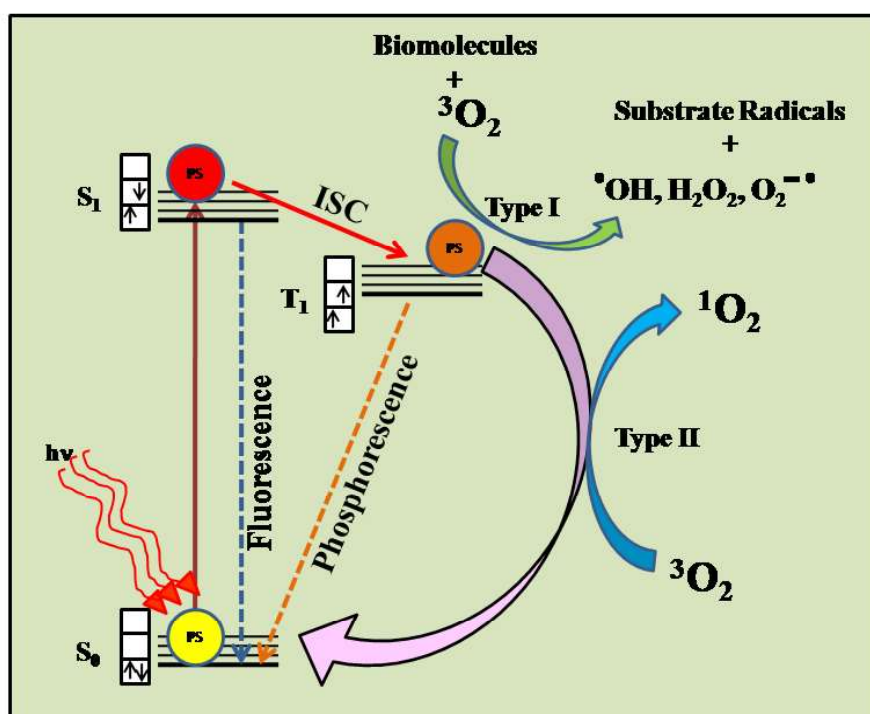
processes occur simultaneously but the prevalence between them depends upon PS property, availability of O₂ and surrounding environment [50, 59-61].

1.3.2.2. Photosensitizers in PDT

The majority of PSs that have been investigated for potential use in PDT are derivatives of porphyrins, chlorins, bacteriochlorins, phthalocyanines and texaphyrins [50, 59, 62]. The application of porphyrins as PS was reported early in 1913, by Friedrich Meyer–Betz, however, its use for oncological applications started in the 1960s after the demonstration by Lipson and Baldes that neoplastic tissues fluoresce under ultraviolet light due to the accumulation of porphyrins [48, 58, 63]. Later it was found by Schwartz that hematoporphyrin derivative (HpD), a porphyrin mixture prepared from hematoporphyrin accumulated better in tumor tissue and produced higher phototoxicity [63]. Detailed preclinical and clinical studies by Dougherty et al. in 1970s on phototherapeutic potentials of HpD led to the development of Photofrin, a purified preparation of HpD and its approval by US FDA for clinical applications. Within few years, PDT with Photofrin became an attractive modality for the treatment of various malignant diseases in several countries [63].

Photofrin is most commonly used PDT agent for treatment of many different types of cancer. However, Photofrin suffers from some major drawbacks including poor pharmacokinetics, prolonged skin photosensitivity and low absorbance in the red wavelength region which limited the effectiveness of PDT [64]. Subsequently, in search of new improved PSs, derivatives of chlorins, benzoporphyrins, phthalocyanines, and porphycenes were investigated which were classified as second generation PDT agents [65, 66]. These second generation PSs offered better PDT

efficacy through improved photophysical characteristics such as high absorption coefficient in the red wavelength region, higher yield of long-lived $^3\text{PS}^*$ and efficient generation of $^1\text{O}_2$ [62, 64, 67]. The photophysical characteristics of some second generation PSs are presented in table 1.1. Among various types of PSs, phthalocyanines provided most suitable photophysical characteristics; however, due to poor aqueous solubility, these tend to aggregate in the physiological media environment and lose their photodynamic activity [68].



Scheme 1.4. Schematic illustration of Jablonski diagram including photochemical reactions. When a photon ($h\nu$) is absorbed by the PS, it is excited from ground state (S_0) to excited singlet state (S_1). Excited PS can lose energy by emitting a photon (fluorescence). Otherwise, the excited PS undergoes non-radiative decay to the excited triplet state (T_1). This process is known as intersystem crossing (ISC) which involves flipping of the spin of the high-energy electron, leading to a long-lived excited triplet state. Excited triplet state of PS can relax back to the ground state in a radiative decay process known as phosphorescence. Otherwise, the triplet excited PS can undergo two different photochemical reactions: type I and type II process. In type II reactions ^3PS interact with molecular oxygen, leading to the formation of singlet oxygen. While in type I process ^3PS reacts with molecular oxygen and surrounding biomolecules and result into the formation of superoxide, hydroxyl and bimolecular radicals.

Table 1.1. Photophysical properties of some second generation photosensitizers

Photosensitizers	λ_{\max} (nm)	ϵ ($M^{-1}cm^{-1}$)	Φ_{Δ}
Benzoporphyrin derivative monoacid ring A (BPD-MA)	689	34,000	0.84
Meta-tetra(hydroxyphenyl)chlorin (m-THPC)	652	35,000	0.87
N-aspartyl chlorin e6 (NPe6)	664	40,000	0.77
Palladium bacteriopheophorbide (WST09)	763	88,000	0.50
Silicon phthalocyanine (Pc4)	680	200,000	0.68

Chlorins due to strong absorption in the red wavelength region of the visible spectrum (650–700 nm) have been considered most suitable for PDT applications [64]. As compared to porphyrin, a peripheral double bond in one of the pyrrole ring is reduced which results in decrease in the symmetry of the conjugated macrocycle, leading to an increased absorption in the red wavelength region. Of the purely synthetic chlorins, 5,10,15,20-tetra(3-hydroxyphenyl)chlorin (m-THPC) was recently approved for marketing and etiopurpurinato- Sn(IV) (SnET2) is close to being commercialized. Other chlorin based synthetic purpurin, tin(II) etiopurpurin have advanced to Phase II clinical trials (USA) for cutaneous metastatic breast cancer and Kaposi's sarcoma in patients with AIDS. Verteporfin a synthetic Benzoporphyrin derivative monoacid ring A'' (BDP-MA), chlorin-type PS has shown promising photophysical properties and currently undergoing Phase II clinical trials for the treatment of solid tumors. Another chlorin derivative, Meso-tetra-hydroxyphenyl-chlorin (Foscan, Temoporfin) has been approved in Europe for the palliative treatment of head and neck cancers [64].

As compared to synthetic chlorins, substituted derivatives of chlorin and bacteriochlorin obtained from the naturally occurring chlorophylls (Chl) and bacteriochlorophylls (BChl) have received much attention as PDT PSs, because they can be prepared easily in large amount from plants and algae. Radachlorin® containing mixture of three water-soluble chlorophyll derivatives is clinically approved and has been shown to be effective for PDT of central airway obstruction in advanced non-small cell lung cancer (NSCLC) patients [69]. A more purified chlorophyll derivative Chlorin e_6 and its mono-aspartyl derivative ($MACe_6$) have been studied extensively and proven to be efficient PSs both *in vitro* and *in vivo*. As compared to HpD, these chlorophyll derivatives have higher photosensitization ability and do not cause prolonged photosensitivity after PDT. $MACe_6$ is undergoing phase I or phase II clinical trials for the treatment of cutaneous cancers. The mono-aspartyl derivative (laserphyrin, taloporphin sodium or LS11) has been used in Japan [64]. Like Ce_6 , Cp_6 is a hydrophilic PS, and has been found to be phototoxic. The anhydride ring of (purpurin) PP_{18} is cleaved by nucleophiles. Therefore, PP_{18} is not stable in the body, because biomolecules, such as proteins, can act as nucleophiles in *in vivo*. However, the opening of the anhydride ring can lead to the formation of a photoactive compound [64]. As an example, the hydrolysis product of PP_{18} , Cp_6 , has been found to be phototoxic in *in vitro*. Pandey et al. have synthesized a series of amphiphilic derivatives of chlorin based pyropheophorbide a, among which hexyl ether analogue of PyroPheid a (HPPH) hexyloxy derivative, is regarded as a promising PS candidate for PDT and has been approved for clinical trials in USA for treatment of cancer [50, 64, 70].

In bacteriochlorins, two double bonds on the opposite sides of the macrocycle are reduced, which strengthens and moves their absorption even further to the red. A bacteriopheophorbide derivative known as TOOKAD [WST09], a lipophilic, water-soluble derivative of the natural pigment Bchl with an incorporated palladium (Pd) atom, have been tested in clinical trials for prostate cancer. A related water-soluble Pd-bacteriochlorin derivative called WST11 has been tested for PDT of mouse melanoma xenografts. A recent report has shown that the application of bacteriochlorin p_6 is effective for *in vitro* and *in vivo* treatment of light-induced fibrosarcoma (RIF) tumors [71]. But, naturally derived bacteriochlorins are usually unstable in the presence of O₂ and light and are rapidly converted to chlorins and porphyrins [72]. 5,10,15,20-Tetra(3-hydroxyphenyl) bacteriochlorin (m-THPBC) is a fully synthetic bacteriochlorin that has been developed for commercial use. The new synthetic bacteriochlorin derivative Fluorinated sulfonamide bacteriochlorin, known as LUZ11 recently entered clinical trials for head and neck cancer in Portugal [73]. Other synthetic bacteriochlorins have also been tested as PSs for anti-cancer applications [50, 72].

1.3.2.3. Limitations of PDT

1) ***Low treatment depth:*** The effectiveness of PDT has been demonstrated in several clinical studies including the cancers which failed to respond to traditional treatments. However, due to limited penetration of light in tissue, the application of PDT is limited as palliative surface treatment [49].

The penetration depth of light in tissues depends mainly on optical properties of tissues and the wavelength of light used. The shorter visible wavelengths (400- 600 nm) do not penetrate in tissue more than a millimeter due to the scattering and absorption of light by endogenous macromolecules and chromophores (flavins, hemoglobin, melanin, etc.). At the longer wavelengths between 600 nm to 850 nm, the scattering and absorption of these chromophores is low and therefore light of this wavelength range penetrates more deeply (several millimeters) in the tissue [74, 75]. While wavelengths longer than 850 nm doesn't provide sufficient energy to excite the PS to its triplet state and beyond these wavelengths (> 1300 nm) light absorption by water molecules dominates. Hence, the spectral range between 600 nm to 850 nm is referred as 'phototherapeutic window' [49, 74]. However, it has also been demonstrated in several studies that tumor damage actually occurs to a greater depth, upto 2.0 cm, than the optical penetration depth of light [76-79].

2) ***Hypoxia***: It is a generally accepted that $^1\text{O}_2$ generated via type II photochemical mechanism plays a key role in the PDT induced tumor damage. Therefore, due to the fact that the majority of the PSs act via this mechanism, their PDT efficacy depends heavily on the availability of O_2 in the tissue environment [49, 61, 80-83]. In solid tumors, the cells often experience hypoxic conditions due to poor vascularization and this is one of the reasons for the therapeutic failure of PDT [49, 84-86]. Thus, to improve the efficacy of PDT there is a need to explore the possibilities of modifying the photophysical properties of the PS such that its photodynamic activity should not depend solely on $^1\text{O}_2$ but it can also act via Type I mechanism, so that the PS in

excited state (singlet and/or triplet) can directly interact with surrounding biomolecules, and thus is less dependent on O₂ [49, 80-83].

1.4. Insertion of high Z elements: A promising approach to overcome the limitations of PDT

The presence of heavy elements in PS strongly influences its electronic and photophysical properties and hence conjugation of PS with a suitable element is regarded as a potential strategy to improve its photodynamic properties. Moreover, PSs conjugated to metal ion or metal complex and heavier halogen have attracted considerable attention as promising agents for multimodal cancer therapy and tumor imaging. These tetrapyrrole compounds depending on the type and nature of inorganic element have been explored for PDT, chemotherapy, X-ray PAT, radiotherapy and also for tumor imaging using Magnetic resonance imaging (MRI), X-ray contrast or Positron emission tomography (PET) [87-92]. Particularly, the combination of metal-based PS and X-ray irradiation has been investigated as a promising novel approach to treat deep-seated tumors, which in case of PDT is a major limitation due to low penetration of light in tissue [93-96]. The following sections provide a review on the present status of the knowledge on the effect of insertion of metal or halogen on the photophysical properties of PS, various metal and halogenated PSs investigated for PDT, chemotherapy and PAT.

1.4.1. Effect of metal and heavy elements on photophysical properties of PS

The lifetime and quantum yield of ³PS* correlate with its ability to produce adequate levels of ROS, hence these are important requirements of PSs [97]. Due to heavy atom

effect, the attachment of heavy element to PS exerts significant effect on its excited states and therefore influences its photosensitization efficiency. Generally, the attachment of a heavy atom, such as a halogen or transition metal to the tetrapyrrolic structure promote the transition of $^1\text{PS}^*$ to a $^3\text{PS}^*$ by spin-orbit perturbation/coupling and thus improves the yield of ROS generation [97, 98]. The majority of metal complex of tetrapyrrole compounds reported so far contain metal ion in the center of the macrocyclic ring. This is due to the fact that the macrocyclic ring with four nitrogen atoms at its central cavity acts as a tetradentate ligand for various metal ions.

Studies have shown that the photosensitization property of the PS is also influenced by the nature of the central metal ion bound to macrocyclic ring. In general, diamagnetic metals such as Zn^{+2} , Pd^{+2} , In^{+2} , Lu^{+3} , Sn^{+4} improve the triplet state quantum yield whereas, paramagnetic ions (i.e., Mn^{+3} , Cu^{+2} , Co^{+2} , Fe^{+3} , Ni^{+2}) conjugated with tetrapyrroles deactivates the $^3\text{PS}^*$ and thus, reduce the $^3\text{PS}^*$ lifetime. Insertion of Zn in tetraphenylporphyrin (TPP) was shown to increase the $^3\text{PS}^*$ quantum yields (Φ_T) from 0.73 to 0.86, without any effect on triplet lifetime (τ_T) ($>10 \mu\text{s}$), whereas insertion of Pd led to an increase in both Φ_T and τ_T ($>50 \mu\text{s}$). For Ce6, insertion of Sn leads to increase in τ_T ($240 \mu\text{s}$) as compared to free Ce6 ($50 \mu\text{s}$), while for copper complexes of TPP, TPPS and Ce4 τ_T is negligible [64, 66, 99, 100]. Chlorophyll inserted with Mg^{2+} , Zn^{2+} and Cu^{2+} have τ_T of 209 ns, 199 ns and 67 ns respectively as compared to metal-free pheophytin a (τ_T 154 ns) [101]. Zn complex of picolylamine porphyrin exhibited Φ_T of ~ 0.97 , as compared to the free base porphyrin derivative (0.64) [102].

Thus, as compared to freebase counterpart, diamagnetic and heavy metal complexes of porphyrins, chlorins and bacteriochlorins have been shown to give better

PDT efficacy, due to higher efficiency to generate ROS, whereas the paramagnetic metal complexes are usually photodynamically inactive. A systemic study carried out by Ando et al., showed that 2,4-bis(1-decyloxyethyl)-deuteroporphyrinyl-6,7-bisaspatic acid and its Zn, Ga, In and Sn complexes with longer (> 1 ms) τ_T exhibited significant photocytotoxicity, while its metal complex of Mn, Cu, Ni and Fe, with short (< 0.01 ms) τ_T , showed no photocytotoxicity, indicating that the τ_T of these derivatives played a significant role in their photocytotoxicity [103]. Similarly, Pd(II) and Pt(II) complex of chlorins showed strong phototoxicity in cancer cells in comparison to its free base chlorin [104]. Zn(II), In(III), and Ni(II) complexes of Methyl pyropheophorbide-a were synthesized and among these analogues the In(III) complex showed the best PDT efficacy while the Ni(II) complexes, because of its inability to produce ROS, did not show any PDT efficacy [105]. *In vitro* cytotoxicity study with TPPS4 (meso-tetrakis(4-sulfonatophenyl) porphyrin) and its metal complexes with Zn, Pd and Mg, showed ZnTPPS4 to be the most effective PS, due to its capability to generate more ROS as compared to other PSs [106]. Phototoxicity induced by non-metalated bacteriochlorophyll and its Pd complex was almost the same, whereas the complexes with Cu, Zn and Mn were photodynamically inactive (the Zn complex was found inoperative due to its oxidation into chlorin during incubation) [107]. Iron (III) complex of meso-tetrakis (carboxyl) porphyrin meso-tetrakis (carboxyl) porphyrin, did not lead to any phototoxicity against cancer cells [108]. Ni, Cu and Zn complex of ^{131}I labeled methyl 3-devinyl-3-{1'-(benzyloxy)-ethyl}pheophorbide-a complex were investigated for phototoxicity against cancer cell lines. These studies showed that Zn complex was most effective PS, which induced significant phototoxicity at a concentration of $1.5 \mu\text{M}$ at a light dose of 20 J/cm^2 ,

while a concentration of 50 μM and light dose of 30 J/cm^2 was required for Ni and Cu complex to induce $\sim 50\%$ cell death [109-111].

However, there are few exceptions to this general conception. For example, studies in leukemia cells and a rat bladder tumor model have demonstrated that copper octaethylbenzochlorin is an efficient PS despite its nearly undetectable triplet state [59]. The PDT activity of copper octaethylbenzochlorin was attributed to interactions between the cationic iminium group and biomolecules which allow electron-transfer reactions to take place via the short-lived excited singlet state and lead to the formation of radicals and radical ions [59]. Studies on Mn complex of meso-tetrakis (carboxyl) porphyrin, showed significant phototoxicity similar to free base porphyrin. [108]. Further, Co(II) and Cu(II) methyl pheophorbide-a also lead to significant phototoxicity in A549 cells [112].

The presence of halogen atom in PS increases intersystem crossing (ISC) through heavy atom effect and thus can increase the Φ_T or τ_T . For example, as compared to ZnTPP (Φ_T of 0.86) its fluorinated and chlorinated derivative show higher Φ_T of 0.99 and 1.02, respectively [113]. Comparison among complexes of 5,10,15,20-tetrakis(4-carbomethoxyphenyl)porphyrin Φ_T was highest for iodinated complex (0.88), followed by brominated complex (0.75) and lowest for nonhalogenated PS (0.35) [114]. These results showed that halogenation could increase Φ_T or τ_T of PS and thus its efficiency to generate $^1\text{O}_2$ can be enhanced significantly. However, the magnitude of the effect has been shown to depend on the type of halogen present in the PS. For example, Topkaya et al, have shown that among the four halogen atoms (F, Cl, Br, I) used for halogenation of trihydroxylated mono-halogenated porphyrin, the $^1\text{O}_2$ quantum yield (Φ_Δ) was enhanced

predominantly by iodination ($\sim 98\%$) [115]. Studies with non-tetrapyrrolic compounds such as BODIPY dye showed that the Φ_{Δ} values of halogen substituted was in the order of $H < Cl < Br < I$, consistent with the Heavy Atom Effect of these halogens [116]. Similarly, non-halogenated squaraine dyes which are poor generators of 1O_2 , upon bromination and iodination showed a significant increase in Φ_{Δ} [117]. A similar increase in Φ_{Δ} through halogenation has also been reported for Rose Bengal [50].

Another important effect of the insertion of metals in porphyrins, chlorins and bacteriochlorins is change in absorption and fluorescence properties. In case of porphyrins, the typical change in absorption property due to the insertion of metal is hypsochromic (blue) shift in the position of the long-wavelength absorption band. For example, the Q band of TPP shifts from 650 nm to 588 nm, 553 nm and 600 nm for ZnTPP, PdTPP and InTPP respectively. Further, the metallation of porphyrins also results in collapse of two out of four Q bands in the spectrum. The later effect was attributed to the increase in the symmetry (e.g., D_{2h} to D_{4h}) of the tetrapyrrole ring [100]. For chlorins, insertion of a metal also causes a similar hypsochromic shift of the long-wavelength Q absorption band without causing any alteration in the symmetry. For chlorophyll derivatives, chlorin *e*₆ and Pheophorbide-a, insertion of Sn²⁺, Pd²⁺, Cu²⁺ cause ~ 15 nm blue shift in Q band whereas in case of Zn²⁺ the blue shift was only few nm [66, 100, 112]. Ruthenium (II) ions inserted in porphyrin core have Q absorption bands in the wavelength region between 500-550 nm [118]. While (TPP) arene-ruthenium(II) derivatives where arene-ruthenium are inserted as peripheral macrocycle substituents showed no change in Q band position as compared to TPP Q band at 642 nm [119]. There are some exceptions where insertion of some metal ions

causes red-shift in the long-wavelength absorption band. For example, insertion of the tin atom in the central cavity of etiopurpurin, a chlorin PS, causes a red-shift of approximately 20–30 nm with respect to non-metallated etiopurpurin [64]. Tin (IV) benzochlorin was reported to exhibit an increased photodynamic effect in transplanted urothelial cell carcinoma in rats, as compared to sulphonated benzochlorin [120].

Similarly, the insertion of a metal ion in PSs also influences its fluorescence quantum yield (Φ_F) and lifetime (τ_F). A general pattern of decrease in fluorescence of tetrapyrrolic compounds is observed for complexes of closed-shell metal where complexes of first- and second-row elements (e.g., Mg, Al) show longest τ_F and higher Φ_F than the third-row (e.g., Zn) and fourth-row elements (e.g., Cd, In). Complexes with open-shell central metals such as diamagnetic Pd and paramagnetic Co, Ni, Cu, Fe have no detectable fluorescence. Φ_F of TPP, ZnTPP, InTPP, PdTPP and CuTPP is 0.10, 0.033, 0.05, 0.0002 and 0 respectively. Similarly, Φ_F for TPPS, ZnTPPS, PdTPPS and CuTPPS is 0.08, 0.043, $< 10^{-4}$ and 0 respectively. For Ce6, ZnCe6 and CuCe4, Φ_F of 0.13, 0.14, 0.09 respectively has been reported [66, 100]. The Zn bacteriochlorins exhibit Φ_F of 0.13 that is comparable with non-metallated bacteriochlorins (0.15). The Φ_F values for In chelates is reduced to 0.02 and it is further reduced in Pd bacteriochlorins (Φ_F of 0.006) and for Cu- bacteriochlorins no fluorescence was observed [121]. The decrease in fluorescence yield is because of the enhancement of internal conversion to the ground state. Paramagnetic complexes have one odd electron that can couple to the spin of the tetrapyrrole triplet yielding a “tripdoublet” and a “tripquartet” state. Similarly, that odd electron can couple its spin with that of the PS first excited singlet state, leading to singmultiplet states. Moreover, the singmultiplet states couple efficiently with the tripmultiplet states resulting in

manifold increase in intersystem crossing from the excited singlet state to the triplet. This coupling mechanism deactivates the singlet states rapidly and quenches almost completely the fluorescence of paramagnetic complexes of tetrapyrroles, while Pd has tightly bound d orbitals that push the intermediate states closer in energy to the ground state, disfavoring the radiationless path [113].

1.4.2. Metal conjugated tetrapyrroles as chemotoxic and phototoxic agent

Tetrapyrrole compounds conjugated with both metal complexes and metal ions have been investigated as a promising strategy for selective delivery of toxic metal ions or metallodrug fragment to tumor cells and exploit the advantage of both chemotoxic and phototoxic effects. Sulfonated pyridinetriphenylporphyrin and hematoporphyrin conjugated to cisplatin and carboplatin were shown to exhibit a synergistic antiproliferative effect against various cell lines through both cytotoxic and phototoxic effect, when compared to the metal complex and PS alone or a combination of the drugs [122-126]. Certain Pt(II) complexes of hematoporphyrin derivatives exhibited elevated tumor localizing effect (tumor/muscle ratio >2) as compared to carboplatin in tumor-bearing mice [125,126]. Momekov et al, reported synthesis of three different types of platinum complexes of hematoporphyrin IX – (1) The “sitting atop” complex, where the Pt(III) is coordinated to two adjacent porphyrin pyrrole nitrogens, (2) The metalloporphyrin-type complex with Pt(III) coordinated through four pyrrole-nitrogens of Hp and (3) The peripheral complex in which Pt(III) is coordinated to the carboxylic groups of propionic acid side chains of Hp. These complexes showed cytotoxic (without light) effects against various cancer cell lines by targeting DNA. Among these three complexes, complexes in which Pt (III) was

coordinated at the center of the macrocyclic ring was found to be more effective than the 3rd complex [127]. Tetraplatinated porphyrins with peripheral platinum centers showed photo and cytotoxicity against human cervical (HeLa), ovarian (A2780) and cisplatin-resistant CP70 carcinoma cell lines. Nuclear localization of these complexes and interaction with CT-DNA mainly through intercalation suggested DNA as the main target for inducing cytotoxicity [128].

Apart from platinum-based PSs, complexes of tetrapyrrolic compounds with other metals such as gold (Au) and ruthenium (Ru) have also been reported. Au (III) complexes of tetraphenyl porphyrin showed *in vitro* and *in vivo* anti-cancer chemotoxicity but lacked photosensitizing efficacy [129-131]. Studies suggested that this complex induced apoptosis through both caspase-dependent and caspase-independent mitochondrial pathways by targeting mitochondrial membrane potential [132]. Similarly, Au(II) complex of Hp showed chemotoxic potential against a wide spectrum of leukemia- and lymphoma-derived tumor cell lines by inducing DNA fragmentation. Moreover, Au(II) Hp showed less cytotoxicity against non-cancerous human kidney cell line 293T in comparison to cisplatin, which exerted prominent cytotoxic effects similar to that induced in the cancer cell lines [133]. Porphyrin complexes of Ru containing metal ion coordinated to nitrogen atoms and a polypyridyl Ru(II) complex conjugated to macrocycle as peripheral substituents have been reported [118]. While polypyridyl Ru(II) porphyrin conjugate showed both chemotoxicity and phototoxicity, the complexes having Ru coordinated with nitrogen atoms failed to show any anticancer activity [134, 135]. Similarly, extended-arms Ru-porphyrins also showed both chemotoxic and phototoxic anticancer effect in human breast cancer cells MDA-MB-231. Further, the study showed that the cytotoxic effect

of these complexes was significantly less in nontumorigenic epithelial cells HBL- 100 as compared to MDA-MB-231 cancer cells [135]. Ru-porphyrin conjugates bearing four peripheral Ru(II) half-sandwich coordination compounds, and another centrally inserted Ru(II) porphyrin induced both phototoxic and cytotoxic effect in cancer cells [118,119].

Besides these Ru, Pt and Au tetrapyrrole complexes, a Cu (II) complex of (5,10,15-tripyridyl-4-yl-porphyrin- 5-yl)benzonitrile has also been reported to exert dark as well as light induced cytotoxicity against the human breast cancer cell line (MCF7) and the dark toxicity of this compound was shown to be mediated through ROS generation [136]. Few Ag complex porphyrins such as 5,10,15,20-tetra(4-N-allylpyridyl)porphine tetrabromide and 5-Mono (3'-methoxy-4'-hexadecyloxyphenyl) -10,15,20-tri(4'-Nallylpyridyl) porphine tribromide have also shown promising chemotherapeutic activity against cancer cells [137,138]. Also, Pd(III) complexes of Hp exhibited dark cytotoxicity against a panel of cancer cells by inducing DNA-fragmentation [139].

1.4.3. PSs for combined radiotherapy and PDT using X-ray irradiation

To overcome the limitation of PDT to treat deep-seated tumor, Chen and Zhang in 2006, proposed a new approach that exploits the tissue penetration property of X-ray radiation for photoactivation of PS. This approach makes use of PS conjugated to lanthanide or metal nanoparticles which upon exposure to X-rays emit visible light by scintillation and thus activates the PS [140-142]. The efficacy of this approach depends on several factors such as effective energy transfer between PS and

scintillating material, cellular uptake of the conjugate, and most importantly on Φ_{Δ} which in deeper tumor region will be limited by hypoxic conditions [49, 85, 141].

Alternatively, the combination of PS and X-ray irradiation has also been proposed for PAT which in principle involves direct interaction of a metal present in drug with X-rays and subsequent generation of Auger electrons and free radicals through photoelectric effect (section 1.3.1). Since free radical generation via Auger electrons is less dependent on O_2 , the efficacy of PAT is less likely to be affected by hypoxia which generally prevails in solid tumors. The sensitization effect of metal complex results in higher dose deposition in tumor tissue and since a relatively low dose of radiation is required, damage to the normal tissue can be reduced significantly. Due to this advantage, PAT is actively being investigated for the treatment of high-grade brain tumors with promising outcome. For example, studies in glioma-bearing rats and mice showed that administration of iodine or platinum compounds and its activation with X-ray result in higher survival compared to radiation alone [42, 44-47]. However, the use of cisplatin is associated with severe side effects which warrant development of less toxic and more effective agents to fully exploit the advantages of this therapeutic approach [143]. PS conjugated to high Z metal are promising alternative candidate for PAT but except few agents such as Au complex of chlorin e6 [144] and Iodinated pyropheophorbide derivative [145] the efficacy of PS for X-ray photon-activation treatment of cancer is not well investigated.

Mono-L-aspartyl aurochlorin e_6 (Au-NP e_6) was investigated for diagnosis and treatment of tumor by Synchrotron X-ray radiation. Tumor-bearing mice treated with Au-NP e_6 , showed good absorption contrast on X-ray films. Moreover, X-ray irradiation of Au-NP e_6 pretreated mice with 25 keV Synchrotron radiation showed a

slow rate of tumor growth as compares to control mice [144]. Studies carried out by Pandey et al. reported that Iodinated HPPH (I-HPPH) can act as a selective radiosensitizer for tumor with X-ray energy of 33 keV (the K-edge absorption energy of Iodine). I-HPPH showed significant *in vitro* radiosensitization effect in T24, a human bladder cancer cell line. The radiosensitization effect was caused by a significant increase in ROS generation following X-ray irradiation of cells pre-treated with I-HPPH. It was suggested to be mitochondria-mediated radiosensitized cell death, due to the localization of I-HPPH in mitochondria. Furthermore, X-ray irradiation of I-HPPH pretreated tumor-bearing mice showed a delayed growth rate of tumor as compared to mice treated with X-ray alone [145].

1.5. Aim of the study

Chlorin derivatives obtained from natural plant pigment chlorophyll are promising candidates for PDT because they possess ideal photophysical properties such as good absorption coefficient in the wavelength region of therapeutic interest and higher yield of $^3\text{PS}^*$. One such derivative, Chlorin p_6 (Cp_6) was explored by A Dube and coworkers as potential PS for PDT of cancer. Cp_6 demonstrated high photodynamic activity against various cancer cell lines [146, 147]. In hamster cheek pouch model, Cp_6 showed preferential accumulation in tumors, rapid clearance from the skin and complete tumor regression after PDT [148, 149]. The aim of this Ph.D. work was to investigate the use of copper iodide (CuI) conjugated Cp_6 as a multimodal anticancer agent by exploring its photodynamic, X-ray photon-activation and chemotoxic activity against cancer cells. CuI was selected to prepare complex with Cp_6 because of several considerations. Insertion of high Z element in PS molecule can enhance the yield of its

triplet state through heavy atom effect and thereby improve its efficiency to generate ROS. Several copper complexes are potential agents for chemo and radiotherapy of cancer [150, 151]. The mode of chemotoxic action of copper complexes involves redox-mediated elevation ROS and/or inhibition of ubiquitin-proteasome activity [150, 152]. Thus, copper complexes due to a different mode of action than the platinum-based drugs hold considerable promise for the treatment of platinum-resistant cancer cells. Particularly, the property of the copper complex to increase intracellular ROS levels through redox process is considered useful because it can exploit the metabolic differences of normal and cancer cells to achieve tumor selective chemotoxicity [153, 154]. Further, the X-ray absorption property of copper & iodide can be exploited for photon-activation therapy (PAT). Importantly, both copper and iodine are considered to be relatively well tolerated metabolically because these are required as essential trace elements [155].

The main objectives of this study are as follows:

1. Preparation of the Cp_6 -CuI conjugate and characterization of its chemical structure, photodynamic activity and interaction with human serum albumin and DNA.
2. Evaluation of PDT efficacy of Cp_6 -CuI in cancer cells.
3. Evaluation of the cytotoxic potential of Cp_6 -CuI combined with X-ray photoactivation.
4. Evaluation of the chemotoxic efficacy of Cp_6 -CuI in cancer cells.

Chapter 2

Materials and Methods

2.1. Materials

2.1.1. Fluorescence probes

Singlet oxygen sensor green (SOSG), 3'-(p-Aminophenyl) fluorescein (APF) and Alexa Fluor 488 labeled rabbit anti-mouse antibody were obtained from Invitrogen (USA). 2', 7'- Dichlorodihydrofluorescein diacetate (DCFH-DA), Hoechst 33342 (HO), Propidium iodide (PI), Ethidium bromide (EB) and Acridine orange (AO) were purchased from Sigma (USA). Cell organelle probes Mitotracker green, LysoTracker blue, ER-Tracker green, Golgi tracker green and Alexa Fluor 488 phalloidin were obtained from Thermo Fischer Scientific (USA).

2.1.2. Biochemicals & Culture media

Human serum albumin (HSA), Bovine serum albumin (BSA), agarose and Trolox were purchased from Sigma (USA). Dulbecco's Modified Eagle's Medium (DMEM), Dulbecco's Modified Eagle Medium / Nutrient Mixture F-12 Ham (DMEM / F12, 1:1 Mixture), Phosphate buffered saline (PBS), Tetrazolium salt 3-(4,5-dimethylthiazol-2-yl)-2,5-diphenyltetrazolium bromide (MTT), 0.25 % Trypsin/EDTA solution, Fetal bovine serum (FBS) and Xylenol orange (XO) were obtained from Himedia, India. Calf thymus DNA (CT-DNA) and plasmid DNA (pUC19) were obtained from Genei (MERCK). Mouse anti-human γ -H2AX antibody was obtained from Millipore (USA). Bicinchoninic Acid (BCA) and reduced glutathione (GSH) was purchased from Alfa Aesar (USA). Millipore water was used throughout for the preparation of all solutions. All other solvents and reagents used were of analytical grade.

2.1.3. Cell lines

Human oral cancer cell lines NT8e derived from upper aerodigestive tract (pyriform fossa) and 4451 derived from a recurrent tumor in the lower jaw were obtained from Advanced Centre for Treatment, Research and Education in Cancer (ACTREC), Mumbai and Institute of Nuclear Medicines and Allied Sciences (INMAS), Delhi respectively. HaCaT, a non-cancerous immortalized dermal keratinocyte cell line was obtained from National Centre For Cell Science (NCCS), Pune, India.

2.1.4. Preparation of Cp_6 -CuI conjugate

Cp_6 was prepared from Chlorophyll-a isolated from dried spirulina powder following the procedure described by Hooper et al [156]. Cp_6 -CuI conjugate was synthesized by mixing equimolar concentration of Cp_6 and CuI in methanol: acetonitrile (1:10 v/v) at room temperature. The solvent was partially evaporated to result in precipitation of the complex. The precipitates were collected by centrifugation (6000 g, 10 min). The product was further purified by Silica column chromatography using methanol: acetonitrile solvent system. The chemical structure of Cp_6 -CuI conjugate was determined by X-ray Fluorescence spectroscopy (XRF), Fourier Transform Infrared spectroscopy (FTIR), Electron Paramagnetic Resonance spectroscopy (EPR) and High-resolution Mass Spectroscopy (HRMS) analysis (described in chapter 3). From the proposed structure it is henceforth referred as “Iodinated Chlorin p_6 -Copper complex” (IC p_6 -Cu).

Stock solution of IC p_6 -Cu: For *in vitro* experiments, the stock solution of IC p_6 -Cu conjugate was prepared in ethanol: PEG (400): phosphate buffer (20:30:50) and stored

at -20 °C, in dark till use. For cell-free studies on photodynamic activity in aqueous solution and binding interaction of the conjugate with HSA and DNA, the stock solution was prepared in 25 mM phosphate buffer (pH 7.4).

2.2. Methods

2.2.1 Cell culture

Oral cancer cell lines (4451 and NT8e) and HaCaT cell lines were maintained in DMEM and DMEM / F12, 1:1 Mixture, respectively. The growth media contained antibiotics (streptomycin, nystatin, penicillin) and 10 % FBS. For subculture, the cells were released by trypsinization and approx 0.4×10^6 cells were added to 5 ml growth media in cell T-25 culture flask (25 cm²) and incubated at 37 °C under 5 % CO₂ + 95 % air atmosphere in a humidified incubator (ESCO, USA). The cells grown to confluency (70- 80 %) were harvested by trypsinization and after counting, cells were seeded in either petri dishes (35 mm) or multiwell plates as per experimental requirement. The cells were allowed to attach and grow for 18 h till they reached exponential phase and then used for various experiments.

2.2.2 Treatment of cells with ICp₆-Cu

The cells were grown in either petri dishes (35 mm) or multiwell (96 or 24) plates as described above. For ICp₆-Cu treatment, the growth media from cell monolayer was removed and replaced with fresh media containing a specified concentration of ICp₆-Cu. The cells were incubated at 37 °C in a humidified CO₂ incubator, in dark for specified time duration as mentioned in various studies. For control, the cells were incubated in growth medium without ICp₆-Cu. After incubation, the growth medium

was aspirated and the cell monolayer was washed twice using plain medium (without serum). Subsequently, the cells were used in various assays or subjected to further treatments as mentioned specifically in various studies.

2.2.3. Light Irradiation

For studies on photodynamic activity of ICp_6-Cu , the samples were irradiated with red light (630 ± 20 nm) from a LED lamp (Dia 4 cm) fitted with a diffuser glass plate for homogenous illumination. The samples were kept at a distance of ~ 6.0 cm below the LED lamp. In studies where parent Cp_6 was used for comparison, the samples were irradiated with red light (660 ± 5 nm) using a diode laser source (Thorlabs, USA). The laser beam was expanded and collimated using appropriate lenses. The power at sample level was measured using a power meter model AN/2 (Ophir) and the power density was kept nearly same (~ 3.5 mW/cm²) for both the light source.

2.2.4. MTT assay

The cytotoxic effect of photodynamic treatment, photon-activation treatment and ICp_6-Cu alone on different cell lines was assessed by MTT assay [157, 158]. In this assay, MTT is converted into dark blue formazan through enzymatic action of mitochondrial succinate dehydrogenase in live cells. The optical density of the color produced gives the relative estimate of viable cells with respect to untreated control. The procedure followed for MTT assay was as follows. The cells grown in 96 well plate were subjected to various treatments and at the specified time period mentioned in specific studies, the growth medium from the cells was removed and fresh medium (without serum) containing MTT (0.5 mg/ml) was added. After incubation at 37 °C

for 3 h in dark, the medium was removed and 100 μ l of dimethyl sulfoxide (DMSO) was added to dissolve the formazan crystals formed within the cells. The absorbance of the samples at 570 nm with the reference wavelength at 690 nm was measured using Powerwave340 microplate reader (Bio-Tek instruments Inc., USA). The absorbance value was used to calculate percent cell viability with respect to the value of control samples.

2.2.5. Determination of intracellular ROS levels

The amount of ROS generated in cells was measured by fluorescence spectroscopy using fluorescence probe DCFH-DA [159, 160]. The non-fluorescent DCFH-DA freely diffuses in cells and converted into a non-fluorescent product 2',7'-dichlorodihydrofluorescein (DCFH) by the enzymatic action of cellular esterases. In cells, DCFH reacts with the broad range of ROS ($O_2^{\cdot-}$, $\cdot OH$, H_2O_2 and 1O_2) and oxidized into highly fluorescent product dichlorofluorescein (DCF) [160]. Briefly, the procedure was as followed. The cells subjected to various treatment and after the specified time periods mentioned in specific studies, cells were washed twice with ice-cold PBS and incubated in culture media (without serum) containing DCFH-DA (10 μ M) for 30 mins at 37 $^{\circ}C$. Cells were released by trypsinization, re-suspended in PBS and the fluorescence of DCF in cells was measured on fluorimeter using λ_{ext} at 488 nm and λ_{em} at 525 nm. All the procedures were done in diffused room light. The fluorescence intensity of the cell suspension after normalization with cell number was used to express the relative ROS level in control and treated cells.

2.3. Methods used for characterization of ICp₆-Cu

2.3.1. Spectroscopic characterization of Cp₆-CuI conjugate

The UV/Vis absorption spectra of the Cp₆ and Cp₆-CuI were recorded from 350-750 nm, at 1 nm bandpass on a Cintra-20 spectrophotometer (GBC, Australia). The fluorescence emission spectra of Cp₆ and ICp₆-Cu were recorded on a Fluorolog-2 spectrofluorometer (Spex, USA) by setting excitation wavelength at ~400 nm, scan range from 500-700 nm and band-pass of ~1.7 nm and ~3.7 nm for excitation and emission slits, respectively. The X-ray fluorescence of Cp₆-CuI was recorded on microprobe XRF beamline (BL-16) at Indus-2 synchrotron radiation facility, RRCAT [161]. For preparation of the sample for XRF, 10.0 μl concentrated solution of Cp₆-CuI in methanol was applied on a piece of Silicon wafer and air dried. Monochromatic X-ray of energy 12.0 keV (beam size 4 mm X 4 mm) was used to excite the fluorescence from the sample. XRF spectra were recorded using a Vortex energy-dispersive detector (SII NanoTechnology, USA). FTIR spectra were recorded on a spectrometer model (FTLA 2000 MB 104) using powdered sample deposited on Zinc Selenide window. The X band EPR spectrum of Cp₆-CuI was recorded on Spectrometer model JES (Jeol, Japan) at 100 K. Methanol was used as solvent. Mass spectrum of Cp₆-CuI was recorded in positive electrospray ionization mode on Bruker microTOF QII high-resolution mass spectrometer at IISER Bhopal, India.

2.3.2. Fluorescence assay for determination of generation of $^1\text{O}_2$ and other ROS in solution

Photosensitized generation of $^1\text{O}_2$ and other ROS for $\text{ICp}_6\text{-Cu}$ and Cp_6 was monitored by fluorescence spectroscopy using three different fluorescence probes: SOSG, APF and DCFH-DA. SOSG reacts specifically with $^1\text{O}_2$ to result in the formation of highly fluorescent endoperoxide product [162]. While, DCFH-DA is non-specific fluorescence probe for detection of the broad range of ROS including $^1\text{O}_2$ as well as other ROS ($\text{O}_2^{\cdot-}$ and $\cdot\text{OH}$, H_2O_2). For detection of ROS in cell-free system, DCFH-DA is chemically converted into dihydro-dichlorofluorescein (DCFH) by hydrolysis according to the protocol described by Bourré et al [163]. For this, DCFH-DA was mixed with 0.01 N NaOH in absolute ethanol and the solution was kept at room temperature for 30 min to allow hydrolysis. After neutralization with 25 mM sodium phosphate buffer (pH 7.4), the solution was stored on ice in dark until use. DCFH upon reaction with various ROS is oxidized into green fluorescent dichlorofluorescein (DCF). To distinguish the relative level of $^1\text{O}_2$ and other ROS generated via Type II and Type I photochemical mode respectively, fluorescence probe APF in presence of NaN_3 and D_2O were used. APF detects both $^1\text{O}_2$ and $\cdot\text{OH}$ radicals [164]. APF upon reaction with $\cdot\text{OH}$ and $^1\text{O}_2$ is converted to a fluorescent product due to the cleavage of the aminophenyl ring from fluorescein ring system. The relative contribution of $^1\text{O}_2$ was confirmed by use of NaN_3 , a specific quencher and also by replacing H_2O with D_2O , in which the lifetime of $^1\text{O}_2$ is ~ 10 times enhanced.

For monitoring generation of $^1\text{O}_2$ and other ROS, $\text{ICp}_6\text{-Cu}$ or Cp_6 (5 μM) was added to 3.5 ml sodium phosphate buffer (pH 7.4) in a plastic petri dish (3.5 cm dia). After addition of the fluorescence probe, the solution was irradiated with appropriate

wavelengths of light using light sources described in section 2.2.3, in dark. The solution was continuously stirred during irradiation. At different time interval, 200 μ l aliquot was withdrawn and fluorescence was measured on spectrofluorometer. SOSG, DCF and APF were excited at 485 nm, 488 nm and 490 nm, respectively. The emission was recorded from 510 nm to 600 nm and the peak fluorescence intensity of SOSG, DCF and APF at 530 nm, 525 nm and 515 nm respectively was used to determine changes in relative ROS levels by plotting ratio of fluorescence intensity before irradiation (F_0) and at different time interval after irradiation (F_t) as F_t/F_0 vs irradiation time.

2.3.3. Photobleaching

Photobleaching of ICp_6 -Cu and Cp_6 were studied by absorption spectroscopy. A 2.5 ml solution of 5 μ M ICp_6 -Cu or Cp_6 in air saturated sodium phosphate buffer (pH 7.4) was taken in a 1 \times 1 cm quartz cuvette without lid and irradiated with appropriate wavelengths of light using light sources described in section 2.2.3. The solution in the cuvette was continuously stirred during irradiation. The absorbance of the two chlorins at Soret band before irradiation (A_0) and at different time interval after irradiation (A) was measured. The change in absorbance plotted as A/A_0 vs irradiation time was used to express relative photobleaching.

2.3.4. Octanol/ water partition coefficient

Partition coefficients of Cp_6 and ICp_6 -Cu were determined in 1-octanol–sodium phosphate buffer (pH 7.4) system. A saturated solution of octanol and buffer was prepared by vigorous shaking of buffer and octanol mixture for 4 h at room

temperature. 10 μM of Cp_6 and $ICp_6\text{-Cu}$ was dissolved in pre-saturated buffer phase, to which an equal volume of presaturated octanol phase was added. The mixture was mixed for 1 h by intermittent vortexing, centrifuged at 5000 rpm for 5 min and left at room temperature for ~ 1 h to allow the two phases to separate. The concentration of Cp_6 and $ICp_6\text{-Cu}$ in both the phases was determined by absorption spectroscopy. The partition coefficients (P) were calculated as:

$$\text{Log}P_{\left(\frac{\text{Oct}}{\text{Buffer}}\right)} = \text{Log} \left[\frac{C_{\text{Oct}}}{C_{\text{Buffer}}} \right] \quad (1)$$

Where, C_{Oct} and C_{Buffer} are the concentration of PS in the organic and the buffer phase, respectively.

2.3.5. Binding studies of $ICp_6\text{-Cu}$ with HSA

2.3.5.1. Spectroscopic measurements

The absorption spectra and fluorescence spectra of $ICp_6\text{-Cu}$ (5 μM) in the absence and presence of varying concentration of HSA (0-10 μM) were recorded from 350 nm to 750 nm and 600 nm -700 nm ($\lambda_{\text{ex}} = 400$), respectively. To assess albumin binding affinity, the intrinsic fluorescence of HSA due to tryptophan (Trp) and tyrosine (Tyr) was excited with 280 nm light and emission was recorded from 300-500 nm. The fluorescence intensity of HSA in presence of $ICp_6\text{-Cu}$ was corrected for inner filter effect using the following equation [165]:

$$F_{\text{cor}} = F_{\text{obs}} \times e^{\frac{A_{\text{ex}} + A_{\text{em}}}{2}} \quad (2)$$

Where, F_{cor} and F_{obs} are the corrected and observed fluorescence intensities respectively. A_{ex} and A_{em} are the absorptions of the ICp₆-Cu at the excitation and the emission wavelength, respectively. To determine the change in protein conformation, the synchronous fluorescence spectra of HSA from 220-400 nm with a difference between excitation and emission wavelength ($\Delta\lambda$) of 15 nm and 60 nm were recorded to resolve the intrinsic fluorescence of Tyr and Trp residues, respectively. For fluorescence measurements, the concentration of HSA was fixed at 5 μM while the concentration of ICp₆-Cu was varied from 1 μM to 10 μM .

The fluorescence emission spectra of ICp₆-Cu excited with 280 nm for Forster non-radiative energy transfer (FRET) was recorded on a FLS920-s spectrometer (Edinburgh Instruments Ltd., UK). The excitation and emission bandpass was adjusted at 2 nm and 3 nm, respectively. To eliminate the higher order excitation, a 330 nm short wavelength cut-off filter was placed before the emission monochromator.

2.3.5.2. Fluorescence lifetime measurements

The experiment set up used to determine the fluorescence lifetime of ICp₆-Cu and Cp₆ consisted of a time-correlated single photon counting (TCSPC) system 'Lifespec-Red' (Edinburgh Instruments, UK) equipped with a Hamamatsu MCP-PMT. The system has an instrument response function (IRF) of ~ 40 ps. The chlorins were excited by vertically polarized light at 400 nm using a Coherent Mira 900F femtosecond laser system, the output of which was pulse picked (Coherent 9200 pulse picker) at a rate of 3.8 MHz and then frequency doubled in an ultrafast harmonic generation system (Inrad 5-050). The excitation light was eliminated by using an appropriate filter and emission was detected at a magic angle over the entire band. The fluorescence traces

after deconvolution by the iterative reconvolution method were fitted to a single- or multiexponential function using FAST software of the TCSPC system.

2.3.6. Binding studies of IC_{p6}-Cu with DNA

2.3.6.1. Spectroscopic measurements

The binding affinity of IC_{p6}-Cu conjugate with DNA was determined by absorption spectroscopy. The absorption spectra of IC_{p6}-Cu without and with increasing concentration of CT-DNA was recorded from 350-750 nm on a spectrophotometer in double beam mode, against a reference sample, which contained CT-DNA in phosphate buffer (pH 7.4) at the same concentration as that in the sample. The concentration of CT-DNA was adjusted using its molar extinction coefficient (ϵ) value ($6600 \text{ M}^{-1} \text{ cm}^{-1}$) at 260 nm [166]. The decrease in the Soret band absorption of IC_{p6}-Cu upon addition of CT-DNA (hypochromism) was used to calculate the binding parameters [167].

2.3.6.2. DNA mobility shift assay

For DNA mobility shift assay, 200 ng pUC19 plasmid DNA was mixed with different the concentration of IC_{p6}-Cu (0, 10, 50 and 100 μM) in 50 mM Tris -HCl (pH 7.4) buffer and left at room temperature for 2 h, in dark to allow binding. Each sample was mixed with gel loading buffer and 10 μl aliquot was loaded on 1% agarose gel containing 2.5 mg/ml EB. Electrophoresis was run in 1% TAE (Tris/Acetate/EDTA) buffer at 100 mV for \sim 1 h. The DNA on the gel was visualized by UV illuminator.

2.4. Methods used in studies on PDT efficacy of ICp₆-Cu

2.4.1. Intracellular uptake of ICp₆-Cu and Cp₆

The monolayer of cells ($\sim 2 \times 10^5$ cells) grown in 24 well plate was incubated in DMEM medium containing 10 μ M ICp₆-Cu and Cp₆ for 3 h at 37 °C, in dark. The cells were washed twice with PBS and solubilized in 200 μ l detergent solution (0.1 M NaOH + 0.1 % SDS) by scrapping and repeated pipetting. After centrifugation (10,000 rpm, 10 min), absorption of the cell extract at 640 nm and 660 nm for ICp₆-Cu and Cp₆ was measured respectively, on microplate reader. The protein content of each sample was determined by bicinchoninic acid (BCA) protein assay and a standard curve of ICp₆-Cu and Cp₆ prepared in NaOH/SDS solution was used to calculate the amount of ICp₆-Cu and Cp₆ in cells extracts (nM/ μ g of protein) [168].

2.4.1.1. BCA method of protein estimation

The protein concentration of cell lysates was measured by BCA method, which is based on the principle of reduction of Cu²⁺ ions from the copper(II) sulfate to Cu⁺ by peptide bonds in a temperature-dependent reaction. The amount of Cu²⁺ reduced is proportional to the amount of protein present in the sample. Reduced Cu⁺ forms a complex with BCA which is a purple-colored product that strongly absorbs light at a wavelength of 562 nm [169]. Following reagents were used for the assay, reagent A, B and C. Reagent A comprises of sodium carbonate monohydrate (8 gm) and sodium tartrate (1.6 gm), dissolved in 100 ml of distilled water and the pH of the solution is adjusted to 11.25 using 10 M NaOH. Reagent B comprises of 4.0 gm BCA dissolved in 100 ml distilled water and Reagent C consists of 0.4 gm penta hydrated cupric sulfate, in 10 ml water. Working solution of reagents was prepared by mixing reagent

A, B and C in the ratio of 26:25:1. For protein detection, an aliquot (10 μ l) of the sample was mixed with 90 μ l of working solution. Samples were heated at 60 °C for 60 min and after cooling the samples, absorbance was read at 562 nm on microplate reader. The concentration of the protein was determined from the standard calibration curve prepared using different concentrations of BSA.

2.4.2. Intracellular localization of ICp₆-Cu

The distribution of ICp₆-Cu in various cell organelles was studied by fluorescence imaging using a LSM 880 confocal microscope (Carl Zeiss, Germany). NT8e cells grown on glass bottom petri plates were incubated with 10 μ M ICp₆-Cu in DMEM medium for 3 h at 37 °C, in dark. The cells were then washed twice with PBS and stained with ER-tracker green, mitotracker green, lysotracker blue, Golgi tracker green or HO. The localization of ICp₆-Cu in cells was imaged by excitation with 405 nm diode laser and collection of emitted fluorescence 570 nm long pass filter on a high sensitivity GaAsP detector. HO and lyso Tracker blue were excited with 405 nm laser and fluorescence emission from 420 nm to 480 nm was imaged on PMT detector. Mito, Golgi and ER-tracker probes were excited at 488 nm with argon ion laser and emitted fluorescence from 490 nm to 560 nm were recorded on PMT detector.

2.4.3. Photodynamic treatment of cancer cells

For concentration-dependent phototoxicity experiments, the cells in 96 well plate were treated with different concentration of ICp₆-Cu (2–15 μ M) for 3 h, as mentioned in section 2.2.2. After treatment, the cells were irradiated with red light at a fixed dose of 7 J/cm², as described in section 2.2.3. For experiments on light dose dependent

phototoxicity, the cells were treated with a fixed concentration of ICp_6-Cu (10 μM , 3 h) and then irradiated with different light doses (0 –12.7 J/cm^2). The light dose was varied by changing the time of irradiation.

For studies on the effect of hypoxia on phototoxicity, the cells were treated with PS (10 μM , 3 h) and then the growth medium of cells was replaced with deoxygenated plane medium. This media was prepared by bubbling nitrogen gas for 1 h. The cells were then incubated under 1 % O_2 + 5 % CO_2 + 96 % N_2 environment at 37 °C for 1 h in a humidified incubator (ESCO, USA) to allow generation of hypoxia in cells. Subsequently, the 96 well plate was transferred in a sealed glass chamber and the chamber was flushed with nitrogen to ensure that hypoxia was maintained during irradiation. The cells were then irradiated with red light as described in section 2.2.3 at a fixed light dose (LD_{50} and LD_{80}). For studies on the effect of mechanistic probes of ROS (NaN_3 , histidine, DMSO and mannitol) on phototoxicity, the cells prior to the photodynamic treatment were incubated for 1 h in growth medium containing a specified concentration of each quencher and then irradiated with red light at a fixed (LD_{50}) light dose. After photodynamic treatments, the percent phototoxicity was determined by MTT assay as described in section 2.2.4.

2.4.4. Microscopy for PDT-induced cell death

PDT-induced changes in cellular and nuclear morphology were examined using an inverted microscope (Olympus, Japan). The cells were grown in plastic culture dishes, treated with the ICp_6-Cu for 3 h and then exposed to red light at $\sim 8 J/cm^2$ (LD_{80}). After ~ 3 h, each of the culture dishes from control and treatment groups was imaged at 20X magnification under phase contrast illumination.

To determine the percentage of cells undergoing apoptosis and necrosis, the cells after PDT were stained with HO (10 mg/ml) and PI (2.5 mg/ml) for 5 min, washed twice with PBS and observed under the inverted microscope. PI is a cell impairment dye and can only stain the cells in which plasma membrane integrity is lost due to necrotic damage. HO is cell permeable, which stains nuclei and allows visualization of chromatin condensation and fragmentation of apoptotic cells. The blue fluorescence of HO and red fluorescence of PI was visualized using excitation with 380–400 nm, barrier filter 440 nm. Images were recorded using a color CCD camera model ‘Prog Res Cfscan’ and a ProgRes Capture Pro Software (Jenoptik, Germany). A minimum of 500 cells were counted in each group and percentage of apoptotic, necrotic and live cells was calculated from the total number of cells counted.

2.5. Methods used in studies on the efficacy of ICp₆-Cu for PAT

2.5.1. X-ray irradiation

X-ray radiation of cells was carried out at beamline-7 of Indus –II synchrotron source at Raja Ramanna Centre for Advanced Technology, Indore India. The beam had a spectral band of energy 2.5–10 keV which was tuned to energy range of 8- 10 keV by inserting 396 µm thick aluminum filter in the beam path. The synchrotron radiation spectrum of the beam is shown in fig 2.1. The spectrum was obtained by simulation using XOP (X-ray Optics utilities) software [170, 171].

For irradiation, the 96 well plate was mounted vertically on a motorized stage in front of the source. The beam size was 3.5 X 70 mm which allowed simultaneous irradiation of 6 wells horizontally. The photograph of the experimental setup is shown

in scheme 2.1 and the image of the beam obtained by exposing Gafchromic film is shown in the inset.

The beam was fixed in the horizontal plane, while irradiations were performed by vertical translation of the stage, to ensure homogenous exposure. The variation in horizontal homogeneity of the beam was <7%.

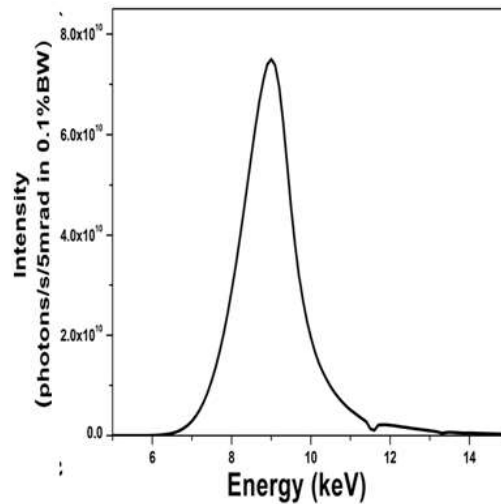
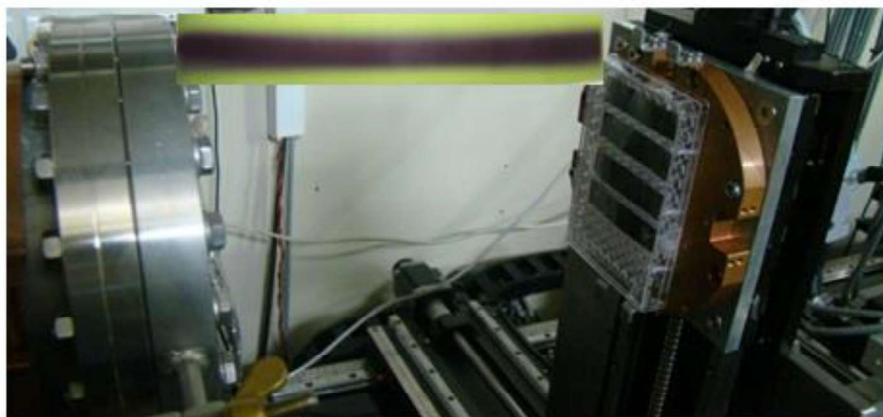


Figure 2.1. The emission spectrum of synchrotron X-ray in the energy range of (8-10 keV).



Scheme 2.1. Experimental set-up at X-ray lithography beamline (BL-7) used for X-ray irradiation of cells in 96 well plate. The plate was mounted vertically on to a motorized stage in front of the beam (beam size of 3.5 x 70 mm). The inset shows horizontal intensity distribution on Gafchromic film.

To take into account the ring current variation, all the experiments were done when the ring current was between 90-130 mA. For this, the time to initiate the sample preparation was adjusted accordingly. Further, prior to each exposure (samples in 96 well plate), the scan translation speed of the stage was adjusted accordingly to compensate for ring current variation. For each experiment, a plate containing Fricke solution was also exposed to ensure that the total dose delivered per sample was nearly same in different experiments.

2.5. 2. XO-Fricke assay

Xylenol orange (XO) is a metal ion indicator, which binds with ferric ions Fe^{3+} formed as a result of ionizing radiation-induced oxidation of ferrous ions (Fe^{2+}), forming a 1:1 colored complex (XO-Fe^{3+}) with an absorption in the visible range. Fricke –xylenol orange dosimeter (FX) was prepared according to Gohary et al [171] with slight modification. FX solution composition was 1 mM ferrous ammonium sulfate (SD Fine chemicals), 50 mM sulphuric acid and 0.1 mM Xylenol orange. 300 μl of the solution was dispensed in each well of 96 well plates and irradiated as mentioned in section 5.3.1. The absorption spectra of irradiated Fricke Xylenol orange (FX) solution was recorded from 350-750 nm on microplate reader within 10 minutes of irradiation .

Fig 2.2a, shows the absorption spectra of irradiated Fricke Xylenol orange (FX) solution vs no. of scans. (5, 10, 20, 30, 40, 50). FX solution presents two absorption bands: one in the range from 435 -445 nm corresponding to Fe^{2+} ions initially present in non-irradiated FX solution and another in the range of 550- 560 nm, corresponding to Fe^{+3} ions generated by radiation-induced Fe^{+2} ions oxidation.

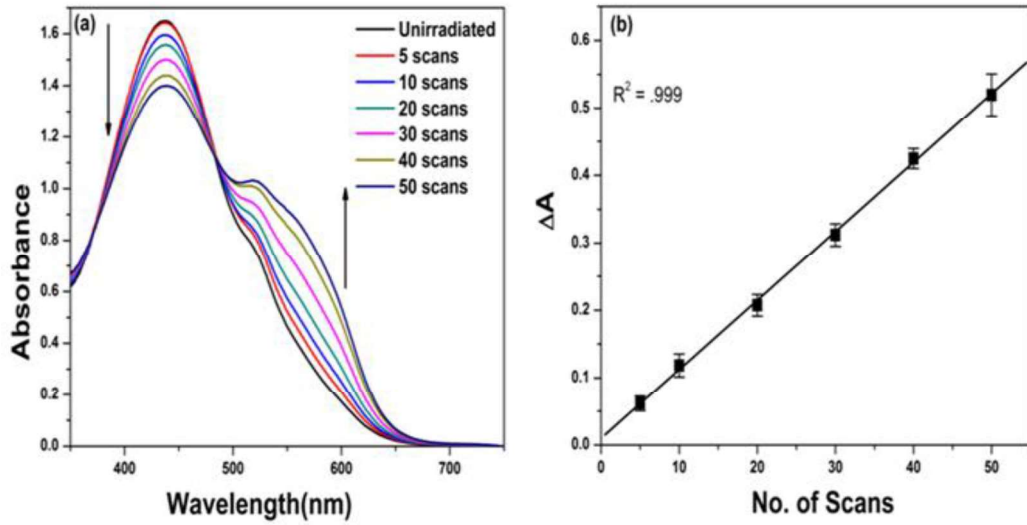


Figure 2.2. (a) The absorbance spectra for irradiated samples of Xylenol orange Fricke solution. (b) The dose-response plot of the change in absorbance at 560 nm (ΔA) of Xylenol orange Fricke solution vs No. of scans. Data represent mean \pm SD obtained from three independent experiments.

With the increase in dose delivered, the 435-445 nm band tends to decrease with concomitant increase in 550-560 nm band. Absorbed dose in the dosimetric solution was calculated as follows:

$$D_w = \frac{(1.004 \times \Delta A)}{(\epsilon G \rho d)} \quad (3)$$

Where, D_w = absorbed dose in FX solution (Gy)

ΔA = net change in absorbance at 560 nm

ϵ = molar extinction coefficient at 560 nm ($2000 \text{ m}^2 \text{ mol}^{-1}$)

ρ = density of FX solution (1024 Kg/m^3)

d = optical path length of FX solution (0.01 m)

G = radiochemical chemical yield ($1.37 \times 10^{-6} \text{ mol/ J}$ at a photon energy of 10 keV), according to International Commission on Radiation Units and Measurements (ICRU)

The value of ϵG was corrected for temperature and substituted in the equation (3)

$$\epsilon_t G_t = \epsilon G [1 + 0.007 (t - 25)] \times [1 + 0.0015 (t' - 25)] \quad (4)$$

Where, t = temperature ($^{\circ}\text{C}$) of FX solution during spectrophotometric measurement.

t' = temperature ($^{\circ}\text{C}$) of FX solution during irradiation which varied between 25 ± 3 $^{\circ}\text{C}$.

Following the above equations a graph of no. of scan vs ΔA was plotted (Fig. 2.2 b).

No. of scans and corresponding calculated absorbed dose is given in table 2.1 and an absorbed dose of $\sim 33.5 \pm 0.6$ cGy/scan was obtained.

Table 2.1. No. of scans and corresponding calculated absorbed dose

No. of scans	Absorbed dose (Gy)
5	1.775
10	3.55
20	7.1
30	10.65
40	14.2
50	17.75

2.5.3. Determination of cytotoxicity

The cells were treated with 10, 20, 30 μM of $\text{ICp}_6\text{-Cu}$ (3 h) as described in section 2.2.2, and irradiated with varying doses of X-ray from 1-17 Gy. Cells without $\text{ICp}_6\text{-Cu}$ treatment were irradiated in a similar manner. After the treatment, the growth medium from cells was replaced with fresh medium. The cells were incubated for 96 h and then the effect of treatment on cell viability was determined by MTT assay as described in section 2.2.4.

2.5.4. Clonogenic survival assay

Sensitizer enhancement ratio (SER) was determined by clonogenic survival assay. Cells were seeded in 24 well plates (~ 100 cells per well) and allowed to attach overnight. Then cells were treated with $\text{ICp}_6\text{-Cu}$ (10, 20, 30 μM) for 3 h, washed with

medium (without serum), and then irradiated with X-ray at a fixed dose of 7.0 Gy which was predetermined from cytotoxicity experiments. After irradiation, the cells were allowed to grow for 10 days to form colonies. The colonies were fixed in 4% paraformaldehyde stained with crystal violet and then counted. The surviving fraction (SF) was calculated as:

$$SF = \frac{\text{mean no.of colonies formed after treatment}}{\text{no.of cells seeded} \times PE} \quad (5)$$

Where, PE (plating efficiency) was determined as:

$$PE = \frac{\text{mean no.of colonies formed in untreated control}}{\text{no.of cells seeded}} \times 100 \quad (6)$$

$$SER (7 Gy) = \frac{SF \text{ at } 7 \text{ Gy of radiation alone}}{SF \text{ at } 7 \text{ Gy of radiation} + ICp6-Cu} \quad (7)$$

2.5.5. Determination of intracellular ROS levels

For X-ray irradiation experiments NT8e and 4451 cells treated with 10, 20, 30 μM ICp₆-Cu (3 h) were irradiated with 7.0 Gy X-ray dose. Cells without ICp₆-Cu treatment were irradiated in a similar manner. After the treatment, intracellular levels of ROS were determined by DCFDA assay as described in section 2.2.5.

2.5.6. ICp₆-Cu induced DNA damage upon X-ray irradiation

The effect of X-ray irradiation either alone or combined with ICp₆-Cu (30 μM , 3 h) treatment on DNA damage and repair in oral cancer cells was determined by γ -H2AX immunofluorescence, a reliable and sensitive biomarker for DSBs detection [173]. For this, cells were grown on X-ray transparent Kapton film and subsequent to X-ray

exposure (~7.0 Gy) were incubated at 37 °C for 30 min, 2 h and 24 h. After the incubation period, the cells were washed two times with ice-cold PBS and fixed in 4% paraformaldehyde for 15 min at room temperature. The cells were washed three times with PBS, permeabilized by treatment with 0.5 % Triton X-100 for 5 min. After washing three times with PBS the cells were treated with 5 % BSA solution for 1 h to block non-specific binding sites. The cells were then incubated with mouse anti-human γ -H2AX antibody (dilution 1:200) for 1.5 h, washed twice with 0.05% Tween-20 in PBS and incubated with Alexa Fluor 488 labeled rabbit anti-mouse antibody (dilution 1:400) for 1 h. After a final wash with PBS for 10 minutes, cells were counterstained with DAPI (1 μ g / ml) for 5 min and the fluorescence in cells was examined on confocal microscope. Alexa Fluor was excited at 488 nm and its fluorescence was recorded in channel 1 with a bandpass of 490 – 560 nm. DAPI was excited at 405 nm and its fluorescence between wavelengths of 420-480 nm was recorded in channel 2. Images were captured using 40X objective and analyzed by Image J software to count the number of γ -H2AX foci in each cell. For each treatment and control, the number of foci per cell was analyzed in at least 100 cells.

2.5.7. Cell cycle analysis

The effect of X-ray irradiation without and with IC_{p6}-Cu (30 μ M, 3 h) treatment on cell cycle and cell death was assessed by flow cytometry. After X-ray irradiation (7.0 Gy), the medium of cells was replaced with fresh medium and allowed to grow for 24 h and then the non-adherent cells in media were collected by centrifugation and the adherent cells were released by trypsinization. The adherent and non-adherent cells were mixed, washed with PBS, re-suspended in ice-cold 70% ethanol and stored at 4 °C until analysis. For flow cytometry measurements, the cells were centrifuged,

washed in PBS and re-suspended in 1.0 ml of PBS containing 50 $\mu\text{g} / \text{ml}$ PI. The cells were kept at 4 $^{\circ}\text{C}$ in dark for ~ 18 h, and the DNA content in cells was measured on Cyflow cytometer (Partec, Germany). The percentage of cells in G1, S, and G2/M phases of the cell cycle were analyzed from DNA histograms. The sub-G1 hypodiploid DNA content peak in the histogram was used to determine apoptotic population [174].

2.6. Methods used in studies on the chemotoxic potential of IC_{p6}-Cu

2.6.1. Treatment of cells with IC_{p6}-Cu

For determination of the cytotoxic effect of IC_{p6}-Cu in dark, cells were incubated in growth media containing varying concentration of IC_{p6}-Cu (10-100 μM) for 48 h, in dark. Further, for studies on the effect of antioxidants on chemotoxicity of IC_{p6}-Cu, the cells were first treated with GSH (1.0 mM) and trolox (10 μM) for 2 h. Cells were then washed with plain medium (without serum) and subsequently treated with IC_{p6}-Cu (50 μM) for 24 h and 48 h. For control, cells incubated in growth medium without GSH and trolox were subjected to IC_{p6}-Cu treatment under similar condition.

2.6.2. Determination of cytotoxicity

After treatment of cells with IC_{p6}-Cu as described above, the effect of treatment on cell viability was determined by MTT assay as described in section 2.2.4.

2.6.3. Cell proliferation assay

The effect of IC_{p6}-Cu treatment on proliferation of cancer cells in dark was determined by multiple time point MTT assay [175]. This method allows

determination of growth inhibition (antiproliferative) as well as the cytotoxic activity of the test compounds [176, 177]. A similar method developed by National Cancer Institute in which MTT is replaced with sulforhodamine B is widely used for the large-scale screening of potential anticancer agents [178]. Cells were incubated in growth media containing 10, 20 and 50 μM $\text{ICp}_6\text{-Cu}$ for 3, 6, 12, 24, and 48 h in dark. For each time point, a set of control without $\text{ICp}_6\text{-Cu}$ treatment was used. At the end of incubation, MTT assay was performed for each set of control and treated cells as described in section 2.2.4. The absorbance value obtained for control at 0 time point (C_0), $\text{ICp}_6\text{-Cu}$ treated cells at various time points (T) and the corresponding control at each time point (C), were used to obtain percent cell proliferation using the following equation:

$$\frac{T}{C} [\%] = \left[\frac{(T-C_0)}{(C-C_0)} \right] \times 100 [\%] \quad (8)$$

The value of T/C % denotes the effect of the compound on the cell growth where the value of 100 % indicates no effect on cell growth, the values between 100 and 0 % indicates a cytostatic effect and the value below 0% shows cytotoxic effect.

2.6.4. Confocal microscopy for the study of cellular morphology and cell death

To identify changes in cellular morphology due to necrosis and apoptosis, HO and PI double staining procedure was used. Cells were grown on glass bottom cell culture petri dishes and treated with 50 μM $\text{ICp}_6\text{-Cu}$ for 48 h in dark and stained with PI- HO as mentioned in section 2.4.4. The fluorescence of HO and PI was visualized using a combination of excitation laser/emission wavelengths as 405 nm / 420-480 nm and

488 nm / 610-680 nm, respectively. For cell morphology, bright-field DIC images were captured using transmitted light PMT detector.

To visualize lysosomal membrane permeabilization, the cell monolayer after treatment with *ICp₆*-Cu (50 μ M, 48 h in dark) was stained with AO (5 μ M). After washing, the red fluorescence of AO in cells was imaged using a combination of excitation laser/emission wavelengths as 488 nm / 600-660 nm. F-actin filaments of the cytoskeleton in cells were visualized by staining the cells with Alexa Fluor 488 labeled Phalloidin. After counterstaining with DAPI (1 μ g / ml), the fluorescence of Phalloidin and DAPI in cells was imaged using a combination of excitation laser/emission wavelengths as 488 nm/550-660 nm and 405 nm/420-480 nm, respectively.

2.6.5. Determination of intracellular ROS levels

For determination of *ICp₆*-Cu induced intracellular ROS generations, NT8e and HaCaT cells were treated with *ICp₆*-Cu (10 and 50 μ M) for 3, 6, 12, 24 and 48 h in dark. After the treatment, intracellular levels of ROS were determined by DCFDA assay as described in section 2.2.5.

2.7. Statistical analysis

All the experiments were performed at least three times using three replicates in each experiment. The data obtained from three independent experiments were plotted as mean \pm SD and Student's t-test was applied for comparisons between different treatments. The value of $p < 0.05$, $p < 0.01$ and $p < 0.005$, was considered to be statistically significant.

Chapter 3

Characterization of ICp₆-Cu

3.1. Introduction

The objective of the present study was to explore the possibility to improve the photodynamic activity of *Cp₆*, a chlorophyll derivative by simultaneously attaching high Z metal and a halogen in the molecule. For this, conjugating *Cp₆* with copper iodide appeared an attractive strategy taking into account the concern of toxicity of non-essential metals and the important advantages offered by copper and iodine as essential trace elements and potential for multimodal cancer therapy and imaging (as described in chapter 1).

Generally, tetrapyrrole compounds can chelate various metal ions by forming a coordination complex between metal ion and pyrrole –NH groups at the center of the macrocycle. However, such metal complexes generally suffer from the drawback of aggregation due to ionic interaction between positively charged metal ion and the electron cloud of the tetrapyrrole ring [179]. Interestingly, studies have shown that tetrapyrrole compounds having free carboxyl groups can form complex with metal ion through coordination with the side chain carboxyl groups instead at the pyrrole nitrogen [180]. *Cp₆* contains two adjacent carboxylic groups at C13 and C15 position and one carboxylic group at propionic side chain at C17 (fig 3.1) and it was thought that *Cp₆* can be conjugated to copper iodide at the carboxylic groups through coordination. This strategy proved successful and the conjugate thus obtained was first characterized by various spectroscopy techniques to confirm its chemical structure and then its photodynamic activity using fluorescence probes and mechanistic probes of ROS. In addition, the interaction of the conjugate with serum albumin, a major drug carrier protein [181, 182], and DNA, a most probable target of metal complexes has also been characterized using absorption and fluorescence spectroscopy [183, 184].

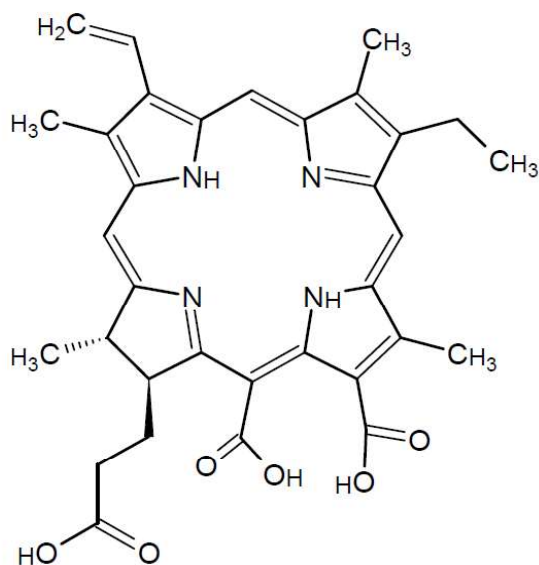


Figure 3.1. Structure of Cp_6

3.2. Results

3.2.1. Characterization of structure

3.2.1.1 Formation of the complex of Cp_6 with CuI

Cp_6 ($5 \mu\text{M}$) upon addition of CuI showed remarkable changes in its absorption spectrum 3.2 a. With the increase in the concentration of CuI , the Q band absorbance of Cp_6 at 663 nm gradually decreased with the concomitant appearance of a new band at 634 nm. This was also accompanied by a decrease in absorbance at the Soret band (400 nm) and the minor Q band (500 nm). Beyond equimolar ($5 \mu\text{M}$) concentration, CuI did not lead to any further change in the absorption spectrum of Cp_6 . This indicated that the complex formation between Cp_6 and CuI occurred at 1: 1 stoichiometry. As compared to Cp_6 (fig 3.2.) the molar extinction coefficient (ϵ) of the complex at major Q_y band was nearly same ($24,000 \text{ M}^{-1} \text{ cm}^{-1}$) whereas the ϵ at the Soret band was decreased by $\sim 30\%$ ($63,000 \text{ M}^{-1} \text{ cm}^{-1}$) (fig 3.2 a). The resultant

complex displayed a Soret band peaking at 408 nm with a shoulder at 380 nm, a minor Q_x band at 500 nm and the major Q_y band at 634 nm (fig 3.2 a). Further, as compared to Cp_6 , the fluorescence yield of Cp_6-CuI was reduced by an order of 10 (fig 3.2 b). X-Ray fluorescence (XRF) spectrum of the complex (fig. 3.3) revealed the characteristic X-ray emission lines for copper at 8.03 keV (K_α) and 8.9 keV ($K_{\beta 1}$) and for iodine at 3.97, 4.25, 4.5, 4.81 keV ($L_{\alpha 1}$, $L_{\beta 1}$, $L_{\beta 2}$, $L_{\gamma 1}$) and thus confirmed the presence of both copper and iodine in the complex.

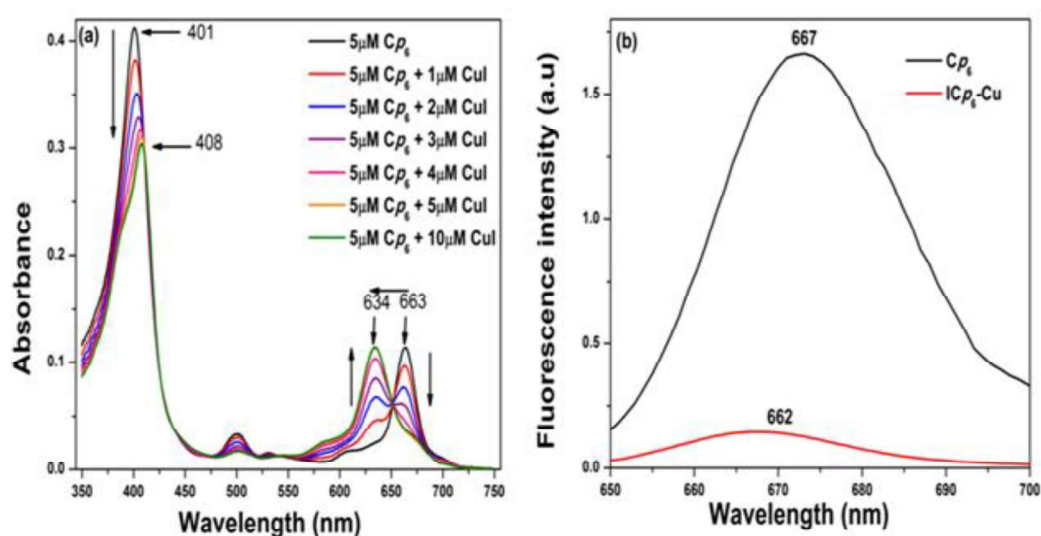


Figure 3.2. (a) Changes in absorption spectra of $5.0\mu M Cp_6$ with the subsequent increase in the concentration of CuI in methanol. (b) Fluorescence spectra of Cp_6 and Cp_6-CuI in phosphate buffer (pH 7.4).

3.2.1.2. Position of copper and iodine in the complex

To confirm the coordination site of copper in Cp_6-CuI , its Electron Paramagnetic Resonance (EPR) spectrum was measured at 100 K in methanol (fig. 3.4). The characteristic anisotropic spectrum of Cu^{2+} with intense absorption in high field region and well resolved hyperfine splitting in low field region was obtained. The value of g-tensor ($g_{||}$) and hyperfine splitting ($A_{||}$) was 2.27 and $174 \times 10^{-4} cm^{-1}$, respectively. No hyperfine splitting was observed in the g_{\perp} region.

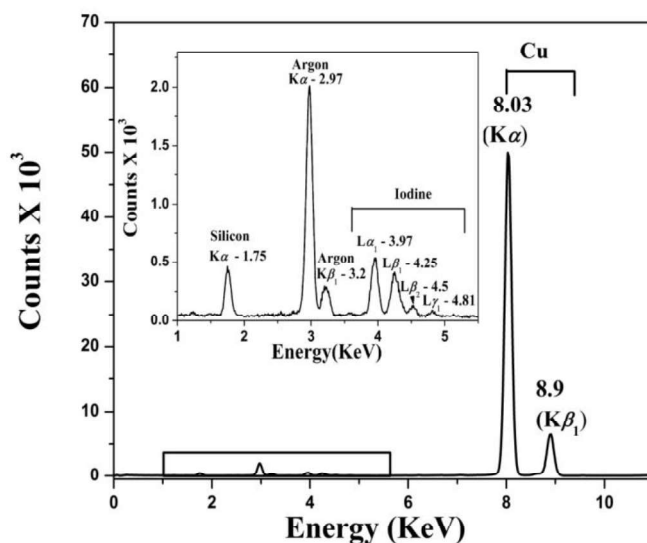


Figure 3.3. XRF spectrum of Cp_6-CuI showing characteristic X-ray emission lines for Copper and Iodine (inset). X-ray emission lines for copper at 8.03 keV (K_α) and 8.9 keV ($K_{\beta 1}$) and for iodine at 3.97, 4.25, 4.5, 4.81 keV ($L_{\alpha 1}$, $L_{\beta 1}$, $L_{\beta 2}$, $L_{\gamma 1}$). The peak at 2.97 keV and 3.2 keV is due to atmospheric argon and the peak at 1.75 keV is due to the silicon wafer on which powdered sample is deposited.

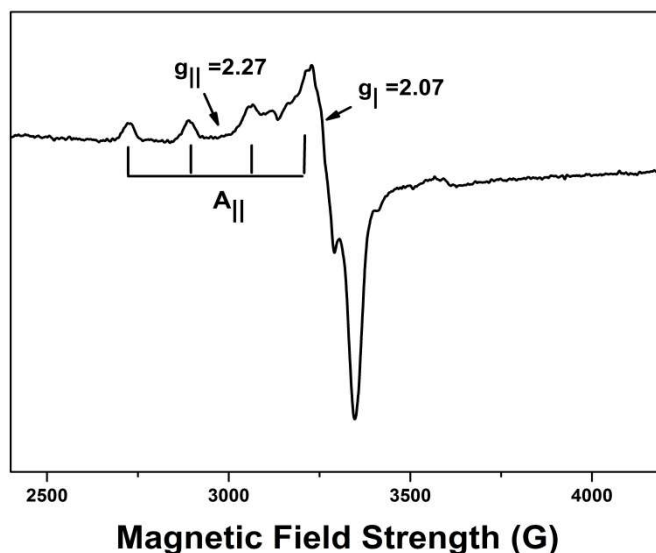


Figure 3.4. ESR spectrum of Cp_6-CuI at 100 K in methanol.

To infer the nature of metal-ligand bond, covalency parameter α^2 was calculated from the following equation.

$$\alpha_{Cu}^2 = -(A_{||}/0.036) + (g_{||} - 2.003) + 3/7(g_{\perp} - 2.003) + 0.04 \quad (9)$$

A value of $\alpha^2 = 0.5$ indicates complete covalent nature and if the value is 1.0 it indicates ionic bonding [185]. The value of α^2 for Cp_6-CuI is 0.82 which indicated that the nature of bonding between ligand and copper has some covalent character.

The FTIR spectra of Cp_6-CuI and Cp_6 are presented in fig. 3.5. The FTIR spectrum of Cp_6 appeared very similar to the FTIR spectrum of Chlorin e6 reported by Gladkova et al [186]. This was expected because the chemical structure of Ce6 is similar to Cp_6 except for the presence of one extra methylene ($-CH_2-$) group at the C15 position. As compared to Cp_6 , the Cp_6-CuI conjugate showed following difference in the FTIR spectra (fig 3.5 b). (1) appearance of three new bands, one at 1637 cm^{-1} due to CO– metal stretch and two prominent bands at 1112 cm^{-1} and 1203 cm^{-1} due to CO stretching [187, 188], (2) As compared to the prominent COO vibration bands observed in Cp_6 as a peak at 1558 cm^{-1} and shoulders at 1578 cm^{-1} and 1596 cm^{-1} , these band in Cp_6-CuI were very broad and one of the band at 1578 cm^{-1} was disappeared and (3) In Cp_6 , the CO vibrations of C13 and C15 carboxylic group appeared as distant bands at 1419 cm^{-1} and 1321 cm^{-1} , whereas in Cp_6-CuI complex, these are shifted to lower frequency at 1396 cm^{-1} and 1313 cm^{-1} , respectively. The C=O vibrational band in the region 1740 cm^{-1} due to carboxylate group at C17 propionic side chain was present both in Cp_6 and Cp_6-CuI indicating that it is not involved in complex formation [186]. In addition, the FTIR spectrum of Cp_6-CuI revealed an intense broad absorption band at 3400 cm^{-1} (Fig. 3.5 c), due to O-OH stretching [187] which suggested the presence of water molecules in the coordination sphere of copper.

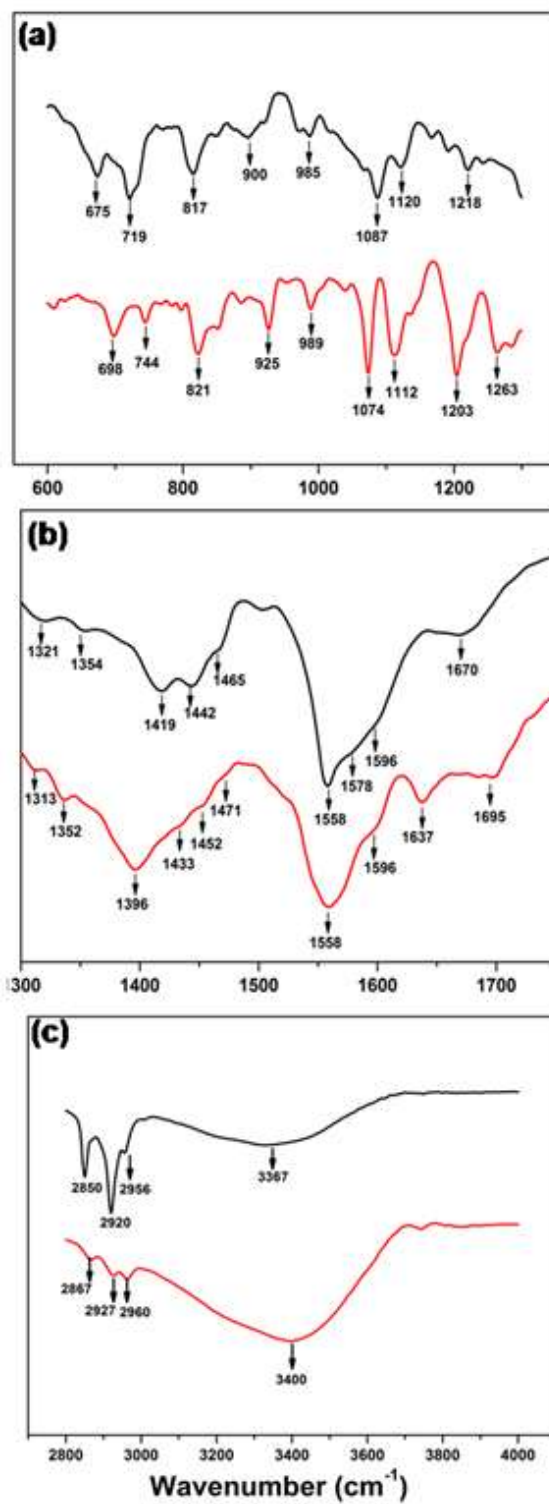


Figure 3.5. FTIR spectra of Cp_6 (black) and Cp_6-CuI (red) plotted in the range of (a) 600- 1250 cm^{-1} , (b) 1300-1750 cm^{-1} and (c) 2800-4000 cm^{-1} .

The mass spectrum of Cp_6-CuI is shown in fig. 3.6. The molecular ion containing copper can be identified by the characteristic isotopic splitting at 724.12 m/z and 726.12 m/z which represent the loss of C17 carboxylate from the molecule. The largest peak observed at 701 m/z showed no such isotopic splitting and hence represents molecular ion with loss of metal. This value matched with the calculated mass of molecule having iodine atom but no vinyl side group. This also ruled out the possibility of iodination at vinyl group, as reported in some previous studies [189]. Based on evidence gathered from XRF (fig. 3.3), EPR (fig. 3.4), FTIR (fig. 3.5), and HRMS (fig. 3.6), the conjugate was referred as ‘Iodinated Chlorin p_6 –copper complex’ (ICp_6-Cu) and its proposed chemical structure is shown in fig 3.7.

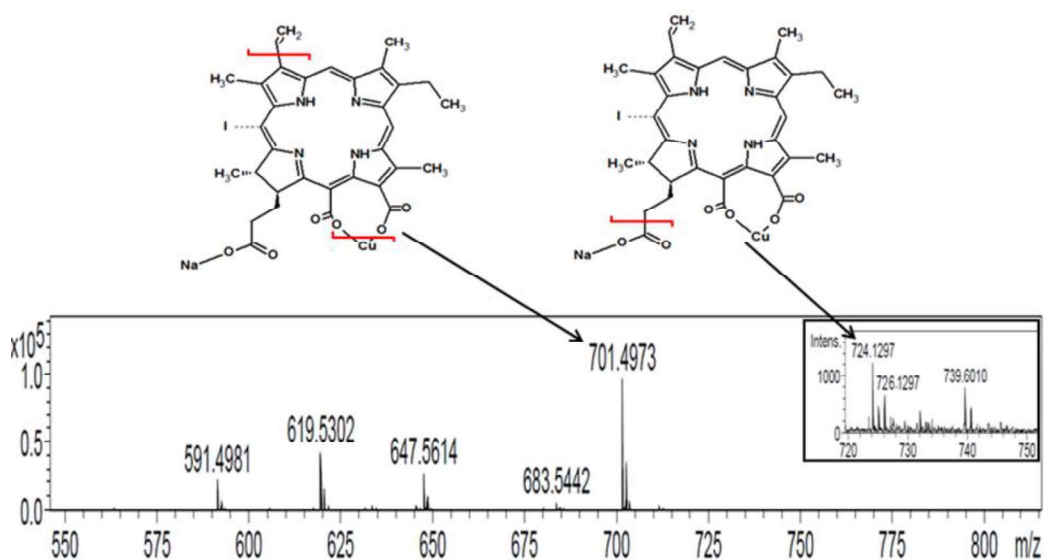


Figure 3.6. Mass spectrum of Cp_6-CuI in the range 550–800 m/z, showing molecular ion at 701 m/z (after loss of Cu and a vinyl (C_2H_3) from parent molecule) and spectrum magnified in the range 720–750 (inset) to show peaks of isotopic ion at 724.12 m/z and 726.12 m/z due to presence of natural isotopes of copper ^{63}Cu and ^{65}Cu (after loss of $-COONa$ from parent molecule).

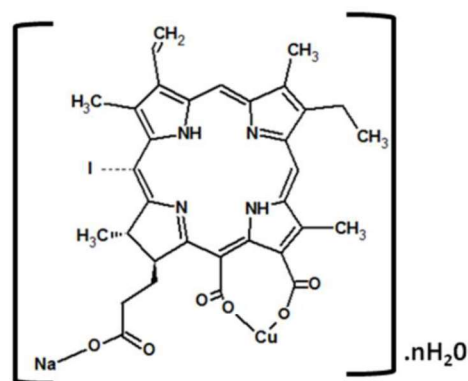


Figure 3.7. Proposed structure of ICp_6-Cu . The probable site of iodine is indicated by the dashed bond.

3.2.1.3. Octanol/ water partition coefficient

Cp_6 at physiological pH (7.4) is mostly hydrophilic due to the presence of three ionizable carboxylic groups, one as propionate side chain at the C17 position and remaining two attached at adjacent C13 and C15 position. Therefore, to assess whether attachment of copper at carboxylic groups has any effect on hydrophilicity, the partition coefficients (Log p) of Cp_6 and ICp_6-Cu was determined in 1-octanol–sodium phosphate buffer (pH 7.4) system. The results are presented in table 3.1. As compared to Cp_6 , the log p value of ICp_6-Cu complex was significantly higher, indicating a increase in its hydrophobicity.

Table 3.1. Octanol/ water partition coefficient of Cp_6 and ICp_6-Cu

Photosensitizer	Log P
Cp_6	0.56 ± 0.065
ICp_6-Cu	0.84 ± 0.054

3.2.2. Photodynamic activity in aqueous solution

3.2.2.1. $^1\text{O}_2$ and ROS generation efficiency of $\text{ICp}_6\text{-Cu}$

The $^1\text{O}_2$ and ROS generation efficiency of $\text{ICp}_6\text{-Cu}$ was measured using three different fluorescence probes SOSG, DCFH and APF. SOSG is specific for $^1\text{O}_2$ [162], DCFH detects total ROS [163] and APF can detect $\cdot\text{OH}$ as well as $^1\text{O}_2$ [164]. The $^1\text{O}_2$ or ROS generated in photochemical reaction converts these probes into highly fluorescent species. The change in fluorescence intensity (F_t/F_0) of SOSG and DCF as a function of irradiation time were plotted to compare the $^1\text{O}_2$ and ROS generation capability of Cp_6 (fig. 3.8 a) and $\text{ICp}_6\text{-Cu}$ (fig. 3.8 b). For $\text{ICp}_6\text{-Cu}$, the relative increase in SOSG fluorescence is 10 times less than that for Cp_6 (fig. 3.8 a and b). The capability of $\text{ICp}_6\text{-Cu}$ to generate other ROS was also assessed using fluorescence probe DCFH. The changes in DCFH fluorescence as a function of irradiation time for Cp_6 or $\text{ICp}_6\text{-Cu}$ is shown in fig. 3.8. Here, the increase in DCF fluorescence by Cp_6 was ~ 2 times higher than that for $\text{ICp}_6\text{-Cu}$, since the $^1\text{O}_2$ generation efficiency of $\text{ICp}_6\text{-Cu}$ was much lower (fig 3.8 b), these results indicated that increase in DCF fluorescence was due to the generation of other ROS. Whereas for Cp_6 , increase in DCF fluorescence is contributed predominantly by the generation of $^1\text{O}_2$ as seen in SOSG assay (fig. 3.8 a). These results show that the generation of other ROS by $\text{ICp}_6\text{-Cu}$ is substantially higher than the generation of $^1\text{O}_2$. To confirm this, changes in DCF fluorescence was monitored in the presence of NaN_3 , a quencher of $^1\text{O}_2$. However, the addition of NaN_3 to DCF solution led to an alteration in fluorescence of DCF which interfered with the measurement. Thus, a fluorescence probe, APF in presence of NaN_3 and D_2O (enhances lifetime of $^1\text{O}_2$) has been used to distinguish type I or type II photochemical mechanism of PDT drug as reported in a previous study [164]. For Cp_6

and ICp₆-Cu, the changes in fluorescence of APF (F_t/F_0) as a function of irradiation time are shown in fig. 3.9 a and b. For Cp₆, the increase in fluorescence of APF is inhibited to 50% and 90% in the presence of 5 mM and 10 mM NaN₃, respectively and it is enhanced by a factor of 4 in D₂O (fig 3.9 a). In contrast, for ICp₆-Cu induced increase in APF fluorescence is not significantly influenced by either NaN₃ or D₂O (fig. 3.9 b).

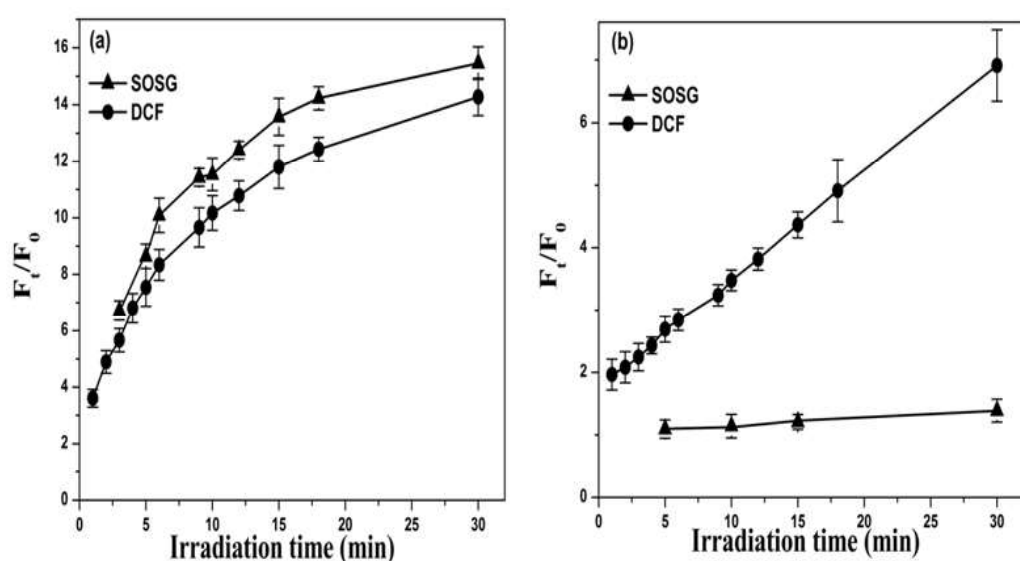


Figure 3.8. Cp₆ (a) and ICp₆-Cu (b) induced photodynamic generation of ¹O₂ and total ROS plotted as an increase in fluorescence (F_t/F_0) of SOSG and DCF, respectively. The solution of PS and fluorescence probe in phosphate buffer (pH 7.4) was irradiated with red light (3.5 mW/cm²) for different time periods. Each data point represents mean \pm SD value of three independent experiments.

3.2.2.2 Photobleaching of ICp₆-Cu and Cp₆

Photobleaching during light irradiation results in a decrease in the concentration of active PS at the target site which limits the overall effectiveness of PDT [61,190, 191]. The photobleaching of ICp₆-Cu and Cp₆ in sodium phosphate buffer (pH 7.4) as a function of irradiation time is shown in fig 3.10. It can be seen that \sim 40% of Cp₆ is photobleached within 18 minutes of irradiation and photobleaching increased with

increase in irradiation time. In comparison, for ICp₆-Cu only ~10% photobleaching was observed at 18 min of irradiation time and thereafter no significant increase in photobleaching was observed.

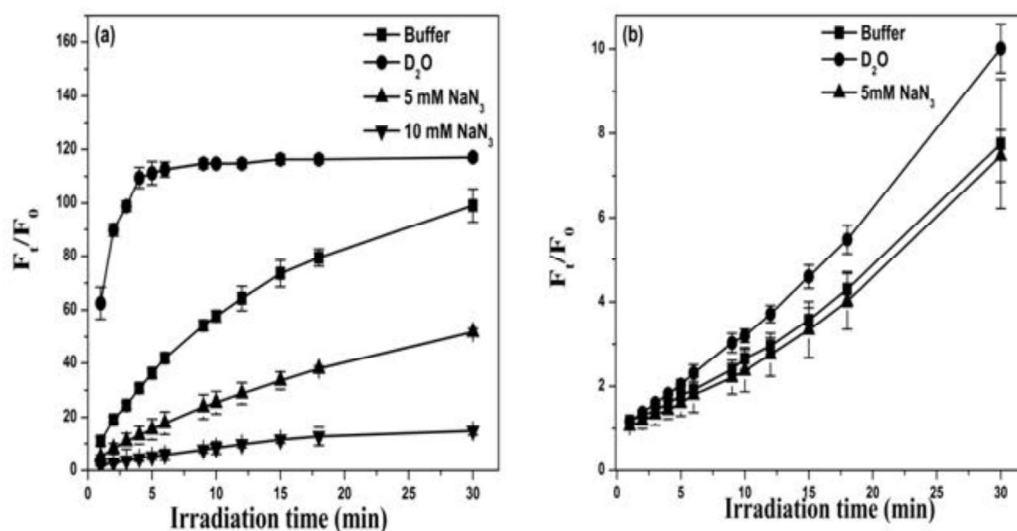


Figure 3.9. Cp₆ (a) and ICp₆-Cu (b) induced photodynamic generation of ROS plotted as an increase in fluorescence (F_t/F_0) of APF in buffer, D₂O and in buffer containing NaN₃ at 5 mM and 10 mM concentration. The solution of PS and fluorescence probe in phosphate buffer (pH 7.4) was irradiated with red light (3.5 mW/cm²) for different time periods. Each data point represents mean \pm SD value of three independent experiments.

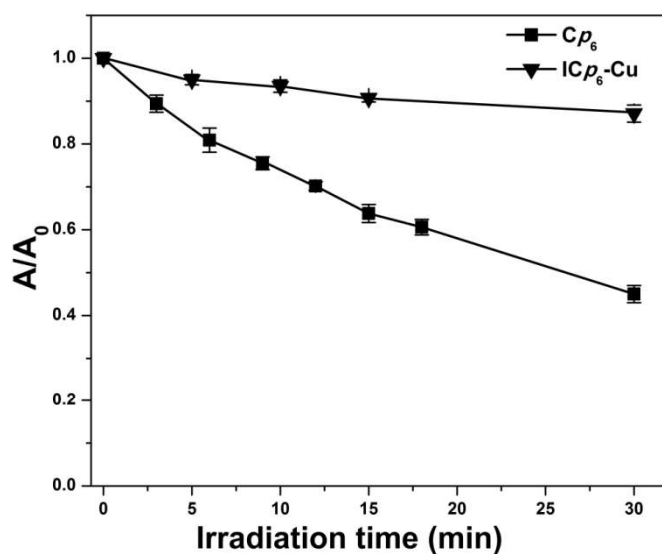


Figure 3.10. Photobleaching of Cp₆ and ICp₆-Cu in buffer as a function of irradiation time. Each data point represents mean \pm SD value of three independent experiments.

3.2.3. Interaction of ICp₆-Cu with HSA and DNA

3.2.3.1. Interaction and binding of ICp₆-Cu with HSA

The changes in absorption spectra of 5 μM ICp₆-Cu in phosphate buffer (pH 7.4) alone and upon addition of increasing concentration of HSA are shown in fig 3.11a. The Soret band at 405 nm and the major Q band at 628 nm of ICp₆-Cu showed a gradual red shift upon addition of HSA. The maximum redshift of 7.0 nm occurred at 4 μM HSA and these changes were accompanied by a slight decrease in the absorbance of the Soret band and increase in the absorbance of the Q band. Beyond 4 μM HSA, the absorption spectrum of ICp₆-Cu did not change both with respect to intensity and position of Soret and Q band indicating that interaction of ICp₆-Cu and HSA completed at a ratio of 5:4 (table 3.2). The fluorescence spectra of ICp₆-Cu in absence and presence of HSA are shown in fig 3.11b. The addition of 1-4 μM HSA to ICp₆-Cu led to a small decrease in its fluorescence intensity with redshift in peak position.

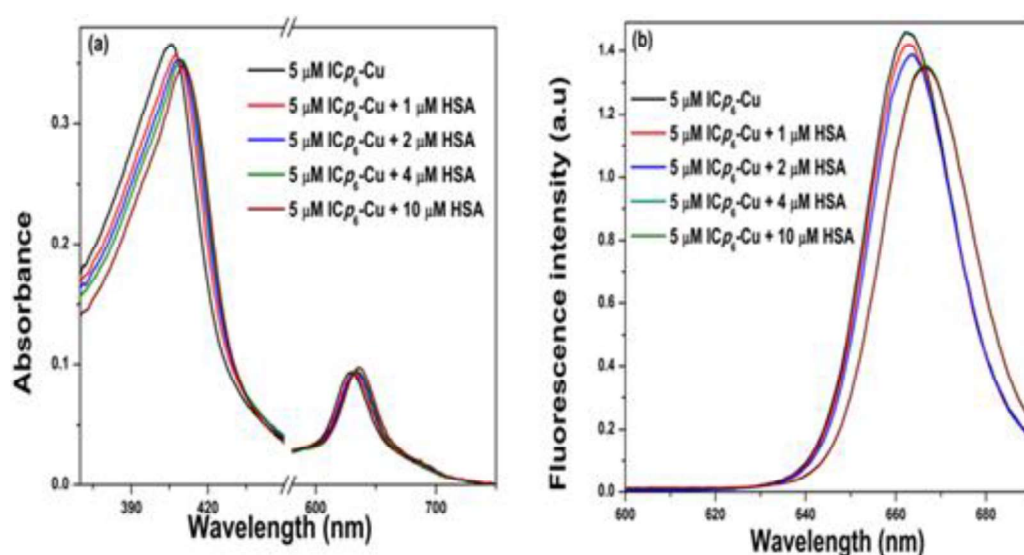


Figure 3.11. Absorption (a) and fluorescence (b) spectra of ICp₆-Cu (5 μM) alone and in the presence of 1.0 μM , 2.0 μM , 4.0 μM and 10.0 μM HSA in phosphate buffer (pH 7.4).

Further, the fluorescence lifetime of both Cp_6 and ICp_6-Cu were compared in absence and presence of HSA (table 3.3). It can be seen that the fluorescence lifetime of Cp_6 is increased upon addition of HSA, which is due to its disaggregation as reported previously [192]. In contrast, there is no change in the fluorescence lifetime of ICp_6-Cu upon addition of HSA.

Table 3.2. Absorption characteristics of ICp_6-Cu ($5\mu M$) with various concentration of HSA.

Concentration of HSA (μM)	Soret Band		Q band	
	λ_{max} (nm)	FWHM (nm)	λ_{max} (nm)	FWHM (nm)
0	405	47	628	32
1	407	47	630	32
2	409	47	632	32
3	410	47	633	32
4	411	47	635	32
10	411	47	635	32

Table 3.3. Average fluorescence lifetime (τ_{avg}) of ICp_6-Cu and Cp_6 in presence and absence of HSA ($5\mu M$). The value of χ^2 is given in parentheses.

Concentration of PS (μM)	τ_{avg} of Cp_6 (ns)		τ_{avg} of ICp_6-Cu (ns)	
	Without HSA	With HSA	Without HSA	With HSA
1	3.06 (1.05)	4.01 (1.07)	3.26 (1.08)	3.30 (1.01)
5	3.04 (1.03)	4.07 (1.05)	3.26 (1.04)	3.07 (1.05)
10	3.20 (1.08)	3.9 (1.03)	3.00 (1.00)	3.16 (1.07)

3.2.3.2. Fluorescence quenching of HSA by ICp₆-Cu

HSA upon absorption of ultraviolet light show intrinsic fluorescence emission from aromatic amino acid residues such as phenylalanine, Trp and Tyr. HSA is 585 amino acid long monomer protein, structurally organized into three homologous helical domains (I-III) and each domain contains two subdomains denoted as A and B [181]. Trp- 214 and Tyr -263 (main Tyr responsible for HSA fluorescence) are located close to the drug binding site at subdomain IIA [193, 194]. HSA contains 18 Tyr residues but mainly Tyr-263 is responsible for HSA fluorescence because remaining Tyr residues in HSA are completely buried inside the protein and suffer quenching of fluorescence [194].

The quenching of protein fluorescence by drug molecule is widely used as a sensitive assay to probe the interaction of HSA with drugs and determine binding parameters, such as the binding constant, number of binding sites and binding distance [195-197]. Fig. 3.12, shows the fluorescence spectra of HSA in the absence and presence of varying concentrations of ICp₆-Cu. With an increase in the concentration of ICp₆-Cu, there is a decrease in fluorescence intensity of HSA (330 nm) along with a gradual blue shift of the emission peak. To ascertain whether the fluorescence quenching involves collisional or static mechanism, the value of quenching rate constant was determined by analyzing the fluorescence quenching data according to following Stern- Volmer equation:

$$\frac{F_0}{F} = 1 + K_{SV}[Q] = 1 + K_q\tau_0[Q] \quad (10)$$

where F₀ and F are the fluorescence intensities of HSA in the absence and presence of the quencher, respectively, τ₀ is the average lifetime of the HSA in the absence of

quencher ($\tau_0 = 10^{-8}$ s) [198], $[Q]$ is concentration of quencher, K_q is the bimolecular quenching rate constant and K_{SV} is the Stern-Volmer quenching constant [199].

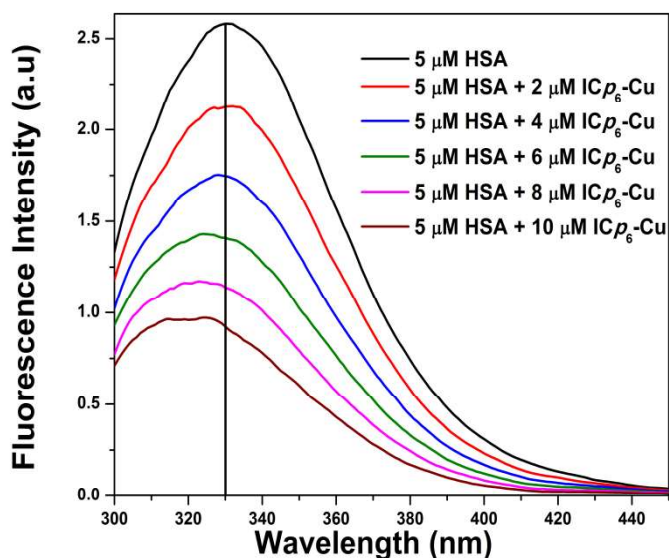


Figure 3.12. Changes in the fluorescence emission spectra of HSA (5.0 μM) on addition of different concentration of $\text{ICp}_6\text{-Cu}$ (0- 10 μM) in phosphate buffer (pH 7.4).

The value of K_{SV} ($0.95 \pm 0.07 \times 10^6$) was calculated from slope obtained from the linear fit from the plot of F_0/F vs $[Q]$. The value of K_q calculated from K_{SV}/τ_0 ratio for $\text{ICp}_6\text{-Cu}$ is in the order of $10^{13} \text{ M}^{-1}\text{s}^{-1}$ which is greater than the maximum scatter collision quenching constant of quenchers with albumin ($K_{\text{dif}} = 2 \times 10^{10} \text{ M}^{-1} \text{ s}^{-1}$) [200, 201]. These results suggest that quenching of HSA fluorescence is dominated by the static quenching arising due to specific interaction between HSA and $\text{ICp}_6\text{-Cu}$.

3.2.3.3. Binding constant and number of binding sites

When binding of a ligand with HSA involves static quenching of Trp fluorescence, the binding constant and the number of binding sites can be calculated from the following equation:

$$\log \left[\frac{F_0 - F}{F} \right] = \log K + n \log [Q] \quad (11)$$

where, F_0 and F are the fluorescence intensity in absence and presence of quencher, $[Q]$ is the quencher concentration [199]. The binding constant (K_b) $2.52 \pm 0.03 \times 10^6 \text{ M}^{-1}$ and number of binding sites (n) 1.2 ± 0.08 were obtained from values of y-intercept and slope, respectively from the plot of $\log [(F_0 - F) / F]$ vs $\log [Q]$ (fig 3.13).

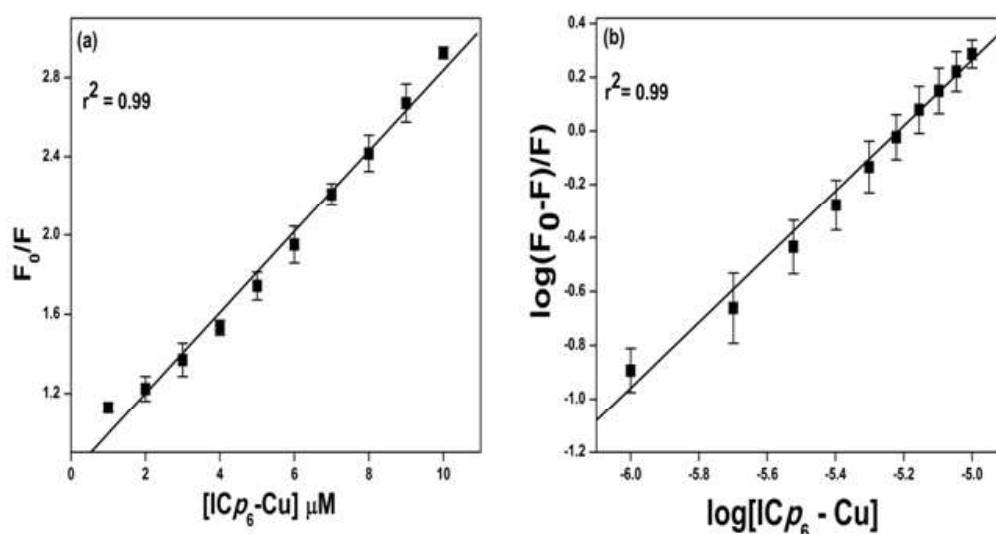


Figure 3.13. (a) Stern–Volmer plot of protein fluorescence quenching (F_0/F) vs concentration of ICp_6-Cu , (b) Double reciprocal plot of $\log [(F_0 - F)/F]$ vs $\log [ICp_6-Cu]$.

3.2.3.4. Proximity of ICp_6-Cu to tryptophan in HSA

The proximity of the bound ligand to the Trp in albumin can be confirmed from fluorescence quenching occurring due to the Forster nonradiative energy transfer (FRET) between the donor (Trp) and the acceptor (ligand) [199]. The possibility of FRET is likely when (1) there is overlap between the fluorescence emission and the absorbance spectrum of the donor and acceptor, respectively and (2) the distance between the two is less than 8 nm. As can be seen in fig 3.14 a, there is considerable overlap between absorption spectra of ICp_6-Cu (acceptor) and the fluorescence spectra

of HSA (donor). Therefore, the efficiency of energy transfer, E , between the two was computed according to Forster non-radiative energy transfer theory using the equation:

$$E = \frac{R_0^6}{(R_0^6 + r^6)} = \frac{(F_0 - F)}{F_0} \quad (12)$$

where, F and F_0 are the fluorescence intensities of HSA in presence and absence of PSs and r is the distance between acceptor and donor. R_0 is the critical distance when the transfer efficiency is 50%, which is given by the following equation:

$$R_0^6 = 8.8 \times 10^{-25} k^2 N^{-4} \Phi J \quad (13)$$

where, k^2 is spatial orientation factor between the emission dipole of donor and the absorption dipole of acceptor, N is the refractive index of the medium and Φ is the fluorescence quantum yield of the donor. For the experimental conditions used, the value of k^2 , N , and Φ were taken as 0.66, 1.336 and 0.188, respectively [199]. J is the overlap integral of the fluorescence emission spectrum of the donor and the absorption spectrum of the acceptor and is calculated from the given equation:

$$J = \frac{(\sum F(\lambda) \varepsilon(\lambda) \lambda^4 \Delta\lambda)}{(\sum F(\lambda) \Delta\lambda)} \quad (14)$$

where, $F(\lambda)$ is the corrected fluorescence intensity of the donor at wavelength λ and $\varepsilon(\lambda)$ is the molar absorption coefficient of the acceptor at wavelength λ .

From above equations, the value of J , R_0 , E and r for ICp₆-Cu were calculated as $2.8 \times 10^{-14} \text{ M}^{-1} \text{ cm}^3$, 2.922 nm, 0.397 and 3.1 nm respectively. The distance between ICp₆-Cu and Trp in HSA is < 8 nm, which further fulfills $0.5R_0 < r < 1.5R_0$ criteria for high probability of energy transfer from donor to acceptor. These results together strengthen the probability of binding of ICp₆-Cu close to Sudlow Site I where the Trp-214 residue is located. This is also in agreement with previously reported FRET distance for Cp₆ that binds to Sudlow Site I [199]. Here it is important to mention that

in most of the studies on tetrapyrrole compounds including Cp_6 , the FRET distance is generally calculated using a value of k^2 as 0.667 (2/3) considering that the motion of both Trp-214 and the bound chlorin is not very much restricted [199]. Considering the extreme value of k^2 as 4.0 [165], which applies when the motion of donor and acceptor is restricted (rigid orientation) the FRET distance for ICp_6 -Cu was 4.2 nm, which is well within the high probability of energy transfer from donor to acceptor.

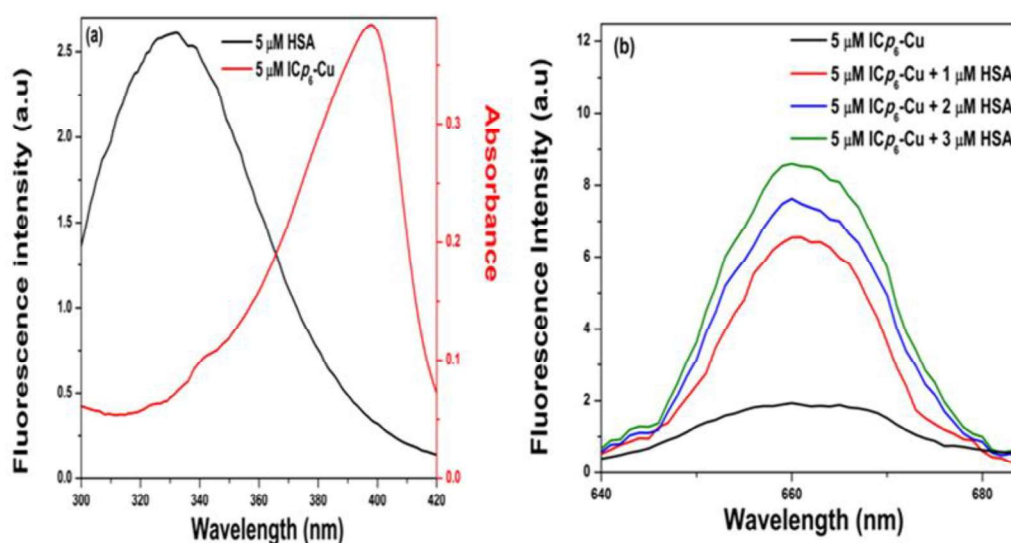


Figure 3.14. (a) Spectral overlap of fluorescence of 5.0 μ M HSA (λ_{ex} 280 nm) and absorption of 5.0 μ M ICp_6 -Cu in phosphate buffer (pH 7.4). (b) Fluorescence spectra (λ_{ex} = 280 nm) of 5.0 μ M ICp_6 -Cu alone and in the presence of 1.0 μ M to 3.0 μ M HSA in phosphate buffer (pH 7.4).

To confirm the possibility of FRET, fluorescence spectra of ICp_6 -Cu (5 μ M) were recorded in absence and presence of HSA (1-3 μ M) using λ_{ext} at 280 nm. As shown in fig 3.14 b, addition of 1 μ M HSA led to ~3 fold increase in the fluorescence intensity of ICp_6 -Cu. The magnitude of effect was increased further with an increase in the concentration of HSA. These results suggested an energetic interaction between excited Trp residue of HSA and unexcited ICp_6 -Cu. These results thus provide

evidence that the electronic excitation energy of HSA was transferred to bound ICp₆-Cu.

3.2.3.5. Effect of ICp₆-Cu on Protein conformation

The intrinsic fluorescence of Trp and Tyr residues in HSA is highly sensitive to the polarity of its environment and hence any change in the conformation of the protein caused by binding of the drug generally leads to a red shift in fluorescence as the environment around these residues becomes more polar [202]. In fig 3.15, synchronous fluorescence spectra of Trp and Tyr residue after addition of various concentrations of ICp₆-Cu in HSA is shown. With the increase in concentration of ICp₆-Cu, the fluorescence of both Tyr and Trp is gradually quenched but there is no change in the peak position of the spectrum. In the plot of F/F₀ versus [ICp₆-Cu] (fig 3.16), the slope of the curve obtained for $\Delta\lambda = 60$ nm was higher than the slope of the curve for $\Delta\lambda = 15$ nm. These results suggest that ICp₆-Cu binds close to Trp residue and the binding did not lead to any alteration in the conformation of the protein.

3.2.3.6. Effect of HSA binding on the stability of ICp₆-Cu

In fig 3.17 absorption spectra of ICp₆-Cu at various time intervals after incubation with HSA in dark is shown. There was no change in the absorption spectra of ICp₆-Cu even after prolonged incubation with HSA. This suggested that the interaction did not destabilize metal from ICp₆-Cu.

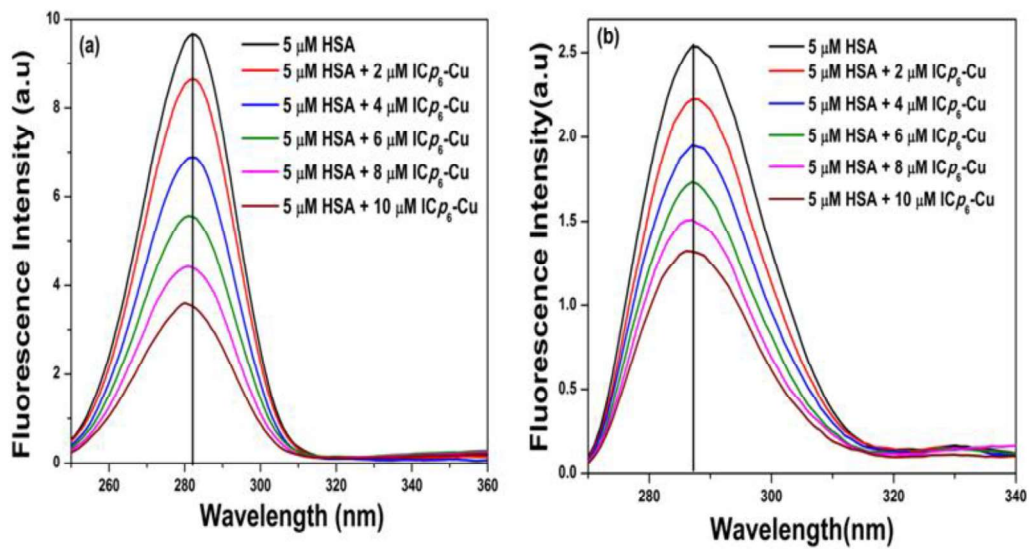


Figure 3.15. Synchronous fluorescence spectra of HSA (5.0 μM) alone and in the presence of different concentration of ICp₆-Cu (0-10 μM) recorded at $\Delta\lambda = 60 \text{ nm}$ and $\Delta\lambda = 15 \text{ nm}$ to resolve fluorescence of tryptophan (a) and tyrosine (b) residue respectively.

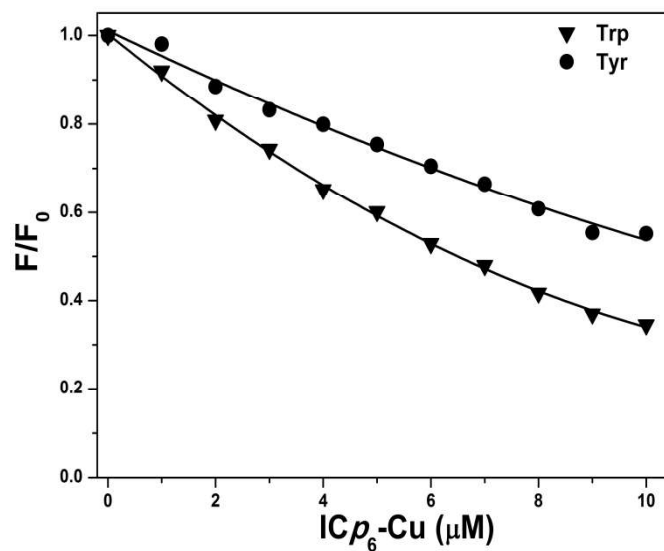


Figure 3.16. Fluorescence quenching (F/F_0) of tryptophan and tyrosine residue vs concentration of ICp₆-Cu.

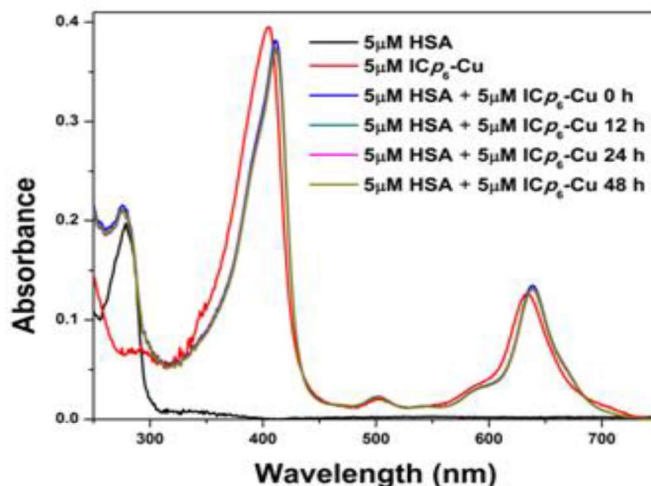


Figure 3.17. Absorption spectra of 5.0 μM $\text{ICp}_6\text{-Cu}$ in presence of 5.0 μM HSA after 0 h, 12 h, 24 h and 48 h of incubation in dark.

3.2.3.7. Binding affinity of $\text{ICp}_6\text{-Cu}$ with DNA

Metal complexes which can bind DNA through intercalation or covalently in cell-free system are generally expected to target cellular genomic DNA. The absorption spectra of $\text{ICp}_6\text{-Cu}$ in absence and presence of increasing concentration of CT-DNA is shown in fig. 3.18 a. $\text{ICp}_6\text{-Cu}$ (5 μM) exhibit an intense Soret band at ~ 405 nm and the minor Q band at ~ 628 nm. Upon addition of increasing concentration of CT-DNA (5–50 μM), the absorbance of $\text{ICp}_6\text{-Cu}$ at Soret and Q band gradually decreases without any shift in the position of Soret band peak. Hypochromism defined as the decrease in Soret band absorption upon addition of CT-DNA (fig 3.18 a), indicates the interaction between $\text{ICp}_6\text{-Cu}$ and DNA. The extent of hypochromism for $\text{ICp}_6\text{-Cu}$ (15%) was almost same as that for non-metallated Cp_6 (fig. 3.19 a). The binding constant (K_b) of $\text{ICp}_6\text{-Cu}$ and Cp_6 with CT-DNA was calculated using following equation [167]:

$$\frac{[\text{DNA}]}{(\epsilon_a - \epsilon_f)} = \frac{[\text{DNA}]}{(\epsilon_b - \epsilon_f)} + \frac{1}{(K_b(\epsilon_b - \epsilon_f))} \quad (15)$$

Where $[DNA]$ is the concentration of DNA, ϵ_f is the molar absorption coefficient of the ICp_6-Cu or Cp_6 in DNA free solution, ϵ_a is the molar absorption coefficient of the ICp_6-Cu or Cp_6 at a given DNA concentration, and ϵ_b is the molar absorption coefficient of the ICp_6-Cu or Cp_6 when fully bound to DNA. The Scatchard plot of $[DNA]/[\epsilon_a - \epsilon_f]$ vs $[DNA]$ is shown in fig. 3.18 b and 3.19 b. It gives $1/(\epsilon_b - \epsilon_f)$ as slope and $1/(K_b(\epsilon_b - \epsilon_f))$ as intercept. The ratio between slope and intercept gives the binding constant K_b . The value of K_b determined for ICp_6-Cu and Cp_6 was $6.8 \pm 0.4 \times 10^4 M^{-1}$ and $6.4 \pm 0.23 \times 10^4 M^{-1}$ respectively.

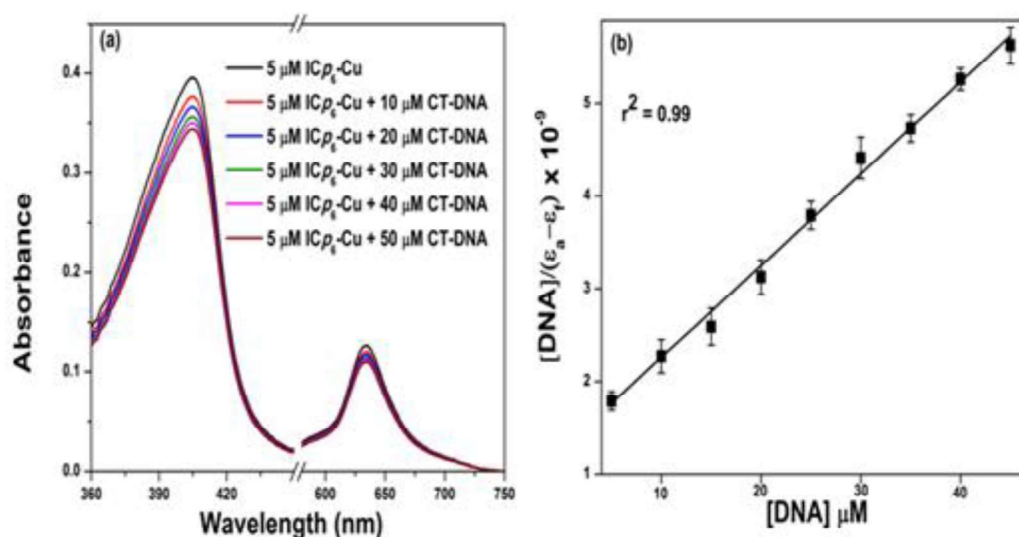


Figure 3.18. (a) Absorption spectra of 5.0 μM ICp_6-Cu in phosphate buffer (pH 7.4) in absence and presence of increasing amounts of CT-DNA (ICp_6-Cu : DNA molar ratio varied from 1:1 to 1:10). (b) Plot of $[DNA]/[\epsilon_a - \epsilon_f]$ vs $[DNA]$.

3.2.3.9. Gel –mobility shift assay

The binding of ICp_6-Cu with DNA was further verified by gel mobility shift assay. Upon electrophoresis, two forms of plasmid DNA are observed one corresponding to the supercoiled DNA (form I) and another one to the open-circle (form II) (fig. 3.20). Strong binding of a metal complex to DNA is expected to result in retardation in the mobility of supercoiled pUC19 DNA [203, 204]. However, there is no change in the

position of the band corresponding to the supercoiled DNA at any concentration of ICp₆-Cu (fig. 3.20). This shows that ICp₆-Cu did not affect the mobility of pUC19 and suggest the absence of strong binding with DNA.

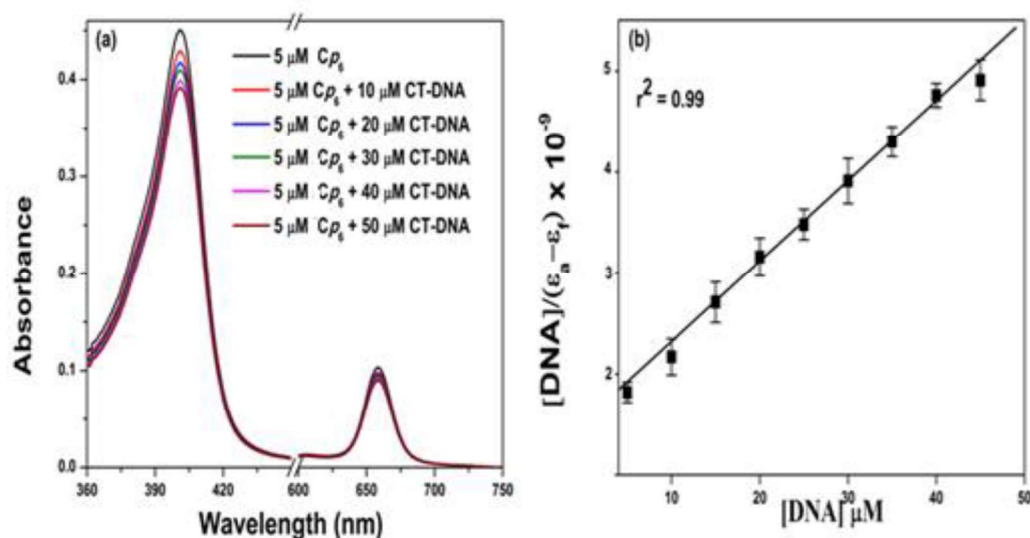


Figure 3.19. (a) Absorption spectra of 5 μM Cp₆ in phosphate buffer (pH 7.4) in absence and presence of increasing amounts of CT-DNA (Cp₆: DNA molar ratio varied from 1:1 to 1:10). (b) Plot of [DNA]/[ε_n - ε_f] vs [DNA].

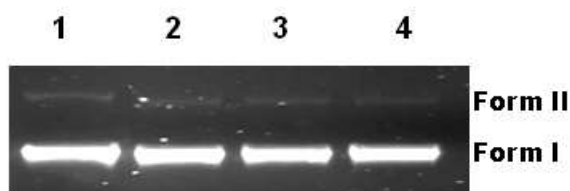


Figure 3.20. Image of agarose gel after electrophoresis of pUC19 plasmid DNA (200 ng) that was pre-incubated with different concentration (μM) of ICp₆-Cu for 2 h at 37 °C. Lane 1: Control, lane 2: 10 μM, lane 3: 50 μM, lane 4: 100 μM.

3.3. Discussion

3.3.1. Structural characterization

Results presented in this study demonstrate that Cp₆ readily reacts with copper iodide to results in the formation of new conjugate ICp₆-Cu having blue shifted Q band

absorption and low fluorescence yield. The observed changes in absorption and fluorescence properties were consistent with previous reports on the effect of insertion of copper on the optical properties of some chlorophyll derivatives [205], which were attributed to interaction between the Cu(II) orbitals and the π electrons of the tetrapyrrolic ring, that cause a decrease of the energy of the a_{1u} (π) and a_{2u} (π) orbitals relative to the e_g (π^*) orbitals [206]. The characterization of the ICp_6 -Cu complex by EPR, FTIR and mass spectroscopy revealed that the chemically ICp_6 -Cu is novel compound with a unique structure.

It is well documented that metallation of tetrapyrrole compounds leads to insertion of metal at the pyrrole -NH in the center of the tetrapyrrole ring. In copper complexes of porphyrin and chlorophyll derivatives, the EPR spectrum show characteristic multiple superhyperfine splitting in g_{\perp} region, due to the interaction of unpaired electron of metal with neighboring nitrogen nucleus [207]. As an example, the EPR spectrum of Copper-Chlorophyllin is shown in appendix. A. fig. A.1. In comparison, the EPR spectrum of ICp_6 -Cu did not reveal such superhyperfine splitting in g_{\perp} region and provided clear evidence that Cu^{2+} is not attached to pyrrole -NH. The results are also consistent with the previous report on metallation of carboxylic porphyrins, where it is shown that the insertion of metal ion at pyrrole -NH is not favored due to preferential binding of metal ion at the carboxylic groups through coordination [180]. The existence of such characteristic difference in EPR spectrum due to the difference in coordination is in agreement with a previous report on two different types of platinum(III) hematoporphyrin complexes, one having platinum attached to pyrrole -NH of tetrapyrrole ring and the other having platinum attached to side chain carboxylic groups [127]. Further, the co-ordination of copper with

carboxylic groups was evident from two other observations. First, according to Peisach–Blumberg correlation [208], the value of g-tensor and hyperfine splitting obtained from the EPR spectrum were within the range of values for copper coordinated with oxygen atoms. Second, the value of covalency parameter (α^2) was higher than that reported for Cu–N bond (0.63–0.68) in copper chlorophyll derivatives [185].

In the infrared spectrum of ICp_6-Cu , the appearance of a characteristic band of CO-metal stretch and two prominent bands due C–O stretching vibration provided additional evidence for the involvement of carboxylic groups in forming a coordination complex with Cu^{2+} . In a previous report also, the appearance of CO stretch bands was recognized as direct proof for the formation of chelate of copper and zinc with C13 keto group of chlorophyll [188]. The observations that the CO vibrations of C13 and C15 carboxylic group shifted to a lower frequency while C=O vibrational band of C17 carboxylate was not altered, suggested that that the two adjacent carboxylic groups at C13 and C15 position participate in the formation of the metal coordination complex. The appearance of a broad absorption band at $\sim 3400\text{ cm}^{-1}$ (fig 3.5 c) was due to the presence of water molecules in the coordination sphere of copper [187].

Generally, the site of halogenation in tetrapyrrole compounds can be identified by the disappearance of characteristic peak in the 1H NMR spectrum. However, because of the influence of paramagnetic copper, the 1H NMR spectrum ICp_6-Cu suffered line broadening and hence the peaks observed could not be interpreted (Appendix.A. Fig. A.2.). Alternatively, the analysis of mass spectrum provided substantial information on the site of iodination in ICp_6-Cu . The m/z value of major

molecular ion matched with the calculated mass of molecule having iodine atom but no vinyl side group. This ruled out the possibility of iodination at vinyl group and also suggested that iodine is attached to the chlorin macrocyclic ring. The changes observed in -CH stretch of substituents and the bands due to -CN and -CC vibrations also indicated the attachment of the heavy element iodide in the chlorin macrocycle. In substituted chlorins, halogenation generally takes place at four meso positions at C5, C10, C15 and C20. Previous reports on iodination of chlorophyll derivatives have shown that of the three meso positions at C5, C10, and C20, the meso position at C20 is relatively more reactive towards halogenations [209]. The selective iodination of chlorophyll-a derivatives at C20 position has been reported in several studies [209-211]. Based on evidence gathered from XRF (fig. 3.3), EPR (fig. 3.4), FTIR (fig. 3.5), and HRMS (fig. 3.6), the proposed chemical structure of ICp₆-Cu is shown in fig. 3.7. The site of iodination is indicated as most probable based on literature discussed above.

3.3.2. Mode of photodynamic action of ICp₆-Cu

Studies on characterization of photodynamic activity of ICp₆-Cu using fluorescence probes suggested that in contrast to Cp₆ which act mainly via ¹O₂, the photodynamic action of ICp₆-Cu is predominantly mediated through generation of other ROS in Type I photochemical process. Both copper and iodide attached to ICp₆-Cu are heavy atom and expected to improve the yield of ¹O₂ by increasing the efficiency of ISC from ¹PS* to the ³PS* [5, 37]. However, copper being paramagnetic also results in shortening of excited state lifetime which would decrease the ¹O₂ generation ability of the PS [38]. For this reason, the copper complex of porphyrin and

chlorophyll derivatives reported in the literature are photodynamically inactive [22, 39]. In contrast to copper, the insertion of iodine in the PS usually increases the Φ_t and results in an enhancement in the $^1\text{O}_2$ yield [40, 41]. However, it has also been reported that iodine depending on its position in the macrocyclic ring of the PS molecule can also affect the τ_t adversely and leads to decrease in $^1\text{O}_2$ yield [37]. The reason for this was attributed to orbital overlap between iodine atom and the tetrapyrrole ring which facilitate non-radiative decay of the $^3\text{PS}^*$ [37]. Thus, the decrease in $^1\text{O}_2$ yield of $\text{ICp}_6\text{-Cu}$ as a result of the insertion of copper was not counterbalanced by the presence of iodine atom, as expected. The results on generation of other ROS probed by DCF and APF suggest that while Cp_6 acts mainly via Type II mechanism, the photodynamic action of $\text{ICp}_6\text{-Cu}$ is mediated predominantly via Type I mechanism. It is also pertinent to note that PS which act via type I process such as copper octaethylbenzochlorin has been found useful for PDT of cancer both in in vitro and in vivo studies [35]. In fact, since type I mechanism is less dependent on the availability of O_2 , use of type I PS can provide an advantage that the tumor cells under hypoxic conditions can be treated effectively, as demonstrated in some studies [86, 212-214]. In addition, with type II PS, a major concern is that the excessive production of $^1\text{O}_2$ can rapidly destroy the PS and decrease the concentration of active PS at target site [190]. The results on photobleaching of two chlorins suggest that $\text{ICp}_6\text{-Cu}$ is more photostable than Cp_6 .

3.3.3. Ability of $\text{ICp}_6\text{-Cu}$ to bind with serum albumin

The characterization of albumin binding property of potential anticancer drug is considered important in terms of understanding its mode of transport and

accumulation in tumor. It is also believed that the macromolecular PS-protein complex can accumulate preferentially in tumor through enhanced permeability and retention (EPR) effect [50, 215].

The results of present study provided considerable evidence that HSA can act as a carrier protein for ICp_6-Cu and its binding did not affect the conformation of the protein. The first evidence came from absorption spectroscopy studies wherein ICp_6-Cu upon interaction with HSA exhibited significant changes in its absorbance spectrum that are characteristic of its localization in hydrophobic environment in the protein. The redshift of Soret and Q band indicates decrease in energy of the π to π^* transitions which can occur when the chlorin ring interacts with aromatic ligands in proteins via electrostatic or hydrophobic interactions [202]. In a previous study on interaction of Cp_6 with HSA, the Soret band absorbance of Cp_6 was observed to decrease initially at lower concentration of HSA and when HSA concentration was increased it led to hyperchromism and redshift of Soret band [192]. These spectral changes were attributed to the aggregation Cp_6 at low HSA: PS ratio (0.25) followed by its dis-aggregation and then formation of ground-state complexes between monomeric Cp_6 and HSA [192]. While ICp_6-Cu also showed decrease in Soret band absorption upon addition of HSA, there was one major difference that the increase in ICp_6-Cu showed redshift of Soret and Q band initially at lower concentration of HSA which is similar to red shift of Soret and Q band of Cp_6 when it forms monomeric complex with HSA [192]. The aggregation and dis-aggregation of Cp_6 upon addition of HSA was also reflected in its fluorescence spectrum as decrease in fluorescence intensity at lower HSA concentration and then an increase with redshift of the fluorescence band upon increase of HSA concentration [192]. Moreover, changes in

fluorescence spectra of ICp_6 -Cu (fig 3.11 b) upon addition of HSA were quite different from that observed for Cp_6 [192]. In addition, the FWHM (full width at half maximum) of Soret band and Q band did not increase upon the addition of HSA (table 3.2). This trend in absorption and fluorescence was otherwise expected if ICp_6 -Cu also aggregates and then dis-aggregates upon gradual increase in the concentration of HSA. These results suggest that the aggregation of ICp_6 -Cu did not occur upon interaction with HSA. Results of fluorescence lifetime measurements in absence and presence of HSA further confirmed that there is no aggregation of ICp_6 -Cu. Cp_6 contains three ionizable carboxylic groups and hence its interaction with HSA at physiological pH is mainly governed by electrostatic interaction [192]. Whereas, in ICp_6 -Cu, the two adjacent carboxylic groups are coordinated with Cu^{2+} and hence the net negative charge on the molecule is reduced. Despite this, the aqueous solubility of ICp_6 -Cu is not reduced and its aggregation also did not take place. This is mainly because of presence of water molecules in co-ordination sphere of Cu^{2+} which increase the interaction of ICp_6 -Cu with solvent molecules through hydrogen bonding and thus prevent stacking of chlorin molecules [179]. The analysis of quenching of intrinsic fluorescence of HSA by ICp_6 -Cu revealed that it binds with the protein with relatively high affinity. The value of K_b and n suggest that HSA has one high affinity binding site for ICp_6 -Cu. The pronounced quenching of Trp fluorescence by ICp_6 -Cu (fig 3.16), high probability of energy transfer and the value of Forster distances (r) between Trp-214 and ICp_6 -Cu strongly suggest the possibility of Sudlow site I as binding site for ICp_6 -Cu. In comparison, the number of binding sites for Cp_6 was more than 1 which is in agreement with previous studies by Datta et al [199]. These investigators based on site marker competition experiments had identified the binding

sites for Cp_6 as Sudlow site I and II [199, 216]. As compared to Cp_6 , the two adjacent carboxylic groups in ICp_6-Cu at C13 and C15 position are occupied by Cu^{2+} which could explain decrease in the number of binding affinity and sites of ICp_6-Cu . The binding of drug or xenobiotics on HSA can often lead to change in the conformation of the protein [217, 218]. Results on quenching of protein fluorescence by ICp_6-Cu showed that there is blue shift in the fluorescence spectrum indicating possibility of change in the conformation of the protein. Since fluorescence of protein after excitation with 280 nm arise due to emission from both Trp and Tyr, to verify any change in conformation of HSA synchronous fluorescence spectroscopy was applied. Results revealed that binding of ICp_6-Cu to HSA resulted in higher quenching of Trp fluorescence than that for Tyr without any significant shift in respective peak position (fig 3.15). Thus due to higher quenching of Trp fluorescence, the 280 nm excited fluorescence of HSA was dominated by Tyr fluorescence and hence appeared blue shifted. In synchronous spectra, it is clearly seen that ICp_6-Cu did not cause any change in the conformation of the protein. Since almost similar results were obtained for Cp_6 which binds to subdomain IIA of HSA [199], it can be concluded that there is no change in binding site of ICp_6-Cu due to insertion of copper and iodide.

HSA possess specific binding sites for transition metal ions at the N-terminal site which comprises the first three amino acid sequence (Asp-Ala-His) and the sulfhydryl groups. A secondary weaker binding site (site A) for metal ions has also been reported which comprises the side chain carbonyl of Asn99 of domain I, the imidazole of His247 and the carboxylate of Asp249, both of domain II [219]. HSA can compete with ligand for metal ion and consequently can results in trans-complexation of metal ion from the ligand to albumin under normal physiological

conditions [220-223]. In addition, such interaction can affect the stability of the metal complex under the physiological condition or lead to structural modifications and oxidation of HSA [220, 222]. However, no change in the absorption spectra of ICp_6 -Cu was observed even after prolonged incubation with HSA. This suggested that the interaction did not destabilize metal from ICp_6 -Cu.

3.3.4. Ability of ICp_6 -Cu to bind with DNA

It is generally accepted that DNA is a potential target of metal-based anticancer agents including copper complexes [150, 224]. Copper complexes have been shown to bind with DNA non-covalently either through intercalation, binding at minor or major DNA grooves or at the surface [150, 184]. Similarly, certain metal complexes of porphyrins also show strong binding with DNA via intercalation, groove binding or outside interaction [167, 225, 226]. Intercalation into DNA base pairs is usually characterized by prominent redshift (≥ 10 nm) and prominent hypochromicity ($\geq 40\%$) in the Soret absorption band of the PS [225]. In contrast, outside binding exhibits less or no redshift and lower hypochromicity in the Soret band [227]. For ICp_6 -Cu, the hypochromicity due to interaction with DNA was not very prominent ($\sim 15\%$) and there is also no shift in the position of the Soret band. These results suggest that binding mode of ICp_6 -Cu with DNA is not by intercalation. Strong binding of metal complexes with DNA is indicated by change in the electrophoretic mobility of the plasmid DNA [203, 204], but no such effect was observed with ICp_6 -Cu. Further, the binding constant for ICp_6 -Cu and metal free Cp_6 was almost same. These results suggest that insertion of copper has no significant influence on DNA binding and the mode of binding is through weak outside interactions.

3.4. Conclusion

To summarize, EPR and FTIR studies of ICp_6 -Cu suggest that copper is attached to the two adjacent carboxylic groups through coordination and the most probable site of iodination was determined to be meso position in the tetrapyrrole ring. Studies with fluorescence probes of 1O_2 and free radicals suggested that the photodynamic action of ICp_6 -Cu is mediated mainly through type I process. Because of low generation of 1O_2 , the complex is more photostable than Cp_6 . The results of serum albumin and ICp_6 -Cu binding study showed that ICp_6 -Cu binds strongly with HSA and the binding did not affect the conformation of the protein or destabilize metal from ICp_6 -Cu. The pronounced quenching of Trp-214 fluorescence and the value of Forster distances (r) between Trp-214 and ICp_6 -Cu suggest that probable binding site is same as Cp_6 , i. e. Sudlow site I at subdomain IIA. Thus strong binding of ICp_6 -Cu with HSA could play important role in its biodistribution, bioavailability and accumulation in tumor. Investigation of the interaction of ICp_6 -Cu with DNA shows moderate binding due to electrostatic interaction and suggested that ICp_6 -Cu is less likely to target DNA.

Chapter 4

Photodynamic efficacy of ICp₆-Cu in cancer cells

4.1. Introduction

Most studies of PDT are focused on PSs which can induce phototoxicity via generation of $^1\text{O}_2$ and hence it is usually considered that the $^1\text{O}_2$ is the main species responsible for PDT efficacy. For this reason, the major drawback in the PDT of solid tumors with currently available PSs is poor effectiveness to induce cytotoxicity within the hypoxic region of tumors [49, 61, 84]. Further, during PDT the formation of $^1\text{O}_2$ and damage to vasculature also results in O_2 depletion which further limits its efficacy [49]. Recent studies showed that switching the mode of action of PS from Type II to Type I can help overcome this drawback [213].

Studies in the previous chapter demonstrated that the photodynamic action of $\text{ICp}_6\text{-Cu}$ is mediated predominantly via Type I mechanism. In the present study, the efficacy of $\text{ICp}_6\text{-Cu}$ to accumulate in oral cancer cells and to induce phototoxicity under normal and reduced O_2 environment has been investigated. Since ROS generated in photosensitized reaction have small diffusion distance of few nanometers relative to the diameter of a cell ($\sim 20 \mu\text{m}$), thus, the radius of its toxic effect is limited to the site of PS accumulation. In this respect, the specific localization PS in vital organelles plays a crucial role in photodynamic killing of cancer cells [49].

The distribution of $\text{ICp}_6\text{-Cu}$ in various cell organelles was studied by confocal microscopy. PDT efficacy was assessed by determination of phototoxicity at varying concentration and the light dose. To gain insight into the mode of photodynamic action of $\text{ICp}_6\text{-Cu}$, the effect of mechanistic probes of ROS (NaN_3 , L-histidine, D-mannitol, DMSO) on phototoxicity has been studied.

4.2. Results

4.2.1. Intracellular uptake of ICp₆-Cu and Cp₆

The intracellular uptake of Cp₆ and ICp₆-Cu in 4451 and NT8e cells after 3 h of incubation is shown in table 4.1. The intracellular level of ICp₆-Cu is about 2 times higher than that of Cp₆ in both the cell lines (p < 0.05).

Table 4.1. Intracellular uptake of PSs in NT8e and 4451 cells incubated with 10 μM concentration for 3 h. Data represent mean ± SD of three independent experiments.

Cell lines	Intracellular level of PS (nM / μg of protein)	
	Cp ₆	ICp ₆ -Cu
NT8e	0.15 ± 0.07	0.34 ± 0.09
4451	0.13 ± 0.01	0.36 ± 0.05

4.2.2. Intracellular distribution of ICp₆-Cu

To find the intracellular localization site of ICp₆-Cu, the cells were treated with 10 μM ICp₆-Cu for 3 h, co-stained with fluorescence probes specific to various cell organelles and imaged by confocal microscopy. The representative images of NT8e cells are shown in fig 4.1. The red fluorescence of ICp₆-Cu is localized in the cytoplasm but not in cell nucleus (fig 4.1 a, d). The green fluorescence of lysotracker, as well as ER-tracker, is well demarcated (fig 4.1 b & e) which overlapped considerably with red fluorescence of ICp₆-Cu as indicated by yellow regions in the overlay images (fig 4.1 c & f). With Mito and Golgi specific fluorescence probes, the fluorescence of ICp₆-Cu did not show significant overlap (fig 4.2). These observations indicated that ICp₆-Cu localized mainly in lysosomes and ER.

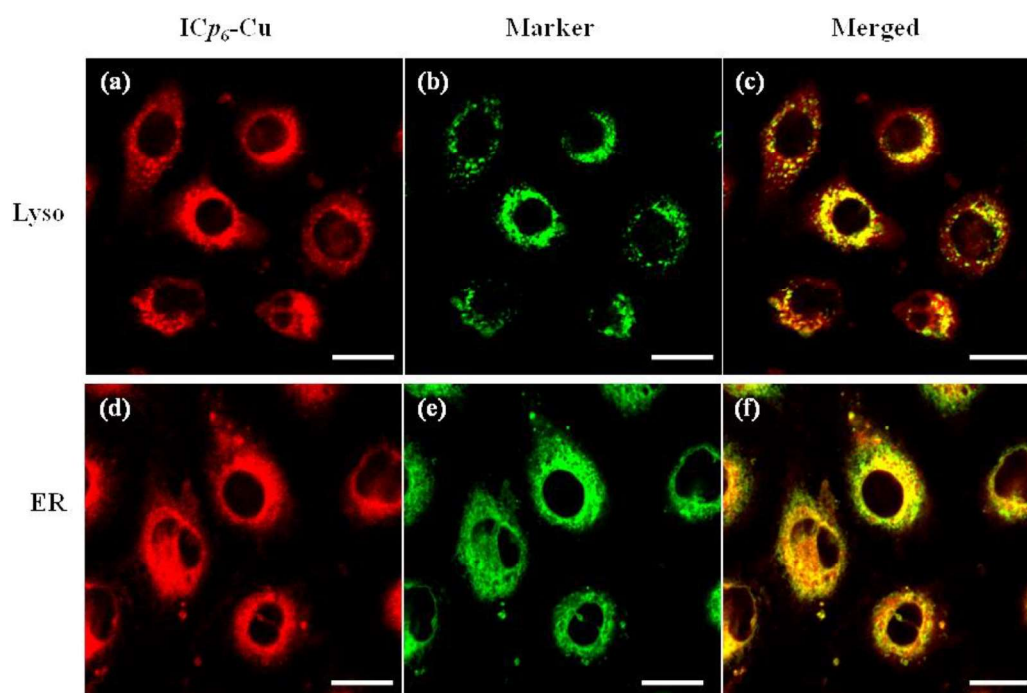


Figure 4.1. Localization of ICp₆-Cu in NT8e cells. Confocal fluorescence micrographs of NT8e cells showing red fluorescence of ICp₆-Cu (a and d) and green fluorescence of LysoTracker (b), ER-Tracker (e) and the merged image of ICp₆-Cu and the organelle probes (c and f). Experiments were repeated three times with similar results and representative images are shown. Magnification 40X, scale bar is 20 μm .

4.2.3. Phototoxicity of ICp₆-Cu in cancer cells

To assess the phototoxicity of ICp₆-Cu, the cells were treated with varying concentrations of ICp₆-Cu (2.0 μM to 15 μM) for 3 h and then irradiated with redlight at a fixed light dose. Additionally, cells were treated with 10 μM ICp₆-Cu for 3 h and then exposed to varying doses of red light. The dependence of phototoxicity of ICp₆-Cu on the concentration and the light dose in two oral cancer cell lines (4451 and NT8e) is shown in fig 4.3 a and b, respectively. Treatment of cells with various concentration of ICp₆-Cu followed by light exposure at a fixed light dose of 7.0 J/cm² led to concentration-dependent increase in phototoxicity (fig 4.3 a). At 10 μM ICp₆-Cu, the phototoxicity was \sim 80% which increased further upto \sim 95% at higher

concentrations. However, there was also some (~ 10%) dark toxicity in both cell lines beyond 10 μM $\text{ICp}_6\text{-Cu}$. Based on this, 10 μM concentration of $\text{ICp}_6\text{-Cu}$ was selected to study the dependence of phototoxicity on light dose. As shown in fig 4.3 b, PDT with 10 μM $\text{ICp}_6\text{-Cu}$ led to a dose-dependent increase in phototoxicity. The phototoxicity was ~ 60% at the light dose of 5 J/cm^2 and increased to ~90% at 12.0 J/cm^2 .

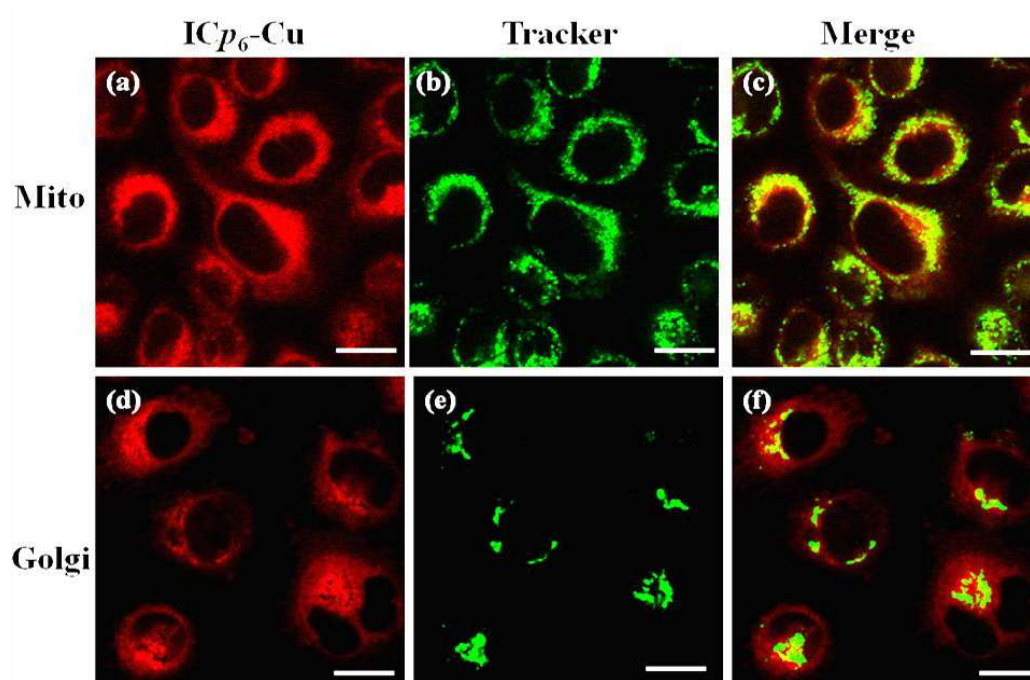


Figure 4.2. Localization of $\text{ICp}_6\text{-Cu}$ in NT8e cells. Confocal fluorescence micrographs of NT8e cells showing red fluorescence of $\text{ICp}_6\text{-Cu}$ (a and d) and green fluorescence of MitoTracker (b), Golgi Tracker (e) and the merged image of $\text{ICp}_6\text{-Cu}$ and the organelle probes (c and f). Experiments were repeated three times with similar results and representative images are shown. Magnification 40X, scale bar is 20 μm .

4.2.4. $\text{ICp}_6\text{-Cu}$ induced morphological changes

The change in cell morphology after PDT is shown in fig 4.4. The cells in control appear healthy with intact cell membrane (fig 4.4 a and c). At 3 h after PDT (LD_{80}

dose), almost all NT8e cells showed the formation of membrane blebs whereas, 4451 cells

cells

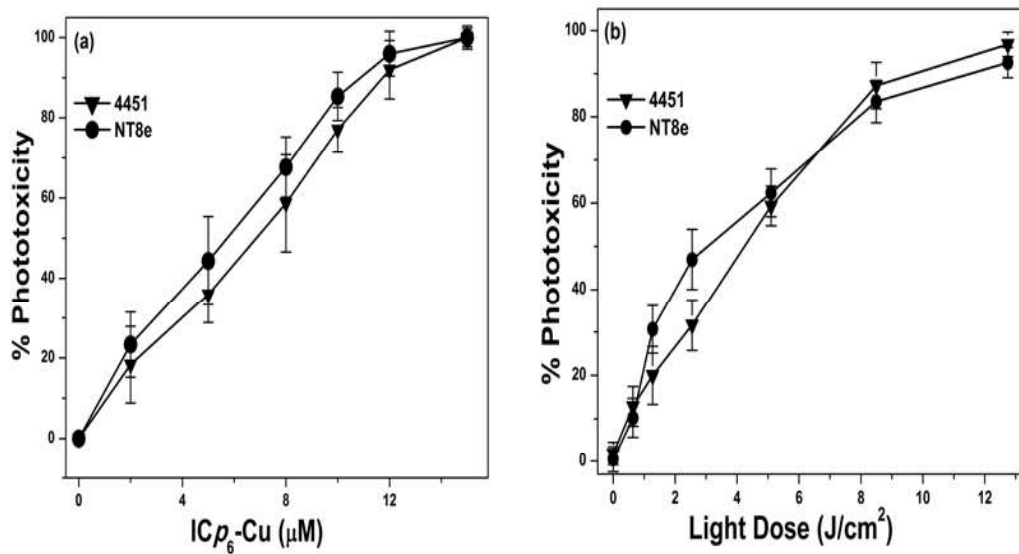


Figure 4.3. (a) Concentration-dependent phototoxicity of ICp_6-Cu in NT8e and 4451 at a fixed light dose of $7 J/cm^2$. (B) Phototoxicity of ICp_6-Cu in NT8e and 4451 cell lines as a function of light dose.

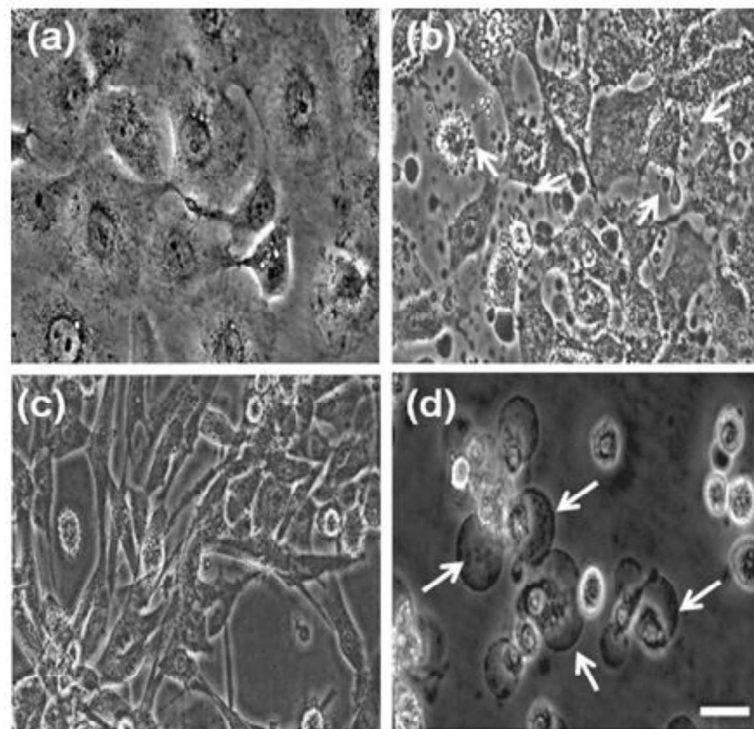


Figure 4.4. Microphotographs of NT8e and 4451 cells in control (a, c) and at 3 h after PDT (b, d) showing cell morphology in phase contrast, magnification 20X, scale bar – $20 \mu m$. Arrows showing the formation of apoptotic blebs in NT8e (b), and plasma membrane damage and swelling in 4451 (d).

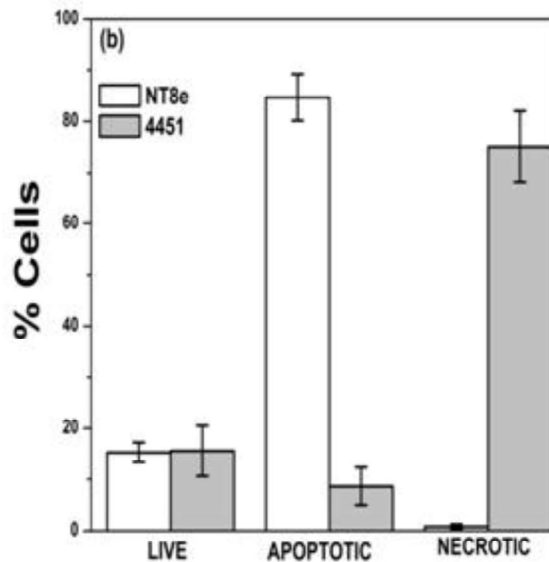
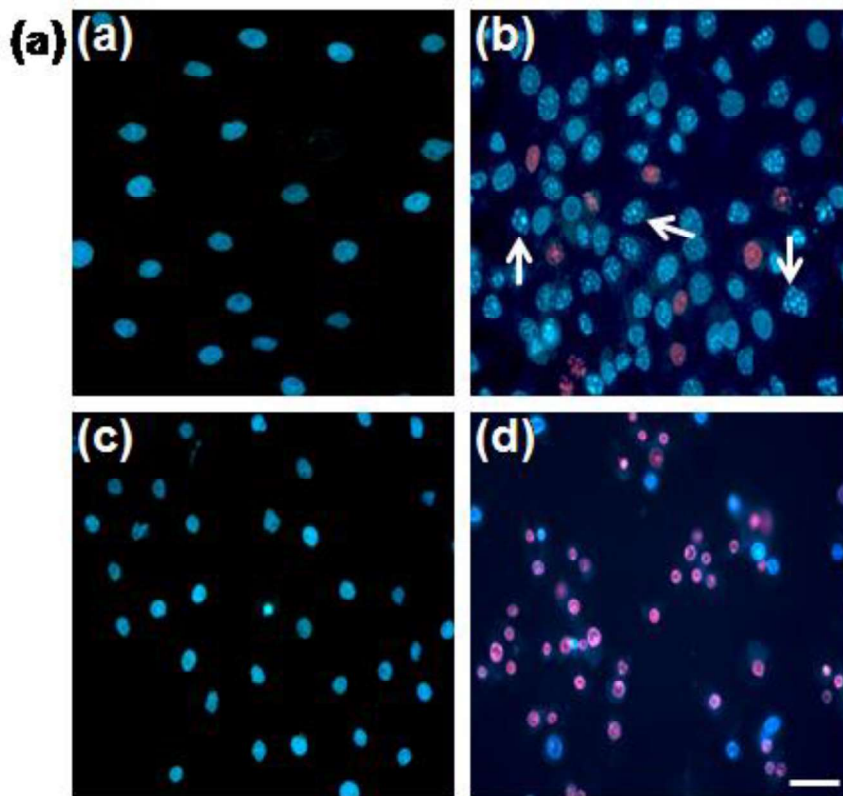


Figure 4.5. (a) Fluorescence microphotographs of NT8e (a, b) and 4451 (c, d) cells in control (a, c) and at 3 h after PDT (b, d) with light dose of 8 J/cm^2 , showing apoptotic and necrotic cells after staining with HO-PI fluorescent dyes, magnification 20 X, scale bar – $20 \mu\text{m}$. Arrows showing bright blue fluorescence of condensed DNA in NT8e. (b) Percentage of live, apoptotic and necrotic cells at 3 h after PDT in NT8e and 4451 cell lines.

display damaged plasma membrane and swelling, indicated by arrows (fig 4.4 b and d). Apoptotic and necrotic cells stained with PI- HO are shown in fig 4.5 a. The percentages of live, apoptotic and necrotic cells in control and PDT treated cells for the two cell lines is shown in fig 4.5 b. it is evident from the results that the mode of cell death in NT8e and 4451 cells occurred mainly via apoptosis and necrosis, respectively.

4.2.5. Effect of ROS quenchers on ICp₆-Cu induced phototoxicity

The influence of quenchers of ¹O₂ (NaN₃, L- histidine) and free radicals (DMSO, D-mannitol) on ICp₆-Cu induced phototoxicity is shown in fig 4.6. As compared to control, the level of phototoxicity is significantly reduced in the presence of all the quenchers. Treatment of cells with quenchers alone under similar conditions did not result in any toxicity.

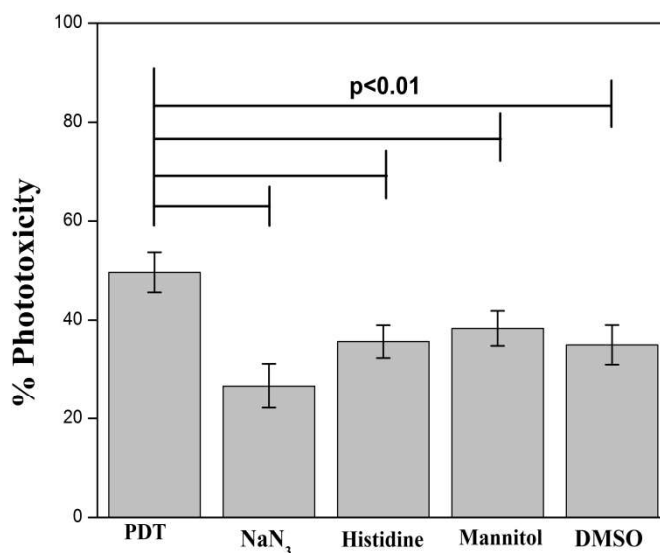


Figure 4.6. Percent phototoxicity induced by ICp₆-Cu in NT8e cells in absence and presence of quenchers of ROS. The cells were subjected to PDT using the light dose of 4 J/ cm² which led to ~50% phototoxicity in absence of any quencher. Data are mean ± SD of three independent experiments in triplicates.

4.2.6. Phototoxicity under hypoxic conditions

The effect of hypoxia on the phototoxicity of ICp_6 -Cu and Cp_6 at LD_{50} and LD_{80} dose (for normoxic condition) is shown in fig 4.7. For Cp_6 , hypoxia led to decrease in phototoxicity by almost 1/2 (~30% and 40%). In contrast, phototoxicity induced by ICp_6 -Cu under normoxic and hypoxic condition show no significant difference. Thus, as compared to Cp_6 , ICp_6 -Cu led to higher phototoxicity under hypoxic condition.

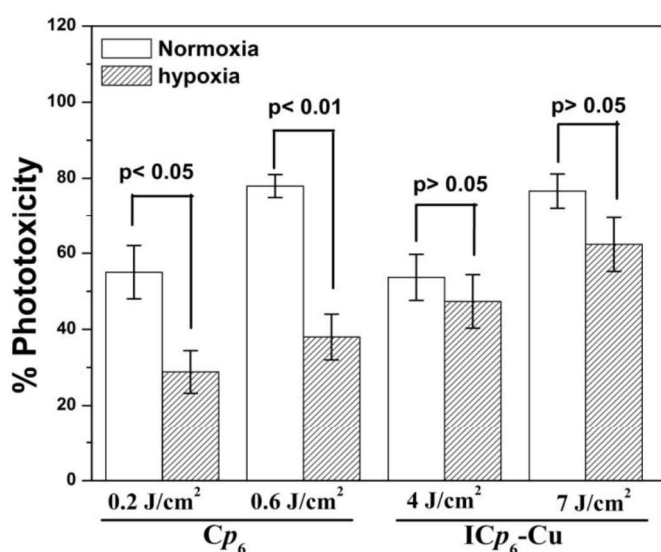


Figure 4.7. Percent phototoxicity of ICp_6 -Cu and Cp_6 in NT8e cells after PDT under normoxia and hypoxia. The light dose used corresponds to LD_{50} and LD_{80} for cells under normoxic condition. Data are mean \pm SD of three independent experiments in triplicates.

4.3. Discussion

Results of this study showed that ICp_6 -Cu accumulated more efficiently in cancer cells than the parent Cp_6 and led to strong phototoxicity in concentration and light dose-dependent manner. The higher cellular uptake of ICp_6 -Cu in comparison to Cp_6 can be attributed to decrease in net negative charge and increase in its hydrophobicity due to coordination of carboxylic groups with Cu^{2+} , as shown in the previous chapter. More

lipophilic PS interacts and localizes better in cellular membranes as a result increased lipophilicity generally contributes to higher cellular uptake [49,228]. Here it is important to mention that the cellular uptake and intracellular localization of PS depend considerably on both charge and amphiphilicity because both these factors determine the interaction of PS with cellular membranes. Due to an overall negative charge of cellular membranes, the negatively charged PSs cannot freely diffuse across the membrane. Generally, anionic PS binds with albumin and taken up by cells either by passive diffusion or by non-specific endocytosis and gets accumulated in ER, Golgi or lysosomes [49, 228, 229]. In agreement with this studies on intracellular localization of Cp_6 in glioma cells have shown that it localizes in endoplasmic reticulum and Golgi apparatus but not in mitochondria [230]. Results of colocalization studies revealed that ICp_6 -Cu accumulated in ER and lysosomes but not in Golgi and mitochondria (fig 4.1 and 4.2). This difference can be explained due to the difference in the hydrophobicity of ICp_6 -Cu and Cp_6 . It is well known that more hydrophobic PS binds with low-density lipoproteins and accumulates in endosomes and lysosomes via receptor-mediated endocytosis. In contrast, more hydrophilic photosensitizers mostly bind with albumin and accumulate in ER, Golgi or lysosome by passive diffusion or by non-specific endocytosis [49, 228, 229]. Moreover, it is generally accepted that positively charged PSs through interaction with negatively charged components of the membrane are taken up more efficiently by cells and generally accumulates in mitochondrial membranes [49, 228, 229]. The absence of localization of ICp_6 -Cu in mitochondria despite having cationic charge at Cu^{2+} is probably because of the presence of water molecules in the coordination sphere of Cu^{2+} which prevent its direct interaction with cellular membranes.

The localization of PS in various cell organelles has an important role in cell death mechanism [49, 61]. Depending on the specific localization of PS in particular cell organelle PDT can lead to cell death via apoptosis, necrosis or autophagy [49, 61]. However, in most cases, PS that localizes in multiple sites and leads to damage of several molecular targets at the same time, triggers a complex signaling between the cell organelles. Consequently, the cell death mechanisms are largely determined by the severity of damage and the genetic factors [49, 61]. The observations on the cellular and nuclear morphology of cells subjected to PDT suggested that ICp_6 -Cu induced apoptotic and necrotic cell death in NT8e and 4451 respectively. This is because the tumor suppressor p53 gene responsible for apoptotic death is wild type in NT8e cells whereas it is mutated in 4451 cells [231, 232]. These results are consistent with our earlier report on the mode of cell death induced by Cp_6 and its histamine conjugate in these cell lines [147].

Since ICp_6 -Cu in cell-free system demonstrated photodynamic action is mainly via type I mechanism, it was of interest to find out whether phototoxicity induced by ICp_6 -Cu in cancer cells is also mediated through the same mechanism. Interestingly, studies on phototoxicity in the presence of quenchers of 1O_2 (NaN_3 , histidine) and other ROS (DMSO, mannitol) revealed that the phototoxicity of ICp_6 -Cu was significantly reduced in presence of all these quenchers suggesting the involvement of both type I and type II ROS. It is important to mention that both NaN_3 and histidine can also quench $\bullet OH$ radicals [233]. If that occurs then both NaN_3 and histidine should lead to inhibition of phototoxicity to the same extent because their rate constant for reaction with $\bullet OH$ radicals is almost same [233]. However, the inhibition of phototoxicity in presence of NaN_3 was higher than that for histidine (fig 4.6). This

correlated with their efficiency to quench $^1\text{O}_2$ [233]. The contribution of $^1\text{O}_2$ to the phototoxicity of $\text{ICp}_6\text{-Cu}$ was not expected because studies on ROS generation in aqueous solution showed that the $^1\text{O}_2$ generation ability of $\text{ICp}_6\text{-Cu}$ is very low (chapter 3, fig 3.8 and 3.9). Here it is pertinent to note that the efficacy of PSs to generate $^1\text{O}_2$ also depends on its environment. In aqueous solution, hydrophilic PSs usually tend to aggregate and show a decrease in $^1\text{O}_2$ generation efficiency whereas the localization of PS in cellular membrane results in dis-aggregation and increase in photosensitization via type II process [46, 47]. $\text{ICp}_6\text{-Cu}$ is more hydrophobic than Cp_6 , as revealed by their octanol: water partition coefficient (chapter 3), hence it is likely to localize efficiently in the cellular membrane [234, 235]. Further, the lifetime of $^1\text{O}_2$ in the cellular environment is considerably longer (10 μs) as compared to that in aqueous media (3.5 μs) [61]. This explains the contribution of $^1\text{O}_2$ to the phototoxicity for $\text{ICp}_6\text{-Cu}$.

PDT efficacy of majority of PSs depends strongly on the availability of O_2 and hence PDT often fails to produce the desirable outcome in case of hypoxic solid tumors [236-238]. Alternatively, studies on PDT of human tumor xenografts with mTHPC (5,10,15,20-tetrakis(meso-hydroxyphenyl) porphyrin) have shown that photochemical process leading to radical formation can work better under hypoxic condition [86]. The results on phototoxicity of $\text{ICp}_6\text{-Cu}$ in normoxic and hypoxic conditions revealed that its photodynamic efficacy is not significantly affected even under low O_2 environment. This is consistent with the ability of $\text{ICp}_6\text{-Cu}$ to induce phototoxicity via Type I mechanism. Several recent studies have also reported that PS which acts via type I photochemical mechanism induce better PDT efficacy under hypoxia. For example, phototoxicity mediated by methylene blue encapsulated in

polymer nanoparticle [212] and mTHPC incorporated in electron-rich poly(2-(diisopropylamino)ethyl methacrylate) micelles is not affected under hypoxia [213]. Similarly, photodynamic release of doxorubicin induced by chondroitin sulfate conjugated Pheophorbide-a via type I mechanism led to higher toxicity under hypoxic conditions than that under normoxic conditions [214]. Thus, the ability of ICp_6 -Cu to act via type I process and induce phototoxicity under hypoxic conditions may provide a significant advantage for PDT of solid tumors.

4.4. Conclusions

To summarize, the results of the studies on cellular uptake and phototoxicity of ICp_6 -Cu showed that ICp_6 -Cu accumulate more efficiently in cancer cells than Cp_6 and apart from ER, it also localized in lysosomes, which is attributed to its higher hydrophobicity. Further, ICp_6 -Cu showed potent phototoxicity in cancer cells and the phototoxic efficacy is not affected even under hypoxic condition. Therefore, it can be concluded that ICp_6 -Cu is a promising PS for PDT of cancer.

Chapter 5

Radiosensitization efficacy of ICp₆-Cu in combination with synchrotron X-ray radiation

5.1. Introduction

PDT has the ability to treat superficial tumors selectively by exploiting the preferential accumulation of PS in tumor and application of light, confined to diseased tissue. However, due to the limited penetration depth of light in tissue, PDT is not very effective for the treatment of tumors located in deep tissue. Recently, a novel therapeutic approach that utilizes X-ray radiation to activate PS directly or indirectly through absorption of X-ray energy by high Z element, has gained considerable attention [93-95, 145]. One such approach requires activation of PS indirectly via X-ray induced luminescence of metal nanoparticles or a lanthanide atom such as europium, terbium, placed in close vicinity of the PS [239]. The efficacy of this approach depends on several factors such as effective energy transfer between PS and scintillating material, cellular uptake of the conjugate, and most importantly on Φ_{Δ} which in deeper tumor region will be limited by hypoxic conditions [141, 240, 241]. Alternatively, a therapeutic approach based on direct X-ray photoactivation of metal conjugated PS can be more suitable for the treatment of deep-seated tumors because it induces cytotoxicity via generation of Auger electrons, photoelectrons and free radicals [37], which is less likely to be affected by hypoxia.

The focus of the present study was to investigate the efficacy of ICp_6-Cu for X-ray photoactivation induced cytotoxicity in human oral cancer cell lines. The presence of copper and iodine in ICp_6-Cu make it suitable for X-ray photoactivation using X-ray energy of > 8.9 keV or > 33.2 keV respectively. The effects of synchrotron X-ray radiation (8- 10 keV) without and with ICp_6-Cu treatment on cell viability and colony forming ability of cancer cells were examined. Studies on cellular ROS levels, DNA

damage and cell cycle progression were performed to understand the mode of ICp₆-Cu induced radio-sensitization.

5.2. Results

5.2.1. Intracellular uptake of ICp₆-Cu

As shown in fig 5.1, both NT8e and 4451 cells accumulated significant amount of ICp₆-Cu after 3 h incubation. The cellular level of ICp₆-Cu was found to increase with concentration and as compared to NT8e cells, 4451 cells showed significantly higher accumulation of ICp₆-Cu at 20 μ M and 30 μ M ($p < 0.05$). However, at 10 μ M ICp₆-Cu concentration the level of uptake is not significantly different between two cell lines.

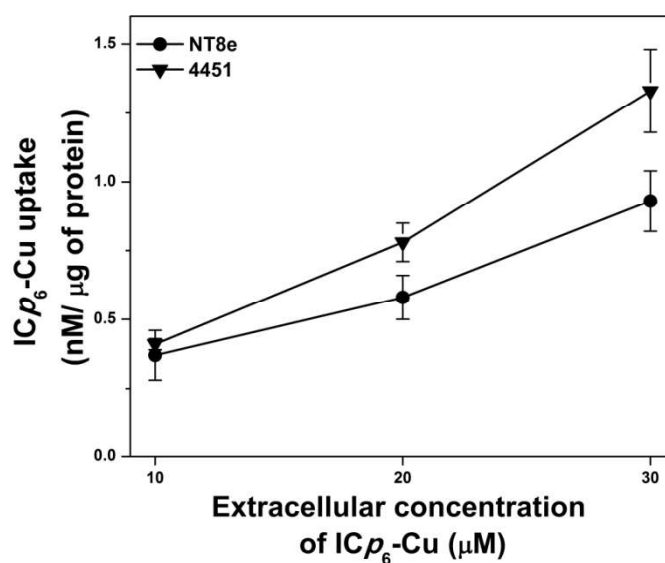


Figure 5.1. Intracellular uptake of ICp₆-Cu as a function of concentration in NT8e and 4451 cells. Data are represented as mean \pm SD obtained from three independent experiments.

5.2.2. ICp₆-Cu pretreatment enhances X-ray induced cytotoxicity

The effect of ICp₆-Cu pre-treatment (3 h at 10 μ M, 20 μ M and 30 μ M) on X-ray induced cytotoxicity in NT8e and 4451 cells is shown in fig 5.2. In both the cell lines, X-ray irradiation led to dose-dependent decrease in cell viability wherein, \sim 50% and

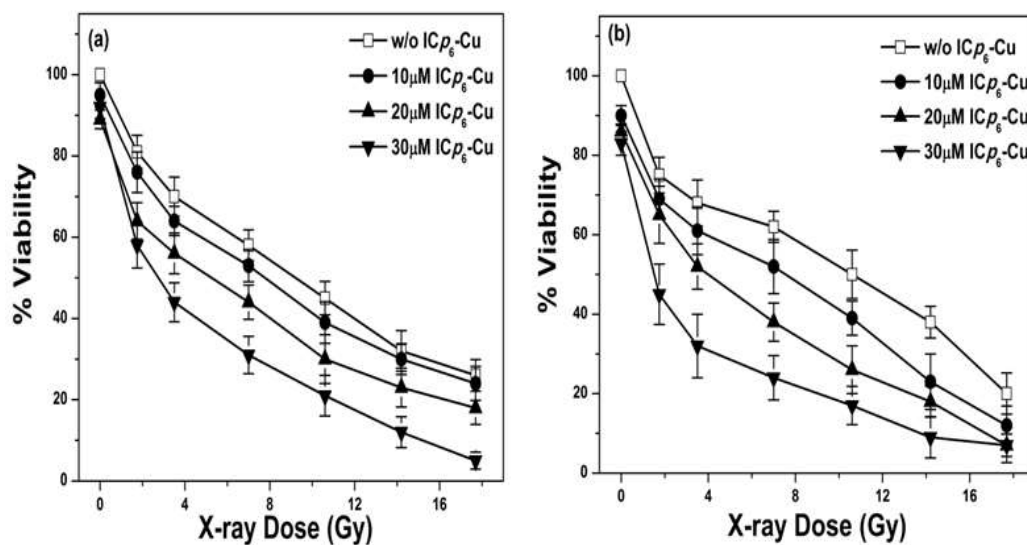


Figure 5.2. Cytotoxic effects of X-ray without and with ICp₆-Cu pretreatment in oral cancer cells determined by MTT assay. Changes in percent cell viability in NT8e (a) and 4451 (b) cells as a function of X-ray dose, the cells were pretreated with 10, 20 and 30 μM ICp₆-Cu for 3 h. Percent cell viability was calculated with respect to a control sample (without ICp₆-Cu treatment). Each data point represents mean ± SD obtained from three independent experiments

90% cytotoxicity was observed at about ~10 Gy and ~17 Gy, respectively. In 4451 cells, pre-treatment with 10 μM ICp₆-Cu led to significant increase in X-ray induced cytotoxicity at X-ray dose ≥ 7.0 Gy (fig 5.2 b). Whereas in NT8e cells, pre-treatment with 10 μM ICp₆-Cu did not lead to any significant increase in X-ray induced cytotoxicity at any dose (fig 5.2 a). At 20 μM, ICp₆-Cu led to significant increase in X-ray induced cytotoxicity (p< 0.05) in both the cell lines and the magnitude of effect was observed to increase further with an increase in the concentration of ICp₆-Cu. At 7 Gy X-ray dose, the loss of cell viability in 4451 cell was ~38 % which increased to ~48%, ~64% and ~78% in cells pretreated with 10 μM, 20 μM and 30 μM ICp₆-Cu, respectively. In NT8e cells, a similar concentration-dependent increase in X-ray induced cytotoxicity was seen but the magnitude of effect was significantly lower (p< 0.05) than that for 4451 cells (fig 5.2 a). At 7 Gy X-ray dose, the loss of cell viability

in NT8e cells was ~42 % which increased to ~47 %, ~56 % and ~67 % in cells pretreated with 10, 20 and 30 μM $\text{ICp}_6\text{-Cu}$, respectively.

5.2.3. X-ray dose enhancement effect by $\text{ICp}_6\text{-Cu}$

The effect of X-ray alone (7 Gy) and $\text{ICp}_6\text{-Cu}$ plus X-ray treatment on percent cell survival of NT8e and 4451 cells is shown in fig 5.3 a. As compared to X-ray alone, $\text{ICp}_6\text{-Cu}$ plus X-ray treated cells show a greater decrease in the surviving fraction and the magnitude of effect increased further with an increase in the concentration of $\text{ICp}_6\text{-Cu}$ (fig 5.3 a).

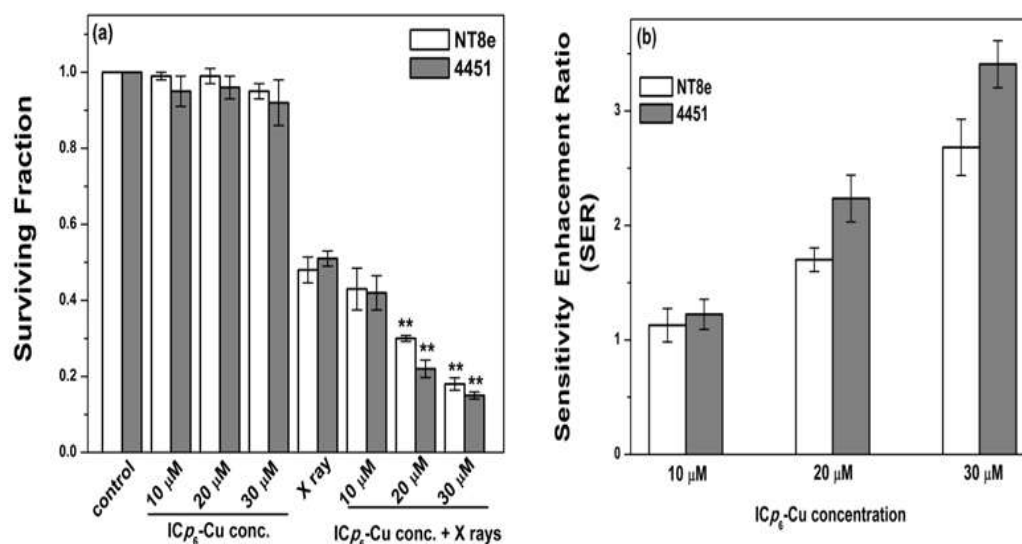


Figure 5.3. Radio-sensitization effect of $\text{ICp}_6\text{-Cu}$ in oral cancer cells determined by clonogenic assay. (a) Surviving fraction and (b) Sensitivity enhancement Ratio (SER) in NT8e and 4451. The cells were treated with $\text{ICp}_6\text{-Cu}$ (10, 20 and 30 μM) for 3 h and then irradiated with X-ray at a fixed dose of 7 Gy. ** = (p -value < 0.01) indicates significant difference between X-ray alone and combined $\text{ICp}_6\text{-Cu}$ and X-ray treatment. Data are mean \pm SD obtained from three independent experiments.

The SER obtained from the cell survival data for NT8e cells was ~1.0, 1.8 and 2.5 at 10 μM , 20 μM and 30 μM $\text{ICp}_6\text{-Cu}$, respectively (fig 5.3 b). Consistent with MTT assay, the radio-sensitization effect of $\text{ICp}_6\text{-Cu}$ was more pronounced in 4451 cells

than that for NT8e cells. SER values for 4451 cells were ~1.0, 2.3 and 3.2 at 10 μM , 20 μM and 30 μM $\text{ICp}_6\text{-Cu}$, respectively. At 20 and 30 μM , the values of SER for 4451 cells are significantly higher than that for NT8e cells ($p < 0.05$).

5.2.4. Enhancement in X-ray induced ROS formation by $\text{ICp}_6\text{-Cu}$

The effect of X-ray irradiation on the relative level of ROS in 4451 and NT8e cells without and with $\text{ICp}_6\text{-Cu}$ pre-treatment is shown in fig 5.4. Results show that as compared to control, X-ray irradiation alone led to an only marginal increase in the level of intracellular level of ROS ($p < 0.05$) in both the cell lines. In cells subjected to $\text{ICp}_6\text{-Cu}$ pre-treatment (20 μM and 30 μM) plus X-ray, the level of ROS increased significantly relative to the X-ray alone. Here also, the ROS generation in 4451 is significantly higher ($p < 0.05$) than NT8e cells at 20 μM and 30 μM $\text{ICp}_6\text{-Cu}$, which is consistent with higher radiosensitization effect of $\text{ICp}_6\text{-Cu}$ in these cells. These results correlated with the enhancement in X-ray induced cytotoxicity and support radiosensitization efficacy of $\text{ICp}_6\text{-Cu}$.

5.2.5. DNA damage induction and repair

Formation of DNA double-strand breaks (DSBs) and its repair play a significant role in X-ray induced cytotoxicity. $\gamma\text{-H2AX}$, a DNA damage sensing protein is the most reliable marker for radiation-induced DNA damage [173]. The microphotographs of 4451 and NT8e cells showing the presence of $\gamma\text{-H2AX}$ foci at 30 min, 2 h and 24 h after X-ray (7 Gy) irradiation are presented in fig 5.5 a and b. As expected, cells in control and $\text{ICp}_6\text{-Cu}$ treatment did not show $\gamma\text{-H2AX}$ foci. In contrast, cells irradiated with X-ray either without or with $\text{ICp}_6\text{-Cu}$ pre-treatment displayed a large number of $\gamma\text{-H2AX}$ foci within 30 min after irradiation. At this time, the number of $\gamma\text{-H2AX}$ foci

in X-ray alone and ICp₆-Cu plus X-ray irradiated cells was almost equal (fig 5.5 b) indicating that pre-treatment with ICp₆-Cu did not affect X-ray induced DNA damage. At 2 h and 24 h post-irradiation, the number of γ -H2AX foci in X-ray irradiated cells declined to ~40% and ~15%, respectively indicating repair of DSBs (fig 5.6 a and b). Whereas in cells treated with ICp₆-Cu plus X-ray irradiation, the number of γ -H2AX foci decreased to a lesser extent by ~60% at 2 h and thereafter no significant decrease was observed (fig 5.6 a & b). These results showed that DNA repair is impaired due to combined treatment. Moreover, the number of γ -H2AX foci at 24 h after combined treatment was higher in 4451 cells than that for NT8e cells (fig 5.6) which was consistent with higher radiosensitivity of 4451 cells.

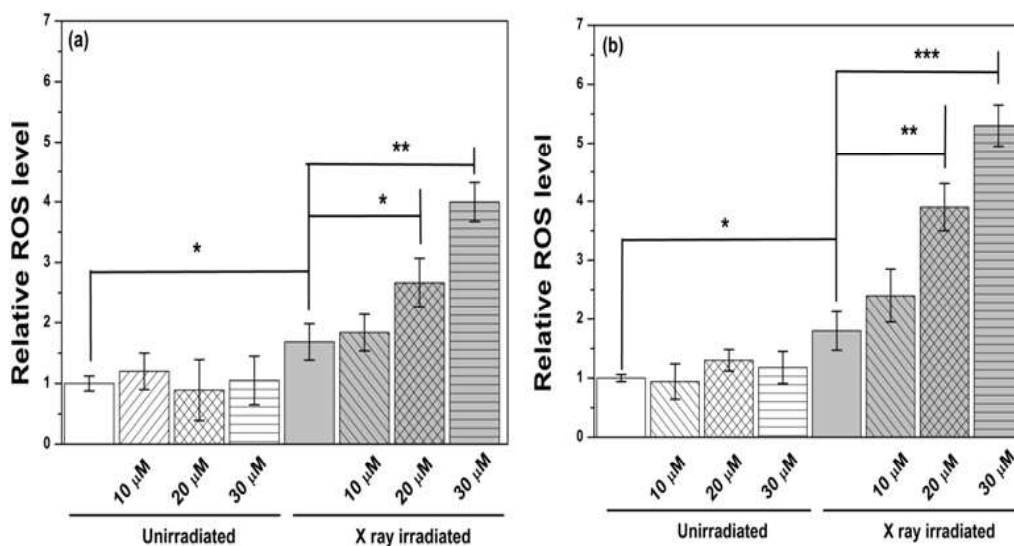


Figure 5.4. Effects of ICp₆-Cu and X-ray irradiation on ROS generation. Relative levels of ROS after X-ray irradiation (7 Gy), in NT8e (a) and 4451 (b) without or with ICp₆-Cu pretreatment. Data are mean \pm SD obtained from three independent experiments. * = ($P < 0.05$), ** = ($P < 0.01$), *** = ($P < 0.005$), indicates statistical significance.

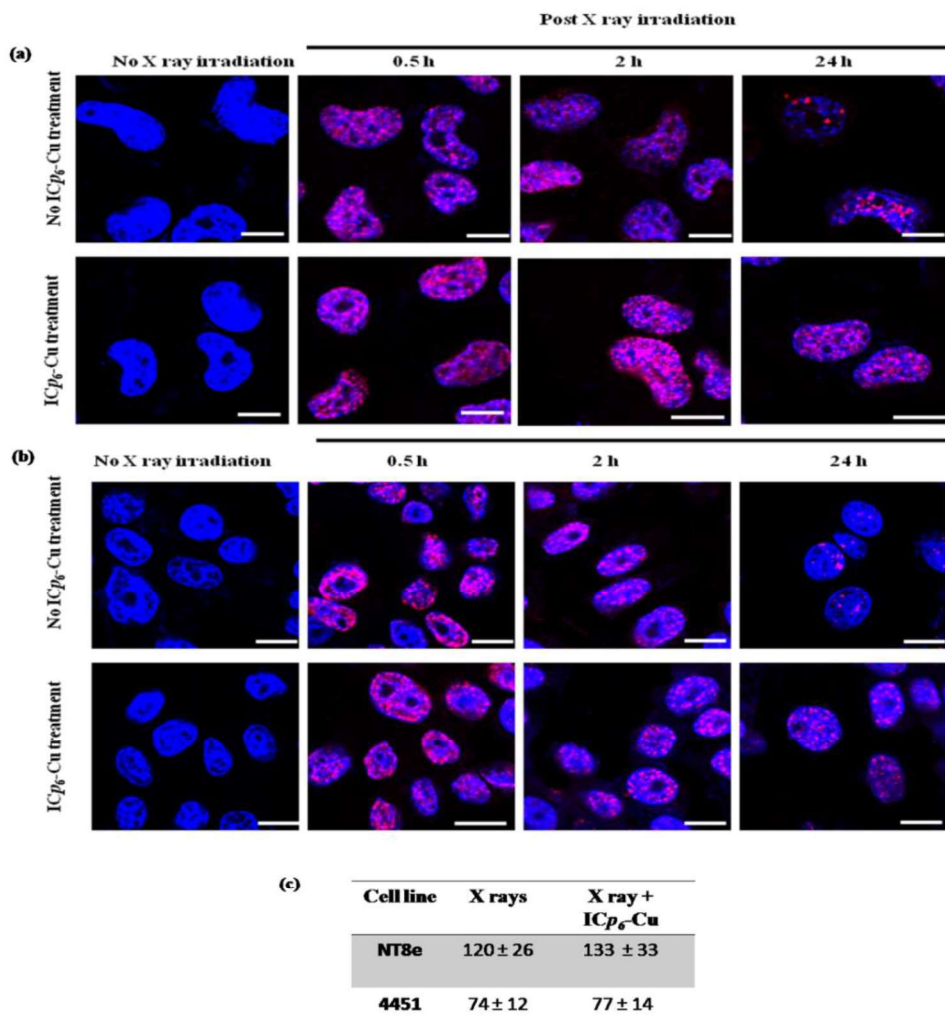


Figure 5.5. Effect of IC_{p6}-Cu and X-ray irradiation on DNA damage determined by γ -H2AX immunostaining. Representative immunofluorescence images of NT8e (a) and 4451 (b) cells treated without (upper panel) or with (lower panel) 30 μ M IC_{p6}-Cu at various time points post-irradiation (7 Gy). Images show cell nuclei in blue and γ -H2AX foci in red. (c) Number of γ -H2AX foci at 30 min post-irradiation (7 Gy) in NT8e and 4451 cells without or with IC_{p6}-Cu treatment (30 μ M).

5.2.6. Radiation-induced cell organelle damage

Since IC_{p6}-Cu localized in lysosomes and ER, the possibility of damage to these vital organelles was studied by confocal fluorescence microscopy. In fig 5.7, the microphotograph of NT8e cells in control, IC_{p6}-Cu alone, X-ray irradiated and IC_{p6}-Cu plus X-ray irradiated cells are shown. In control, IC_{p6}-Cu alone and X-ray

irradiation, lysosomes are intact as indicated by well-demarcated punctuate fluorescence (fig 5.7 (a) a, b and c), whereas, in cells that received combined treatment the fluorescence of lysotracker was diffuse and less intense indicating disintegration of lysosomes (fig 5.7 d). X-ray irradiation alone or ICp₆-Cu plus X-ray led to no significant change in ER structure (fig 5.7 (b)).

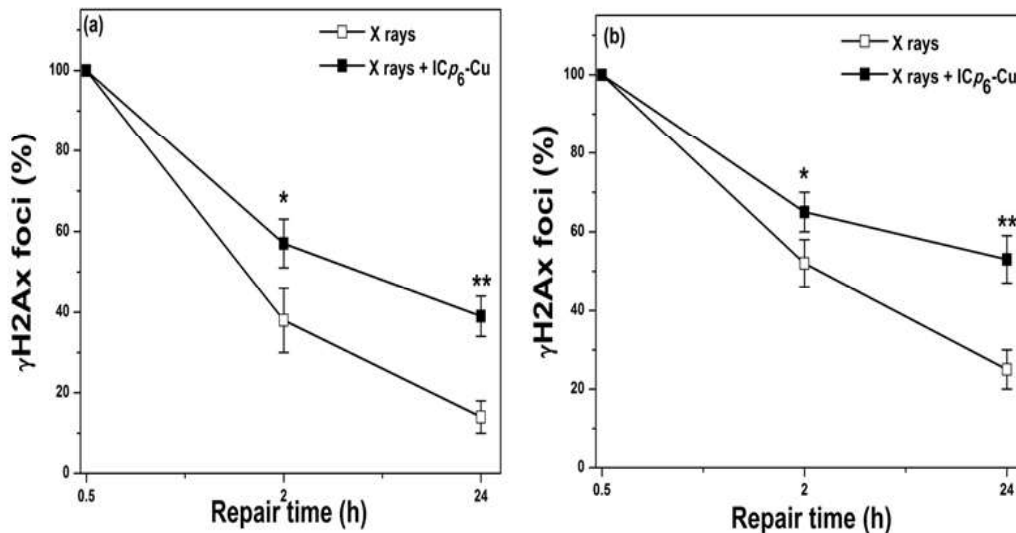


Figure 5.6. Changes in the percentage of γ -H2AX foci in NT8e (a) and 4451 (b) cells treated with or without 30 μ M ICp₆-Cu at different time periods post-irradiation (7 Gy), indicating repair kinetics of DSBs. Data represent mean \pm SD obtained from three independent experiments. * = ($P < 0.05$), ** = ($P < 0.01$) indicates statistical significance between X-ray alone and ICp₆-Cu plus X-ray treatment.

5.2.7. Cell cycle distribution and induction of cell death

Fig 5.8 shows the effect of X-ray irradiation without and with ICp₆-Cu treatment on the cell cycle distribution in NT8e and 4451 cells. As compared to the control, ICp₆-Cu treatment alone showed no effect on the cell cycle. X-ray alone and X-ray in combination with ICp₆-Cu treatment led to no change in the fraction of cells in S and G2/M which suggested that these treatments have no effect on cell cycle distribution i.e. no cell cycle arrest. In addition, results also revealed that as compared to X-ray

alone, the combined treatment led to significant increase in sub G1 population ($p < 0.05$) (fig 5.8 b and c), which mainly corresponds to apoptotic cells [174].

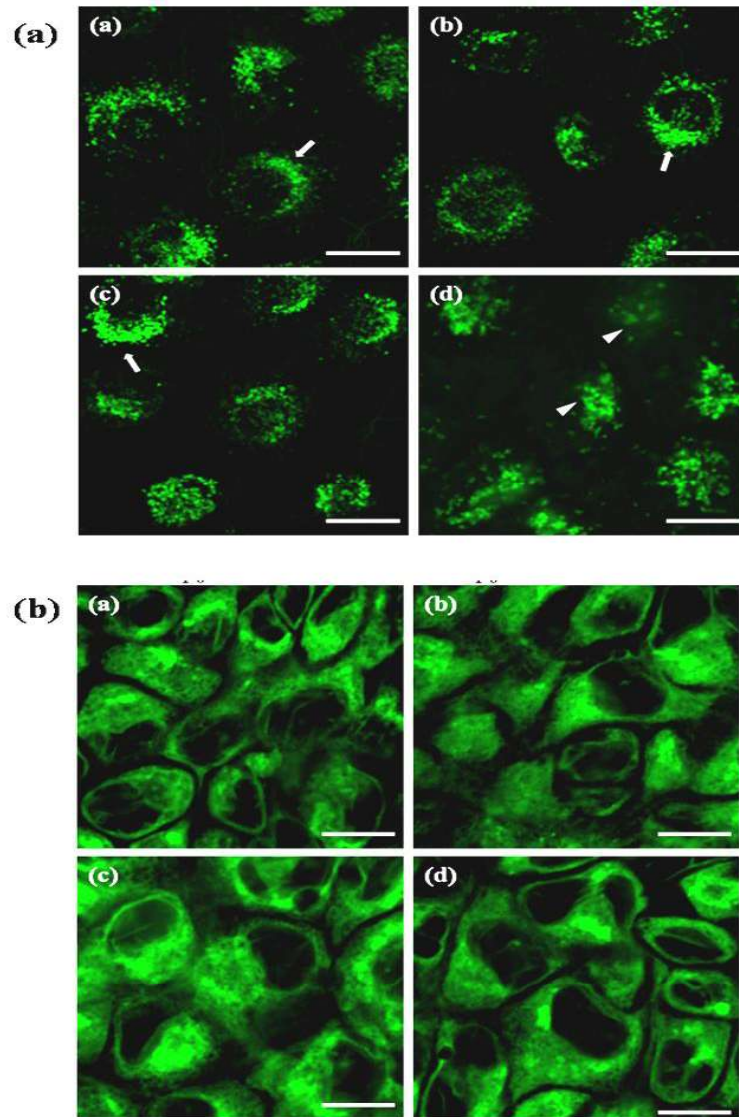


Figure 5.7. Confocal fluorescence micrographs of NT8e cells showing the effect of ICp₆-Cu induced radiosensitization on the integrity of lysosomes (a) and ER (b). Cells were stained with lysosome and ER-specific LysoTracker and ER-tracker probes. (a) Control, (b) ICp₆-Cu (30 μM) treatment alone, (c) X-ray (7 Gy) treatment alone and (d) ICp₆-Cu (30 μM) plus X-ray (7 Gy) treatment. Experiments were repeated three times and representative images are shown. Arrows indicate intact lysosome, arrowheads indicate weak disintegrated lysosomes. Magnification 40X, scale bar 20 μm.

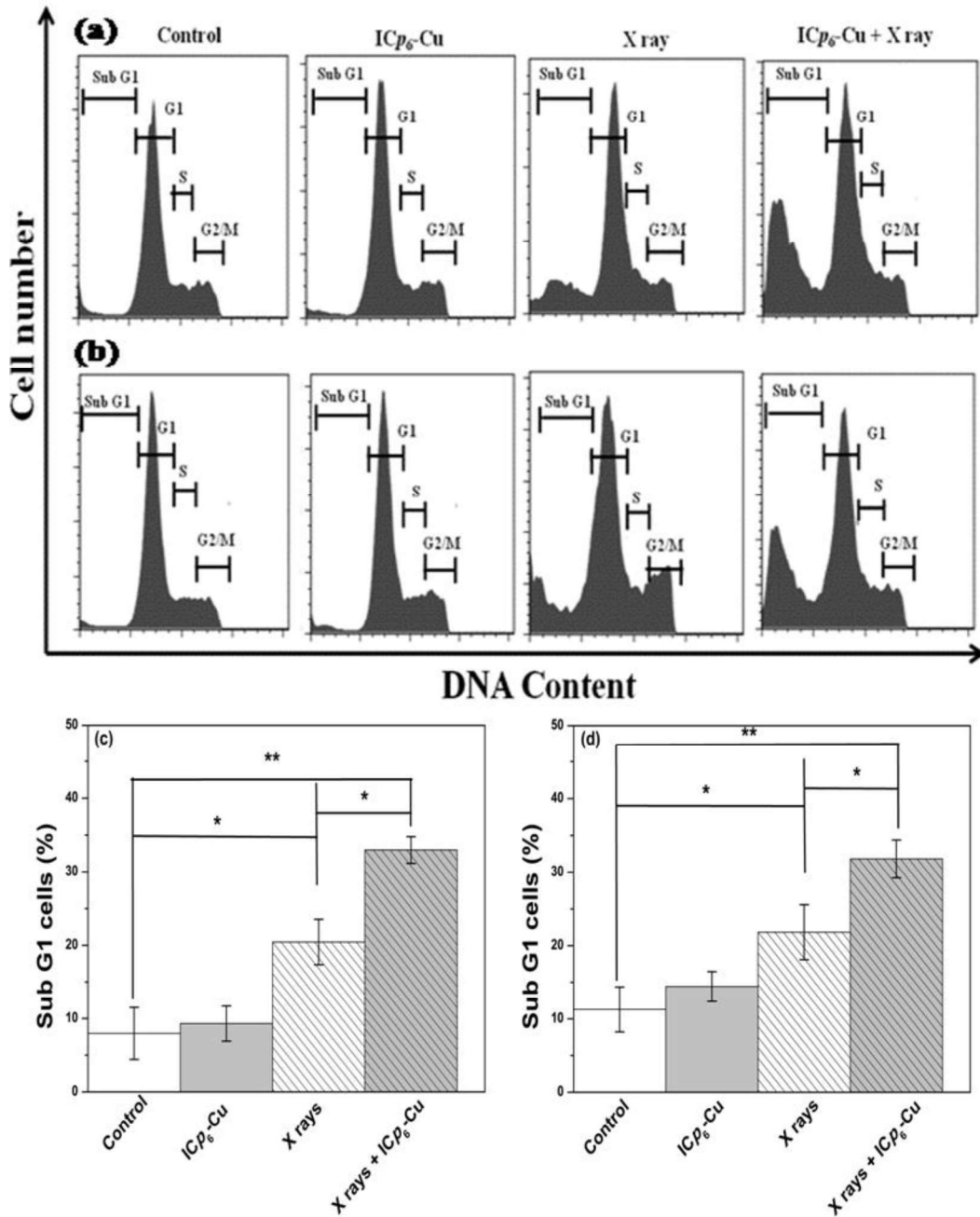


Figure 5.8. Effect of ICp₆-Cu and X-rays irradiation on cell cycle distribution in NT8e and 4451 at 24 h post-irradiation. Cell cycle histograms of NT8e (a) and 4451 (b) cells. Percentage of NT8e (c) and 4451 (d) cells in sub-G1-phase, for control, ICp₆-Cu treatment alone, X-ray irradiation alone and ICp₆-Cu plus X-ray treatment. The cells were treated with 30 μ M ICp₆-Cu for 3 h and then irradiated with X-ray at a fixed dose of 7 Gy. Data represent mean \pm SD of data obtained from three independent experiments. * = ($P < 0.05$), ** = ($P < 0.01$), *** = ($P < 0.005$) indicates statistical significance between X-ray alone and ICp₆-Cu plus X-ray treatment.

5.3. Discussion

Results of this study demonstrated that ICp_6 -Cu induced strong radio-sensitization in oral cancer cell towards X-ray irradiation. The radio-sensitization effect of ICp_6 -Cu accompanied with a significant increase in ROS generation which is in agreement with the fact that ROS generated via radiolysis of water play a major role in X-ray induced cytotoxicity and the presence of X-ray absorbing metal can further enhance this process [37]. Here it is important to note that irradiation of high Z element is expected to yield better radio-sensitization efficacy because it can generate more number of secondary electrons than irradiating with lower-Z element [37]. In the present study, the X-ray energy used for photoactivation of ICp_6 -Cu was close to copper K-edge absorption. Since ICp_6 -Cu also contain iodine, irradiation with X-ray energy tuned to iodine K edge (~33 keV) may produce more efficient radio-sensitization against cancer cells. Of the two types of cell lines used, the radio-sensitization effect of ICp_6 -Cu was more pronounced in 4451 cells as compared to NT8e cells. As shown in fig 5.1 and fig 5.4, the intracellular level of ICp_6 -Cu and the relative level of ROS both are significantly higher in 4451 cells than that for NT8e cells. These results correlated with higher sensitivity of 4451 cells to ICp_6 -Cu induced radio-sensitization and further substantiate the role of photon-activation induced ROS generation in the radio-sensitization effect of ICp_6 -Cu. A relevant difference between the two cell lines is the status of p53 gene i.e. 4451 cells has mutated p53 gene [232], whereas, NT8e has wild-type p53 [231]. However, the difference in their sensitivity to radio-sensitization cannot be attributed to the difference in the status of p53, because the sensitivity of the two cell lines to X-ray alone was almost similar (fig 5.2). The

relationship between p53 status and radiosensitivity is not well understood and there are several conflicting reports on radiosensitivity vs p53 gene mutation [242-244].

An important mechanism of radio-sensitization effect of currently applied PAT drugs such as cisplatin and 5-iodo-2'-deoxyuridine is the enhancement in DNA damage and/or inhibition of DNA repair which is primarily attributed to the localization of these drugs in cell nucleus [245-247]. As shown in fig 5.5 c, IC_{p6}-Cu treatment did not lead to any increase in the level of X-ray induced DSBs which is because IC_{p6}-Cu is not localized in the cell nucleus (Chapter 4, fig 4.1). Interestingly, analysis of γ -H2AX foci at 2 and 24 h post-irradiation (fig 5.6 a and b) revealed that the repair of DSBs is significantly inhibited in IC_{p6}-Cu treated cells as compared to cells irradiated with X-ray alone. Previous studies have shown that platinated drugs inhibit or delay X-ray induced DSBs due to the formation of cisplatin–DNA adducts [245]. For, IC_{p6}-Cu the reason for inhibition of DNA repair and accumulation of unrepaired DNA is not clear. Confocal microscopic observation showed that X-ray irradiation of IC_{p6}-Cu treated cells led to the disintegration of lysosomes (fig 5.7 a). It is well documented that lysosomal membrane permeabilization and the leakage of cathepsins into the cytosol can trigger either necrotic or apoptotic cell death pathways [248]. Moreover, lysosomes contain *Dnase2a*, an endonuclease that degrades DNA to oligonucleotides and nucleotides and thus plays an important role in the clearance of damaged DNA. Recent studies have shown that DSBs induced by DNA-damaging agents accumulates to high levels in *Dnase2a* deficient cells [249]. Moreover, the persistence of unrepaired DSBs after radiation exposure has been identified as a potentially lethal event that triggers apoptotic cell death [250]. The results of cell

cycle analysis revealed that ICp_6 -Cu plus X-ray treatment induced significantly higher cell death than X-ray alone (fig 5.8).

5.4. Conclusion

In conclusion, ICp_6 -Cu showed a potent radio-sensitization effect in oral cancer cells. The underlying mechanism of radio-sensitization appears to be the photoactivation induced enhancement in ROS production which causes damage to lysosomes and subsequently leading to impairment of cell's ability to repair X-ray induced DSBs. In the present study, the X-ray energy used for photoactivation of ICp_6 -Cu was close to copper K-edge absorption which has low penetration depth (few millimeters) in soft tissue. Therefore, it needs further investigations using X-ray energy tuned to iodine K-edge (~33 keV) to establish the efficacy of ICp_6 -Cu for treatment of deep-seated tumors.

Chapter 6

Chemotoxic potential of ICp₆-Cu in cancer cells

6.1. Introduction

In addition to their potential use in PDT of cancer, some metal complexes of tetrapyrrole compounds can also exhibit cytotoxic activity against cancer cells in dark, due to the toxic effect of a bound metal ion. This has opened a new possibility to exploit the tumor localizing property of porphyrin and chlorin derivatives to localize preferentially in the tumor for combined anticancer therapeutics. For example, platinum (Pt), gold (Au), and ruthenium (Ru) complex of tetrapyrrole compounds have been shown to exhibit anticancer effect via both chemo as well as phototoxicity [119, 122, 123, 127, 131, 135, 177, 251-254]. On the other hand, some copper complexes of porphyrin and chlorin derivatives, have neither shown photodynamic activity nor any dark cytotoxic effect but on the contrary, act as antioxidants [255, 256].

In recent years, as an alternative to the nonessential metal-based drug, copper complexes have received significant attention as promising anticancer agents because of their property to induce cytotoxicity through modes that are different from the platinum-based anticancer drugs [150]. While platinum-based drugs inhibits DNA replication and transcription by forming platinum-DNA adduct, the mode of action of copper complexes involves redox-mediated elevation of ROS and/or inhibition of ubiquitin proteasome activity [150, 152]. Particularly, the property of the copper complex to increase intracellular ROS levels through redox process is considered useful because it can exploit the metabolic difference of normal and cancer cells to achieve tumor selective chemotoxicity [153, 154].

In this chapter, we have evaluated the chemotoxic efficacy of ICp_6-Cu in human oral cancer cells and non-cancerous keratinocytes cells. The effect of ICp_6-Cu

on cell viability, cell proliferation, cell morphology and intracellular ROS levels was monitored to assess its cytotoxic potential. The effect of antioxidants on induced cytotoxicity was also studied to verify the role of oxidative stress in the cytotoxic action of ICp_6-Cu . These studies revealed that ICp_6-Cu exert potent antiproliferative action against cancer cells through elevation of oxidative stress.

6.2. Results

6.2.1. ICp_6-Cu induced cytotoxicity

Oral cancer cells (NT8e and 4451) and non-cancerous keratinocyte (HaCaT) were treated with varying concentrations of ICp_6-Cu (10-100 μM) for 48 h, in dark and the effect of treatment on cell viability was determined by MTT assay. In fig. 6.1 a, the changes in percent cell viability of NT8e, 4451 and HaCaT cells as a function of ICp_6-Cu concentration is shown. In cancer cell lines, ICp_6-Cu led to a loss of cell viability in concentration-dependent manner, whereas there was no significant change in the viability of HaCaT cells. The IC_{50} value of ICp_6-Cu obtained from the sigmoid curve of cell viability vs ICp_6-Cu concentration for NT8e and 4451 cells was $\sim 34 \mu M$ and $\sim 40 \mu M$, respectively. While under similar conditions the metal free Cp_6 did not induce significant cytotoxicity both in oral cancer and HaCaT cells (fig. 6.1 b).

To further confirm the anticancer activity of ICp_6-Cu , its effect on cell proliferation of 4451 and NT8e cells was determined by multipoint kinetic MTT assay, as described in section 2.6.3. The percent cell proliferation (T/C %) of NT8e (fig.6.2 a) and 4451 cells (fig. 6.2 b) at different time intervals after treatment with 10, 20 and 50 μM ICp_6-Cu is shown in fig. 6.2. At a lower concentration (10 μM), ICp_6-Cu did not exert any significant effect on cell proliferation. At 20 μM which is below IC_{50} value, $\sim 20\%$

decrease in cell proliferation was observed after prolonged treatment (48 h). When the concentration was increased to 50 μM , (concentration above IC_{50}), a pronounced inhibition of cell proliferation occurred at 24 h after treatment, as indicated by the decrease in the value of T/C % to $\sim 6\%$. At the later time point (48 h) the value of T/C % did not change further indicating complete inhibition of cell proliferation.

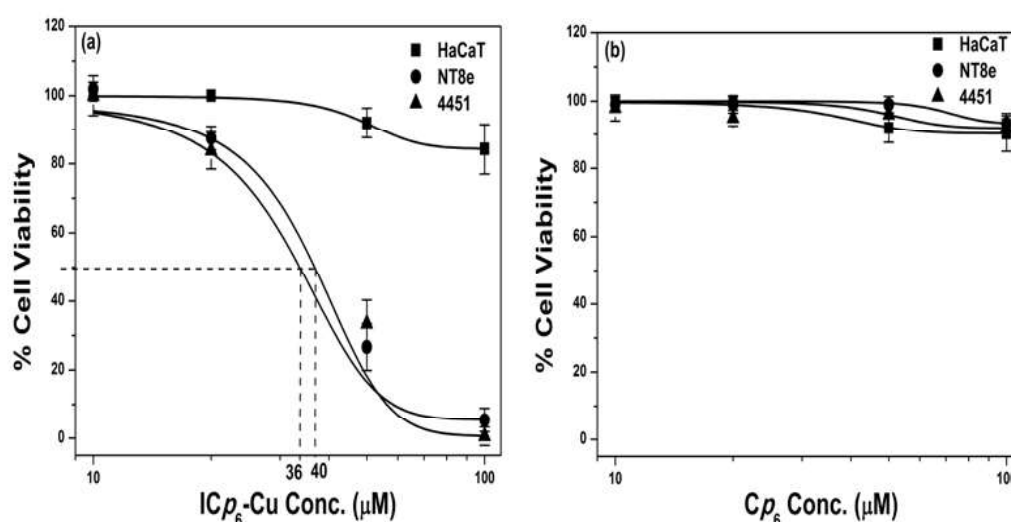


Figure 6.1. Effect of $\text{ICp}_6\text{-Cu}$ (a) and Cp_6 (b) treatment (48 h) on the viability of NT8e, 4451 and HaCaT cells. Percent cell viability was calculated with respect to control (without $\text{ICp}_6\text{-Cu}$ treatment). The horizontal dashed line represents 50% growth inhibition. Each data point represents mean \pm SD of three independent experiments.

6.2.2. Effect of $\text{ICp}_6\text{-Cu}$ on cell morphology

The effect of $\text{ICp}_6\text{-Cu}$ on cell morphology was studied by confocal microscopy after staining the cells with fluorescent dyes PI and HO which can identify and differentiate morphological changes associated with necrotic and apoptotic cell death. The representative confocal images of HaCaT, NT8e and 4451 cells in control and $\text{ICp}_6\text{-Cu}$ treated (50 μM , 48 h, in dark) cell monolayer are shown in fig 6.3. In control, all three cell types (HaCaT, NT8e and 4451) appear healthy indicated by intact cell

morphology, the absence of PI fluorescence and intact nuclear DNA (fig. 6.3 a, b, e, f, i, j). After ICp₆-Cu treatment, while HaCaT cells showed no change in the morphology, both NT8e and 4451 cells displayed marked alterations indicated by the formation of large vacuoles in the cytoplasm (fig 6.3 g) and loss of cell adherence with ‘rounded shape’ morphology (fig. 6.3 k), respectively. Further, the absence of PI uptake and/or DNA condensation or fragmentation in corresponding fluorescence images of NT8e and 4451 (fig 6.3 h & l), showed that cell death did not occur due to necrosis and apoptosis.

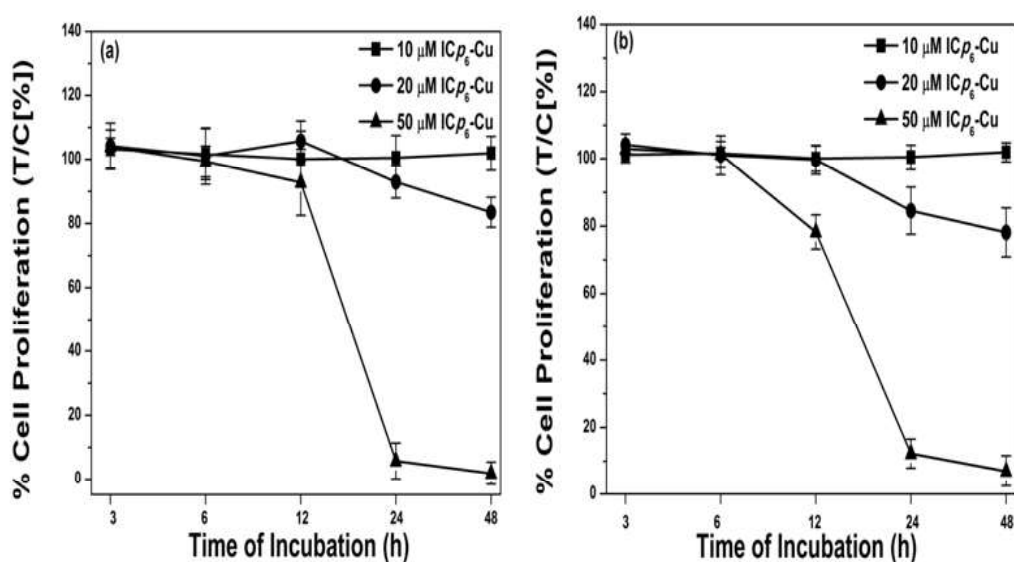


Figure 6.2. Time-dependent effect of ICp₆-Cu treatment (10, 20 and 50 μM) on the proliferation of NT8e (a) and 4451 (b) cells. The T/C values represent percent cell proliferation with respect to a control sample (without ICp₆-Cu treatment). Each data represents mean ± SD of three independent experiments.

6.2.3. ICp₆-Cu induced organelle damage

To further verify that ICp₆-Cu exerted the cytotoxic effect, damage to F-actin filaments of the cytoskeleton and Lysosomal membrane permeabilization (LMP) which are the major hallmark of non-apoptotic modes of cell death were also probed. The photomicrographs of control and ICp₆-Cu treated NT8e and 4451 cells after

staining with F-actin specific Phalloidin Alexa Fluor 488 are presented in fig 6.4. In control cells, F- actin filaments of the cytoskeleton are brightly stained and intact (fig 6.4 a & c). In contrast, the cells after ICp_6-Cu treatment lacked intact actin filaments and fluorescence of Phalloidin appeared as dotted structures indicating disruption of F- actin filaments (fig 6.4 b & d).

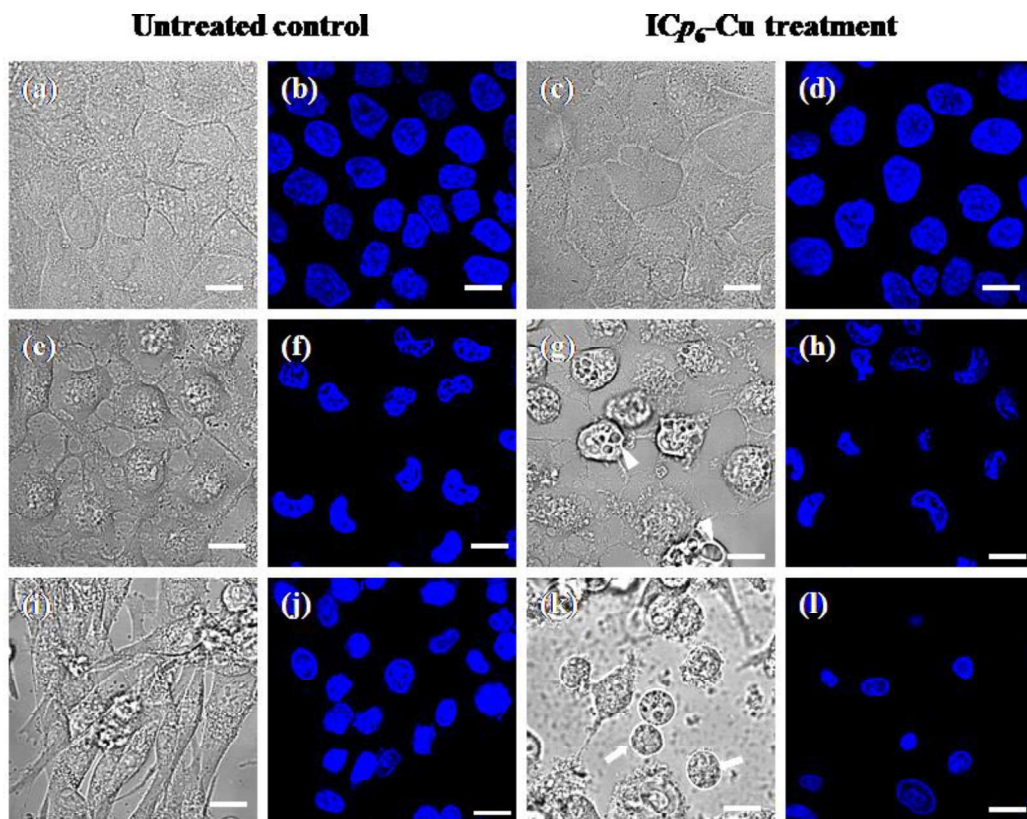


Figure 6.3. Photomicrographs of control and ICp_6-Cu treated ($50 \mu M$, 48h) HaCaT (a - d), NT8e (e- h) and 4451 (i - l) cells. The cells were stained with PI and HO and bright-field and corresponding fluorescence images are shown. Formation of vacuoles in NT8e cells and loss of cell adherence with 'rounded shape' morphology of 4451 cells are indicated by arrowheads, and arrows, respectively. Experiments were repeated three times with similar results and representative images are shown. Magnification 40X, scale bar $20 \mu m$.

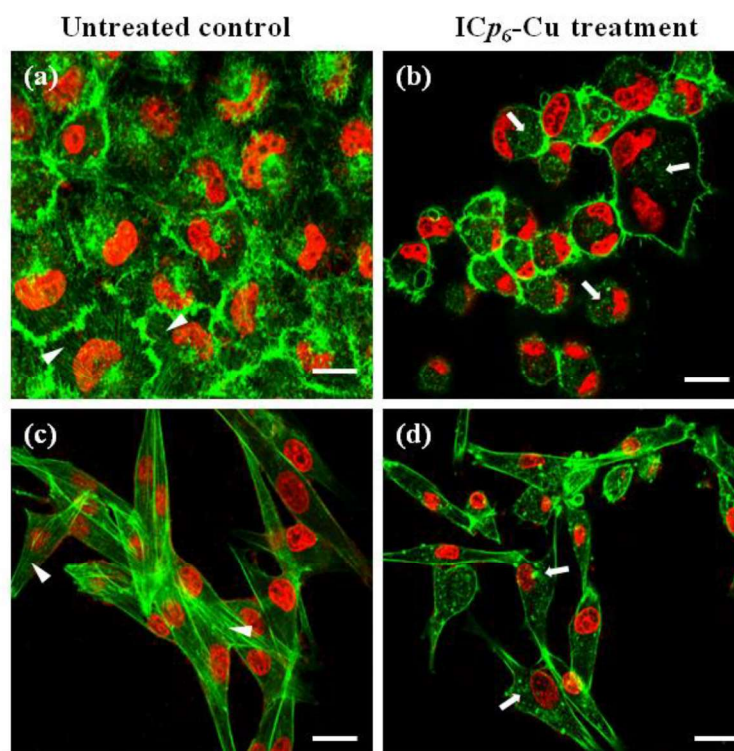


Figure 6.4. Confocal fluorescence photomicrographs of control and ICp₆-Cu (50 μ M, 48 h) treated NT8e (a, b) and 4451 (c, d) cells showing F- actin filaments of the cytoskeleton. The cells were stained with DAPI and Alexa Fluor 488 Phalloidin. Experiments were repeated three times and representative images are shown. Arrow indicates intact F- actin filaments; arrowheads indicate F- actin aggregates. Magnification 40X, scale bar 20 μ m.

Fig. 6.5 shows the photomicrographs of control and ICp₆-Cu treated NT8e and 4451 cells stained with AO, a fluorescence probe which accumulates in acidic vacuoles and emits red/orange fluorescence [257]. In the control cells, intact lysosomes in the cytoplasm are clearly visible as discrete vesicles having bright red punctuate fluorescence (fig 6.5 and c). In cells treated with ICp₆-Cu (Fig 6.5 b & d), the red fluorescence of AO is diminished and the vesicles with punctuate red fluorescence staining are less or absent. These observations indicate that ICp₆-Cu treatment led to partial or complete permeabilization of lysosomal membrane in both NT8e and 4451 cells.

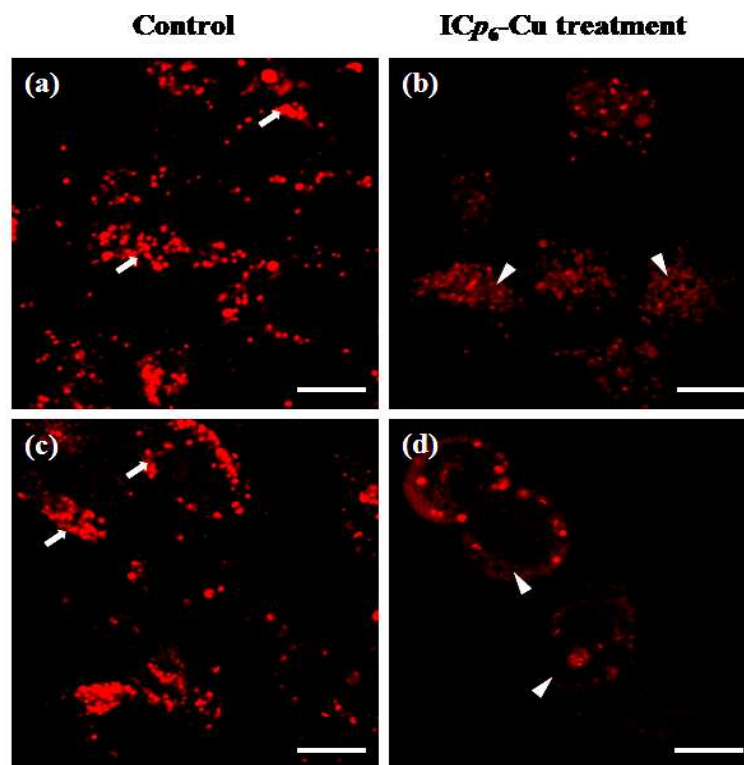


Figure 6.5. Confocal fluorescence photomicrographs of control and ICp₆-Cu treated (50 μ M, 48 h) NT8e (a, b) and 4451 (c, d) cells showing AO stained lysosomal acidic vesicles. Experiments were repeated three times and representative images are shown. Arrows indicate intact acidic lysosome, arrowheads indicate weak diffused lysosome staining. Magnification 40X, scale bar 20 μ m.

6.2.4. Effect of ICp₆-Cu on intracellular ROS levels

Fig. 6.6, shows levels of intracellular ROS in HaCaT and NT8e cells at different time periods after the treatment with 10 μ M and 50 μ M ICp₆-Cu. ICp₆-Cu at lower concentration (10 μ M) did not show any significant effect on the level of intracellular ROS which is consistent with an absence of cytotoxicity at this concentration. At higher concentration (50 μ M) ICp₆-Cu treatment led to time-dependent increase in the level of ROS in cancer cells (fig. 6.6 b) and a maximum increase of \sim 4 fold was observed at 24 h after the treatment. In contrast, the level of intracellular ROS did not change significantly in HaCaT cells (fig 6.6 a).

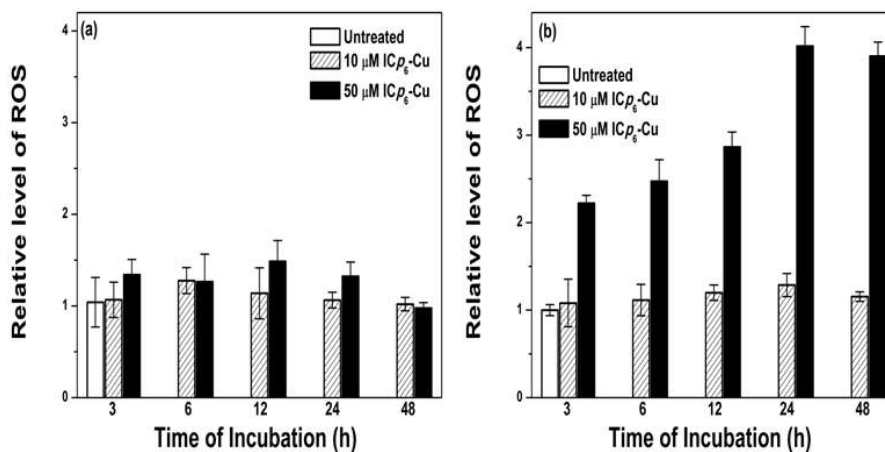


Figure 6.6. Changes in the levels of intracellular ROS relative to control in HaCaT (a) and NT8e (b) cells at different time periods after treatment with 10 μ M and 50 μ M of IC_{p6}-Cu. Data represent mean \pm SD obtained from three independent experiments.

To confirm the involvement of ROS in cytotoxic action of IC_{p6}-Cu, the effect of antioxidants (glutathione and trolox) on IC_{p6}-Cu induced cytotoxicity was studied in both cancer cell lines. Fig. 6.7 a and b, shows percent cell viability of NT8e and 4451 cells that were subjected to IC_{p6}-Cu treatment (50 μ M) for 24 and 48 h, without and with GSH (1 mM) and trolox (10 μ M) pre-treatment (2 h). At 24 h, in IC_{p6}-Cu treated cells that received antioxidant pre-treatment, the percent cell viability was significantly higher as compared to cells which received no pre-treatment. At prolonged treatment time (48 h), antioxidant pre-treatment did not lead to any significant increase in cell viability. Similarly, the inhibition of cell proliferation induced by IC_{p6}-Cu at 24 h was also reduced significantly by pre-treatment of cells with antioxidants (GSH and trolox) and the effect at the prolonged time was less pronounced (fig 6.7. c and d).

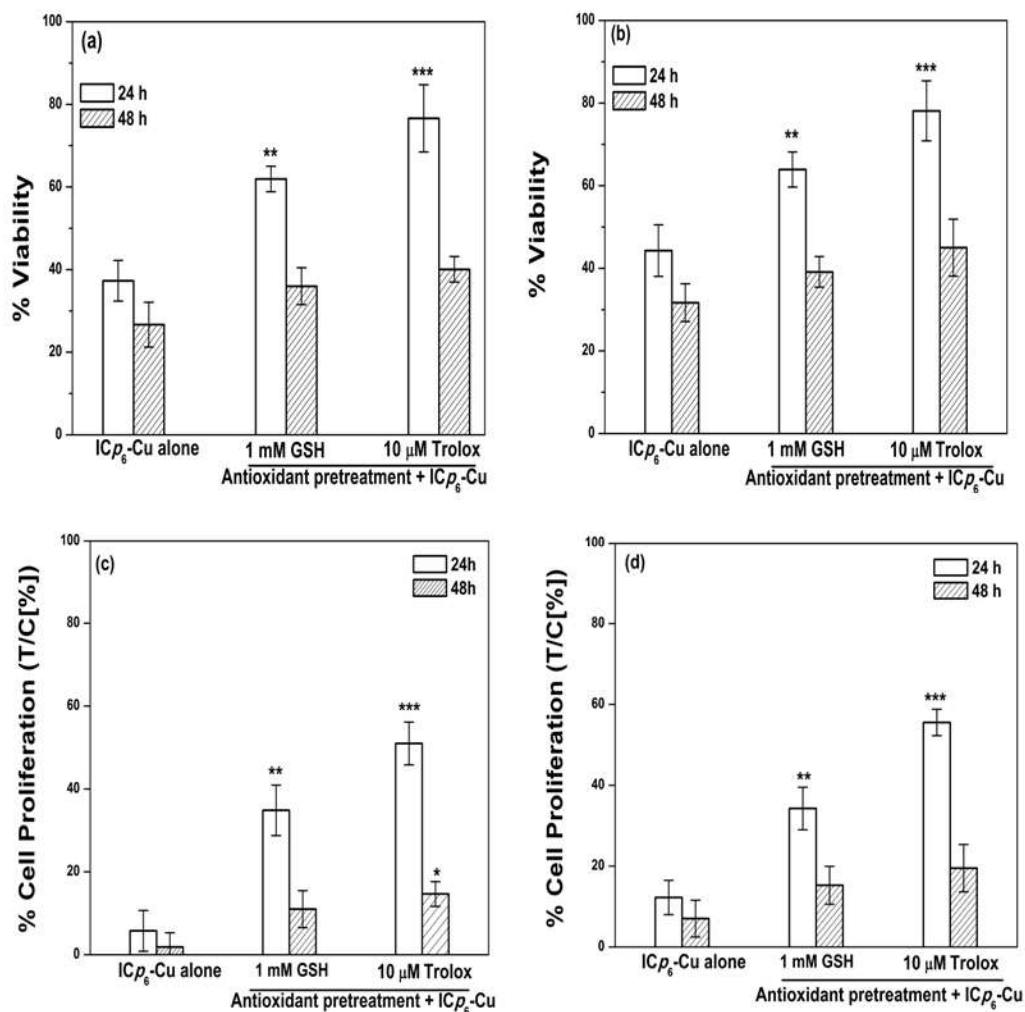


Figure 6.7. Percent cell viability and cell proliferation of ICp₆-Cu treated (50 μM) NT8e (a, c) and 4451 (b, d) cells without and with GSH and Trolox pretreatment (2 h). Data represents mean ± S.D obtained from three independent experiments. * = ($P < 0.05$), ** = ($P < 0.01$), *** = ($P < 0.005$), indicate significant difference from untreated control (without GSH and Trolox treatment).

6.3. Discussion

Copper coordination compounds are promising alternative to platinum-based anticancer drug as these have the ability to enhance the intracellular ROS levels via redox process and can provide selective cytotoxicity against cancer cells [258]. Motivated by this interesting rationale, the efficacy of ICp₆-Cu to induce cytotoxicity

in human oral cancer cell lines and non-cancerous keratinocyte cells was evaluated. Results show that ICp_6-Cu exerted pronounced cytotoxic action against oral cancer cells but did not show any effect on the non-cancerous human keratinocytes. The IC_{50} value of ICp_6-Cu ($\sim 40 \mu M$) was within the range as reported for platinum complexes [259] and some copper-based anticancer compounds such as copper (II) complexes of Schiff base, phthalate and dipyriddy [150]. Anticancer agents can be either cytostatic (suppress the growth of cancer cells) or cytotoxic (induce cell killing) [260], in order to verify this, the cytotoxic effect of ICp_6-Cu was further assessed by multiple point chemosensitivity assay [175]. Results showed that ICp_6-Cu exhibited pronounced cytostatic effect in both NT8e and 4451 cells. It is well known that when the cytostasis is profound and prolonged it can lead to cell death [260]. Interestingly, PI/HO staining revealed that ICp_6-Cu did not induce apoptosis or necrosis in both 4451 and NT8e cells (fig 6.3). Instead, changes in cellular morphology of ICp_6-Cu treated cells, such as the presence of large cytoplasmic vacuoles in NT8e cells (fig 6.3 g) and rounded shape morphology in 4451 cells (fig 6.3 k) indicated the possibility of some other mode of cell death. This is further supported by observation on damage to F-actin filaments of cytoskeleton (fig 6.4) and lysosomal membrane permeabilization (fig 6.5) in ICp_6-Cu treated cells. Similar morphological alteration in cancer cells after treatment with anticancer agents have been reported in several studies and these were considered to be hallmarks of non-apoptotic mechanisms of cell death such as autophagy, anoikis, lysosomal membrane permeabilization [261]. Although, further investigation is required to know the exact cell death pathway, here it is important to mention that anticancer agent that can induce non-apoptotic cell death pathway holds considerable promise to overcome the limitation of chemotherapy to treat apoptosis-

resistant tumor [261]. Consistent with this, ICp_6 -Cu showed almost same effectiveness against 4451 and NT8e cells, despite the fact that 4451 cell line has defective apoptotic machinery due to mutated p53 gene [232], whereas, NT8e with wild-type p53 is apoptotic proficient [231].

Results on the elevation of intracellular ROS levels by ICp_6 -Cu (fig 6.6) and the inhibitory action of antioxidants on ICp_6 -Cu induced cytotoxicity (fig 6.7) provided evidence that cytostatic effect of ICp_6 -Cu is mediated via an increase in oxidative stress. This is also consistent with changes observed in cellular morphology of treated cells and results observed in some previous studies. It has been shown that enhanced oxidative stress induces cytoplasmic vacuolization [262, 263], disruption of actin cytoskeleton [264], lysosomal membrane permeabilization [257, 265]. Interestingly, as compared to cancer cells the non-cancerous HaCaT cells did not show an increase in ROS levels after ICp_6 -Cu treatment which explains the absence of its cytostatic effect in these cells. HaCaT cells have been used in several studies as normal cells to test the efficacy and selectivity of anticancer drugs [266, 267]. It is well known that the cellular redox homeostasis in normal cells is well regulated through antioxidant defense mechanism. In contrast, cancer cells exhibit higher oxidative stress due to dysregulated redox homeostasis, hence they are more susceptible to further increase in intracellular ROS levels than the normal cells [268, 269]. The difference in sensitivity of HaCaT and cancer cells to oxidative stress is also in agreement with the previous reports [266].

6.4. Conclusions

Results demonstrate that ICp_6 -Cu induced pronounced chemotoxicity in oral carcinoma through elevation of intracellular ROS levels. It exhibited potent cytostatic effect and prolonged cytostasis appeared to trigger non-apoptotic cell death which is characterized by alterations in cellular morphology, cytoskeletal F-actin architecture and lysosomal membrane permeabilization. Results suggest that ICp_6 -Cu could be a potential anticancer agent which may provide selective chemotoxic effect based on the difference in susceptibility of normal and cancer cells to ROS.

Chapter 7

Summary and Future Prospective

Summary

Chlorin p_6 , a chlorophyll derivative which demonstrated promising results for PDT of tumors in previous studies was conjugated to copper iodide to widen the scope of its application for multimodal cancer treatment. In this research work, studies on characterization of the conjugate, its efficacy for photodynamic treatment, photon-activation treatment and chemo cytotoxicity led to several important findings as summarized below.

Results of studies on characterization of the metal complex by absorption, XRF, FTIR, EPR and Mass spectroscopy validated the expected optical properties and chemical structure of the conjugate. Fluorescence spectroscopic studies revealed that the photodynamic action of ICp_6 -Cu is mediated predominantly via free radical generation. Thus, ICp_6 -Cu is a novel PS which unlike already known copper complexes of porphyrins and chlorins contains copper attached to carboxylic groups instead at pyrrole -NH, an iodine atom at meso position and is able to efficiently generate ROS photodynamically.

Spectroscopic studies on the interaction of ICp_6 -Cu with HSA and DNA suggested that albumin acts as a carrier protein for ICp_6 -Cu and its binding did not affect the conformation of the albumin. Further, since the binding affinity of ICp_6 -Cu with DNA was same as that for Cp_6 and it is not likely to target cellular DNA.

In vitro studies on cellular uptake, intracellular localization and phototoxicity of ICp_6 -Cu in two oral cancer cell lines revealed that ICp_6 -Cu accumulates more efficiently than Cp_6 in cells and gets localized particularly in lysosomes and endoplasmic reticulum. Further, its efficacy to induce phototoxicity in cancer cells is not affected under hypoxia, a condition which generally prevails in the tumor. Studies

using various mechanistic probes of ROS confirmed that ICp_6-Cu acts through both type I and type II photochemical mechanism. From these results, it can be suggested that ICp_6-Cu is a promising agent for PDT of hypoxic solid tumors.

Since treatment of deep-seated tumor is a major limitation of PDT due to low penetration of light in tissue, another motivation to insert high Z element in Cp_6 was to explore its use for X-ray photon-activation which should overcome this limitation. Studies on the radio-sensitization efficacy of ICp_6-Cu in two oral cancer cell lines using synchrotron X-ray demonstrated that ICp_6-Cu led to significant enhancement in cytotoxic effect of X-ray via augmentation of ROS levels. Confocal microscopy and flow cytometry studies showed that combined treatment has no significant effect on cell cycle progression and damage to lysosomes and persistence of radiation-induced DNA double-strand breaks contributed to the radiosensitization effect of ICp_6-Cu . These results suggested that ICp_6-Cu is a potential agent for photon-activation therapy of cancer.

Studies on the potential of ICp_6-Cu to induce redox-mediated chemotoxicity in two oral cancer cell lines and non-cancerous keratinocyte cells showed that ICp_6-Cu also possess significant anti-proliferative activity against cancer cells but did not affect non-cancerous cells. Results on increase of intracellular ROS generation and inhibition of cytotoxicity by antioxidants showed that the chemotoxic effect of ICp_6-Cu is mediated via elevation of oxidative stress. Results also revealed that prolonged inhibition of cell proliferation by ICp_6-Cu led to induction of non-apoptotic mode of cell death. These studies suggested that ICp_6-Cu also acts as a cytotoxic agent and may provide tumor selective chemotoxicity because of the difference of redox environment in normal and cancer cells.

Conclusions and future perspective

In conclusion, the strategy to conjugate Cp_6 to copper iodide successfully yielded a novel PDT PS which could provide PDT efficacy against cancer cells both under normoxic and hypoxic conditions, induce significant radio-sensitization of cancer cells through X-ray photoactivation and also possess ability to induce cytotoxicity as chemotherapeutic agent. Thus, there would be considerable advantage for use of ICp_6 -Cu in combined cancer treatments. However, there are some possibilities which may be worth investigating to fully establish the efficacy of ICp_6 -Cu for PDT and PAT.

Since ICp_6 -Cu is capable of inducing cytotoxicity in dark, it may help to improve the efficacy of PDT by eliminating the non-respondent cancer cells and thereby can prevent tumor recurrence. Thus, further studies in animal model will be useful in order to establish the advantage of combined PDT and chemotoxic potential of ICp_6 -Cu.

The blue-shifted optical absorption of the longest Q band of ICp_6 -Cu is not a favorable feature for PDT as it would decrease the depth of treatment. One possible way to deal this is the application of two-photon excitation which can allow its activation with a tissue penetrating longer wavelength light.

Irradiation of high Z element is expected to yield better radio-sensitization efficacy because it can generate more number of secondary electrons than irradiating with a lower-Z element. At present, the X-ray energy used for photoactivation of ICp_6 -Cu was close to copper K-edge absorption. Since ICp_6 -Cu also contain iodine, to establish its potential for treatment of deep-seated tumor it would be worthwhile to explore its radio-sensitization efficacy at higher energies.

In addition, the presence of iodine atom and paramagnetic copper in ICp_6-Cu can also be exploited for X-ray contrast imaging and/or magnetic resonance imaging of tumor (Appendix. A. Fig. A.2.).